CFD Analysis of Piston Cooling Jets

Master of Science Thesis

Halil I. Çelik

Technische Universiteit Delft

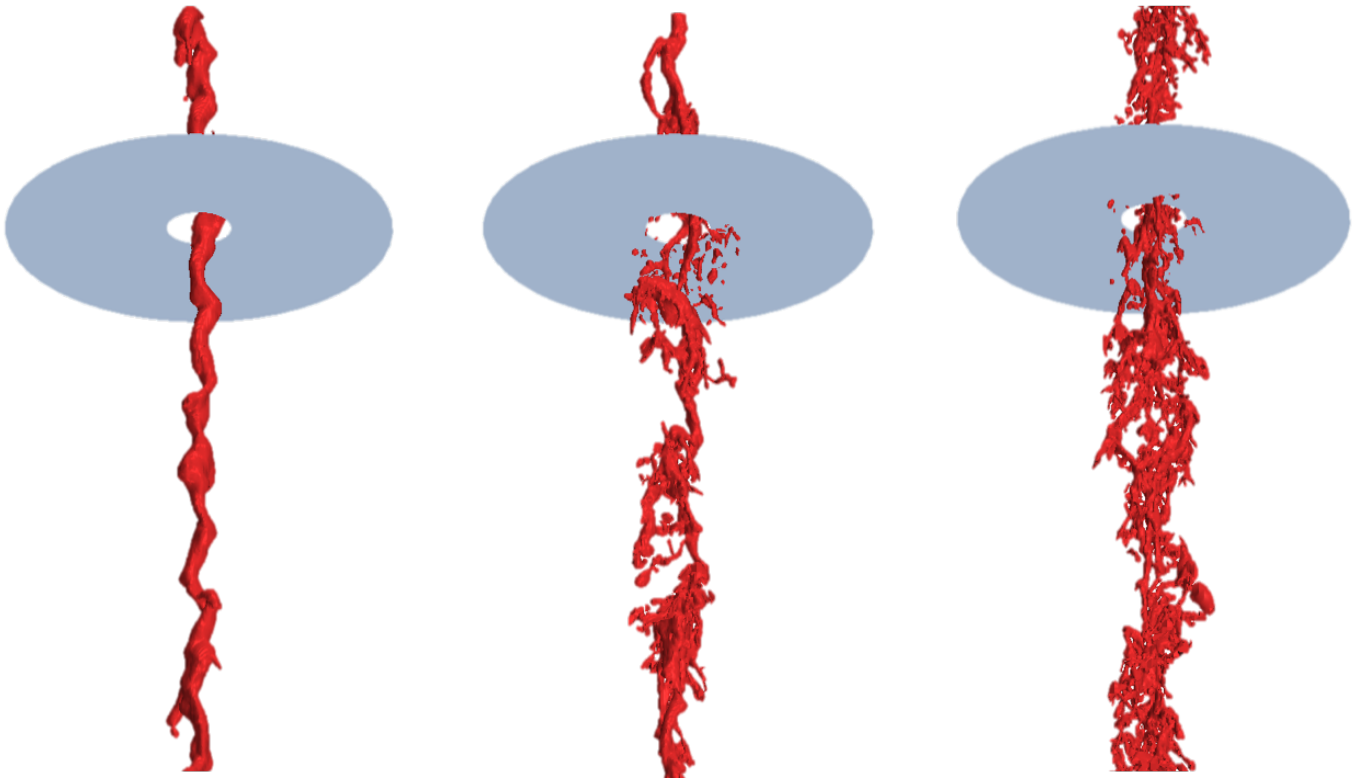

TU Delft Delft University of Technology

DAF A PACCAR COMPANY

Challenge the future

CFD Analysis of Piston Cooling Jets

by

Halil I. Çelik

in partial fulfillment of the requirements for the degree of

Master of Science

in Aerospace Engineering

at the Delft University of Technology,

to be defended publicly on Thursday March 15, 2017 at 2:00 PM.

Supervisors:	Dr. J. Znaien	DAF Trucks N.V.
	Dr. ir. A. H. van Zuijlen	TU Delft
Thesis committee:	Dr. ir. M. Gerritsma	TU Delft
	Dr. C. Lettieri	TU Delft

This thesis is confidential and cannot be made public until March 1, 2023.

TU Delft Delft University of Technology

Acknowledgements

I would first like to thank my daily supervisor at DAF, Jemil Znaien, for taking the time to have two meetings every week for the entire duration of this project. He always allowed the research project to be my own work, but steered me in the right direction whenever he thought it was needed. Also, many thanks for the computational resources that he continuously made available during my Large Eddy Simulations. Finally, my sincere thanks for spending your Saturday evenings reading chapters of my thesis.

I would also like to thank Dr. Van Zuijlen, my university supervisor, for the progress meetings we had, where his 'outsider' view was often very enlightening. I appreciate his knowledge, patience and critical feedback, that helped me in writing and improving this thesis.

Finally, I must express my very profound gratitude to my family and girlfriend for providing me with unfailing support and continuous encouragement throughout my years of study and through the process of researching and writing this thesis. This accomplishment would not have been possible without them. Thank you.

Table of Contents

List of Figures

List of Tables

Nomenclature

Abbreviations

BDC	Bottom dead centre
CFD	Computational Fluid Dynamics
DNS	Direct Numerical Simulation
LES	Large Eddy Simulation
LPM	Litre per minute
MSF	Multiphase Segregated Flow
OFR	Oil fill ratio
PCJ	Piston cooling jet
RANS	Reynolds Averaged Navier-Stokes
RST	Reynolds Stress Tensor
TDC	Top dead centre
TKE	Turbulent kinetic energy
URANS	Unsteady Reynolds Averaged Navier-Stokes
VOF	Volume of Fluid

Subscripts

0	Stagnation point
∞	Ambient/far field conditions
avg	Area averaged
aw	Adiabatic wall conditions
$cond$	Conduction
$conv$	Convection
$cycle-avg$	Engine cycle averaged
i	Phase
l	Liquid
max	Maximum
min	Minimum
r	In radial direction
rad	Radiation

s	Surface
T	Thermal
w	Wall conditions

Greek symbols

α	Volume fraction
δ	Boundary layer thickness
ϵ	Turbulent dissipation rate
η	Flow rate efficiency
μ	Dynamic viscosity
ω	Specific dissipation rate
ρ	Density
σ	Stefan-Bolzmann constant (for radiation)
σ	Surface tension force (for multiphase flow)
σ	Turbulent length scale (for inlet conditions in CFD)
θ	Inclination angle

Latin symbols

C	Celsius
c_p	Specific Heat
D	Disc diameter
d	Jet diameter
h	Convective heat transfer coefficient
k	Thermal conductivity
L	Target distance
Nu	Nusselt number
Oh	Ohnesorge number
p	Pressure
Pr	Prandtl number
q''	Heat flux
r	Radius (on impingement plane)
Re	Reynolds number
S	Spreading
s	Region of maximum Nu (with oblique impingement)
T	Temperature
t	Time

u, v, w	Velocity components in x, y and z directions
We	Weber number
y	Dimensional wall distance
y^+	Non-dimensional wall distance

1 Introduction

As any other truck manufacturer in the market, DAF aims to fulfil their customers' wills and needs, by increasing their engine performance and decreasing fuel consumption. The increasing engine performance results in higher (thermal) loads on engine parts, and especially on parts that form the combustion chamber [19]. One of these parts is the piston, which is the only non-stationary part in the combustion chamber, and thus the standard cooling system of the engine can not be used to cool down the piston. Proper control of the piston temperature is important and one of the determining factors in a modern successful engine design [20].

The common solution in industry to avoid overheating of the piston is by cooling it with engine oil. This solution is applied at the DAF engines for over 30 years. Nevertheless, there is a limited knowledge at the company about the piston cooling process: it only extends so far that it is known that the cooling is necessary to avoid damage and/or failure, and that the currently applied cooling mechanism gets the job done. The highly dynamic environment around the reciprocating piston makes it very difficult and expensive to gain more insight into this process by performing experiments [17]. A more practical and less expensive way of gaining more insight into the piston cooling process is by using Computational Fluid Dynamics (CFD). The goal of the research project is therefore to investigate the piston cooling process by using CFD.

The research conducted and presented in this thesis can be considered as the first steps towards reaching this goal. The entire project can be divided into different sub-projects, of which the first part will be covered in this thesis. The remaining sub-projects are left to be conducted as follow-up studies, and these are discussed in detail in the recommendations section of this thesis. This introductory chapter provides the exploration of the problem area, the initial problem statement and the structure of this report.

1.1. Background

With increasing performance of combustion engines, cooling the piston is essential in order to maximise the efficiency and durability of the engine. The trend of increasing performance of combustion engines over the past 100 years is nicely illustrated in Fig. 1.1. At DAF, the aim is to maintain this trend in the coming years by improving their engines, and hereby maintaining their position in the market.

There are two main methods to control piston temperatures in the automotive industry, depending on the amount of heat that needs to be removed. The first method is called spray cooling, where engine oil is splashed onto the lower surface of the piston. The relatively cold oil hits the hot surface and cools it down. This method is commonly used for gasoline engines, though it can be used for diesel engines at low power outputs. When the heat removal with spray cooling is not sufficient, then mostly pistons with a cooling gallery are used. A cooling gallery is a ring-shaped cavity inside the piston. This gallery contains an inlet and outlet hole, through which the engine oil can enter and leave the gallery. By partially filling the gallery, the recipro-

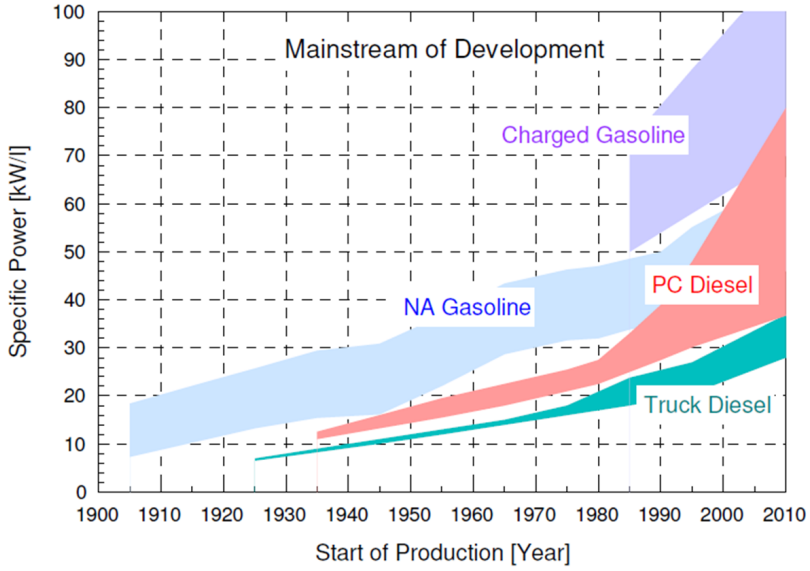

Figure 1.1: Performance development of combustion engines in the last 100 years[1].

cating motion of the piston creates a sloshing flow inside the gallery, and the turbulent oil flow cools down the piston[1]. Examples of the pistons used for both cooling techniques are shown in Fig. 1.2.

Figure 1.2: Examples of typical diesel engines: (left) for spray cooling [1] and (right) for gallery cooling [2].

It is clear that the combustion side for both pistons is very similar, since this side of the piston is optimised in order to achieve an efficient combustion process. The focus of this project is on the lower side of the piston, where the piston cooling takes place. It can be seen that this surface is completely different for both pistons. The piston used for spray cooling has a curved lower surface, such that the oil impinges on one side of the piston pin and leaves from the other side. The gallery cooling pistons contain the cooling gallery, and it can be seen that the cooled surface is much closer to the hot side of the piston, with shorter heat flow paths.

Other key motivations for applying and improving the piston cooling process are the following:

- **Thermal fatigue**
  The heat created by combustion warms up the upper surface of the piston, hereby creating a temperature gradient inside the piston. This temperature gradient results in different thermal expansions of the material inside the piston. This in turn produces different stresses, which in time can result in cracks and eventually failure. If the effect of these temperature gradients can reduced, then the thermal fatigue in the piston will similarly be reduced [21].

- **Creep**
  At high temperatures and high mechanical loads due to the compression and combustion process, the piston material will creep and eventually rupture. With creep deformation, the material strains over a longer period of time until it fails, though it can occur in relatively short time frames under very high temperature conditions [21]. Again, reducing the thermal loading by cooling reduces the onset of creep in the piston material.

- **Emissions**
  With more and more strict legislation regarding exhaust emissions, the emissions of NOx, CO, HC and PMs need be controlled and reduced. Controlling the piston temperature can significantly reduce these emissions [22]. Decreasing the piston temperature Piston temperature control is therefore included in many emissions reduction strategies.

- **Power consumption and fuel efficiency**
  The cooling can be improved by increasing the flow rate of the piston cooling jets, for which also the pump power needs to be increased. When an oversized oil pump is used, this reduced the engine performance, since the power for the pump is provided by the output power. Therefore, the cooling process needs to be optimised, such that there is sufficient cooling and maximum engine power output. Increasing the engine power output results in a higher fuel efficiency, which is defined as the distance travelled per liter of fuel consumed.

1.2. Initial problem statement

The DAF pistons are all (diesel) pistons with a cooling gallery. The CAD model of the piston can be seen in Fig. 1.3. It can be seen that the cooling gallery contains three holes. The two larger holes are the inlet and outlet of the cooling gallery. The third hole, which is slightly smaller than the other holes, is there to feed some of the oil to the oscillating piston pin, for lubrication purposes.

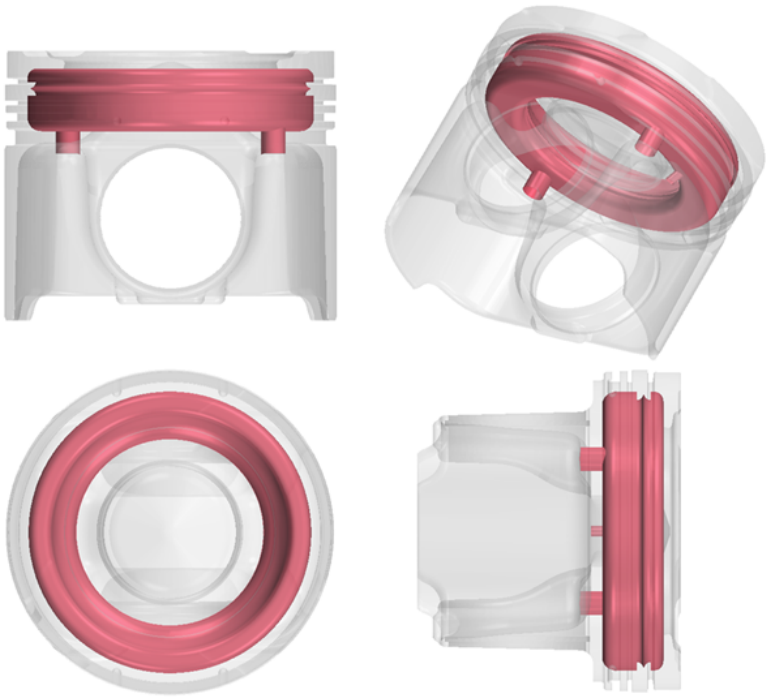

Figure 1.3: CAD model of DAF piston with a cooling gallery.

Gallery cooling is a technique applied to the DAF engines for more than 30 years. Nevertheless, the knowledge at the company about this process is very limited. Experimental testing of the cooling process is not done because of the complexity and costs related to such an experiment. At the moment, the knowledge at the

company extends so far that it is known that the cooling process works and that, without any additional piston cooling, failure will occur. A more efficient and less expensive way of analysing this problem is by means of a CFD analysis. The analysis needs to show how efficient the cooling method is, and how the cooling process can be improved.

Since this is the first CFD analysis on piston cooling at DAF, a fundamental approach is opted for, such that every sub-project of the problem is investigated extensively. The division of the project into different sub-projects is done as follows:

- The oil jet
- Impingement
- Spray cooling
- Gallery cooling
- Lubrication of the piston pin

In this thesis project only the first three sub-projects are considered; and the other two are to be investigated in follow-up projects.

The analysis of the oil jet is the first part of this project. The jet is investigated by isolating it from the piston cooling problem, such that the focus can be on accurately simulating the oil jet behaviour and sensitivity to different operating conditions, before investigating the impingement or heat transfer. The research objective of this sub-project is to determine the oil jet characteristics at relevant piston locations, by using both the RANS and the LES methods.

The second sub-project in this project is on simulating the impingement. Because of the increasing complexity and mesh requirements for near-wall flow, LES is not considered as a practical way to deal with turbulence at this stage, and all simulation work is done with RANS. The analysis of the impingement is done for a simplified spray cooling problem, such that the focus can be on modelling the convective heat transfer. The research objective of this sub-project is to develop a simple, fast and reliable CFD model, that is able to make accurate heat transfer predictions for an impinging oil jet, by using RANS.

The third and final sub-project in this thesis project is on investigating the spray cooling method. Even though this method is not used by DAF for the cooling of their pistons, it is believed that this is a logical step to make, before investigating the (relatively unknown and complex) gallery cooling method. The research objective is thus to analyse the spray cooling method, by combining the results of sub-projects 1 and 2.

1.3. Structure of the report

The report is structured as follows. The review of past work on relevant research areas is presented in Chapter 2. The RANS and LES results for the oil jet analysis are discussed in Chapter 3. The effect of different operating conditions on the behaviour of the jet behaviour is investigated in this chapter by performing a trend analysis. Chapter 4 deals with the development of the CFD model used for the analysis of the impingement. Again a trend analysis is performed, by varying the operating conditions, now checking the effect on the impingement heat transfer. Finally, in Chapter 5 the results of part 1 and part 2 are combined to analyse the spray cooling method. The thesis ends by listing the main conclusions and by presenting recommendations, for the work done in this thesis and for the remaining two sub-projects.

2

Literature review

This chapter presents an overview of the literature and past work conducted on research areas that are relevant for the CFD analysis of the piston cooling problem. The three main topics discussed in this chapter are: the physics of liquid jets, heat transfer after liquid jet impingement and relevant aspects of CFD.

2.1. Liquid jets

The first research area reviewed in this chapter is the physics of liquid jets and their behaviour in operating conditions similar to the conditions of the DAF piston cooling jets. First the typical classification of liquid jets will be discussed, followed by a section on the stability and disintegration.

2.1.1. Free-surface liquid jets

The study of liquid jets is a topic that has been studied for over one hundred years, for all different sorts of applications. Before reviewing the physics of liquid jets an important distinction needs to be made, based on the surrounding medium the jet travels through. When a liquid jet passes through an environment consisting of the same medium, this jet is called a submerged jet. These jets are characterised by a high level of interaction with the surrounding medium. The second type of liquid jets are jets passing through a different medium, such as a liquid in a gas. These jets are called free-surface liquid jets, and the level and type of interaction is totally different compared to submerged jets. A visual comparison between the two types is given in Fig. 2.1, with the main parameters involved: the jet diameter at the nozzle exit (d), the jet velocity at the nozzle exit (v), the jet temperature at the nozzle exit (T) and the wall temperature (T_w).

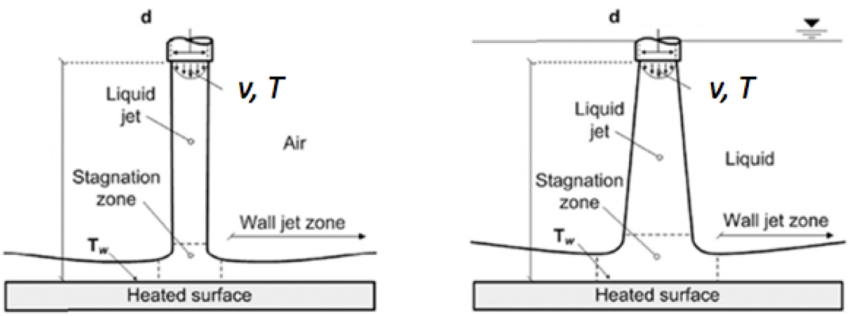

Figure 2.1: Difference between free-surface jets (left) and submerged jets (right), from [3].

The characteristics of submerged jets are very similar to gas jets, which means that the extensive literature available on gas jet behaviour can be used to study submerged liquid jets [23]. Unfortunately, these studies can not be used for free-surface liquid jets. The jets considered in this project piston cooling oil jets operating in a space filled with air. The focus of this thesis is therefore only on free-surface liquid jets, and only studies performed on these jets are reviewed and presented next.

2.1.2. Breakup

Free-surface liquid jets are often classified based on the mechanism of breakup, which is depending on different parameters of the jet, such as inertial forces, surface tension forces, viscous forces and aerodynamic forces. For steady injection of a liquid through a circular nozzle into still air, a typical classification is into four regions, based on two parameters: the Reynolds number (Re) and the Ohnesorge number (Oh) [4].

$$Re = \frac{\rho v d}{\mu}, \tag{2.1}$$

$$Oh = \frac{\mu}{\sqrt{\rho \sigma d}}, \tag{2.2}$$

with ρ the liquid density, μ the liquid dynamics viscosity and σ the surface tension between the liquid and surrounding gas. The Ohnesorge number can also be expressed as a function of the Weber number (We) and the Reynolds number:

$$We = \frac{\rho v^2 d}{\sigma}, \tag{2.3}$$

$$Oh = \frac{We^{0.5}}{Re}. \tag{2.4}$$

These dimensionless parameters, Re and Oh, represent respectively the inertial-to-viscous force ratio and viscous-to-surface tension force ratio. The classification is depicted in Fig. 2.2, with the blue indication representing the region where the current DAF oil jets are operating based on the two mentioned parameters. The DAF engine oil jet properties and operating conditions are shown in Table 2.1 and Table 2.2. It can be seen that the flow rate and target distance are the only varying parameters in these tables.

Table 2.1: Relevant DAF engine oil (10W-30) properties at 100 °C.

Density	810.1	$[kg\,m^{-3}]$
Dynamic viscosity	$9.542{\cdot}10^{-3}$	$[N\,m^{-1}s^{-1}]$
Specific heat per unit mass	2170	$[J\,kg^{-1}K^{-1}]$
Thermal conductivity	0.128	$[W\,m^{-1}K^{-1}]$
Surface tension	0.024	$[N\,m^{-1}]$

Table 2.2: Piston cooling jet operating conditions.

Nozzle diameter	3.0	$[mm]$
Target distance	78-230	$[mm]$
Flow rate	6-8	$[L\,min^{-1}]$
Temperature	100	[°C]
Reynolds number	3,600-4,800	[-]
Weber number	20,000-36,000	[-]
Ohnesorge number	0.0395	[-]

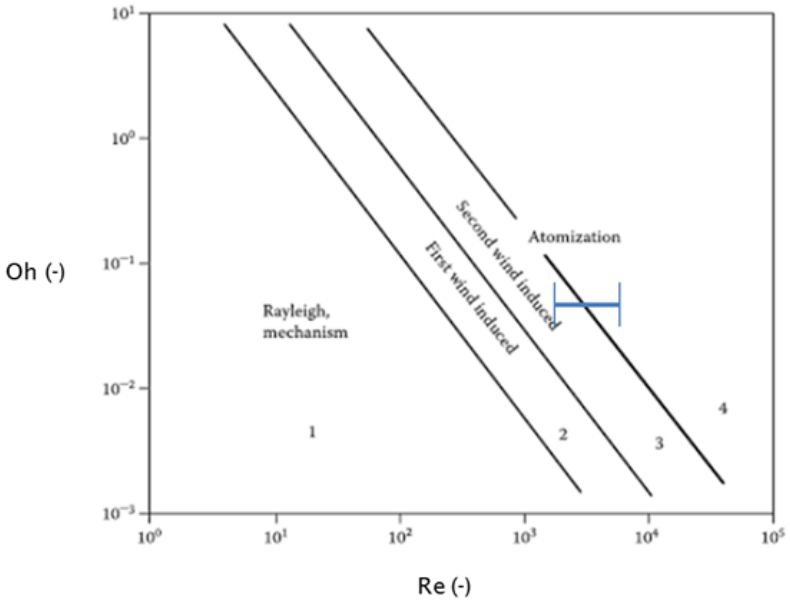

Figure 2.2: Classification of jets, based on the breakup mechanism [4], with the region of interest for the DAF jets indicated by the blue line.

The first breakup mechanism is called the Rayleigh breakup mode. The jets in this mode are low speed jets with low Reynolds numbers, where the breakup is in the form of drop formation. Initial disturbances and surface tension forces cause small perturbations, which grow as surface waves along the liquid-air interface and eventually induces the jet to break up. The breakup length of the jet is proportional to the jet velocity and the drop diameter is larger than the jet diameter [4][24]. An illustration of the Rayleigh breakup is given in Fig. 2.3.

The second region in Fig. 2.2 is called the first wind-induced breakup mode. When the velocity of the jet is increased, aerodynamic forces become more dominant and the surface tension influence decreases. The breakup is now caused by oscillations with respect to the jet axis (sinuous waves) [4][24]. The average drop size decreases and is similar in size to the jet diameter.

If the velocity is increased even more, the jet breaks up according to the third breakup mode. The second wind-induced breakup mode is similar to the first wind-induced mode [25]. The difference between the two regimes is that the relative velocity between the phases increases and the aerodynamics effect is larger. This results in shorter wavelength disturbances and smaller droplets for the second wind-induced breakup [4][25]. The drops separate in two zones as primary breakup and secondary breakup. Primary breakup is the drop formation from the coherent part of the jet, while secondary breakup is called the point where the jet is completely turned into small droplets [26]. This is also shown in Fig. 2.3.

The final breakup regime is the atomization regime, where the jet breaks up close to the nozzle in a chaotic manner. First, unstable ligaments are formed by growing instabilities. The ligaments shorten with increasing velocity and much smaller droplets are formed. The jet has the shape of a conical spray. The fourth breakup mechanism is not described as accurately as the other three, since the atomization process is still an relatively unknown process. Although various mechanisms and hypotheses are suggested in literature to explain this phenomenon, there is not one single mechanism responsible for the breakup, and a combination of factors is involved [5].

It can be concluded from Fig. 2.2 that the relevant breakup mechanisms in this project are the second wind-induced and the atomization breakup. It is known from [21] that the cooling (with the spray cooling technique) is maximised when the jet is still intact at impingement onto the piston surface. Several researchers have derived correlations for the breakup distance, and these correlations can be used to make a prediction for the breakup length. The correlations are listed in Table 2.3. It can be seen that two of the correlations are

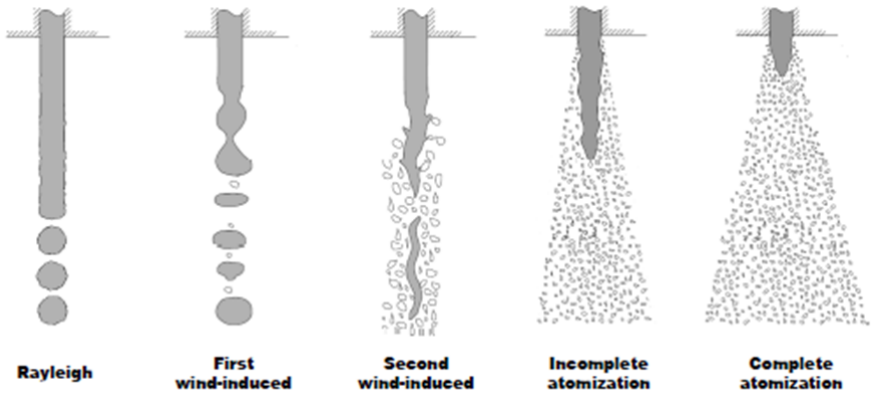

Figure 2.3: Classification of liquid jet breakup mechanism, with the incomplete atomization case most similar to the jets used by DAF [5].

functions of the Weber number, whereas the third correlation is only depending on the gas density ratio of the oil and the air. The predictions are done for the lower and upper Weber numbers presented in Table 2.2, and the density of air is set at its value at sea level: 1.225 kg/m^3.

The breakup lengths are predicted for the non-dimensional jet length (L/d). The maximum nozzle-to-target distance considered in this study is the distance between the nozzle exit and the piston at its maximum position, which is called the top dead centre (TDC). This corresponds to a distance of $L/d = 77$ for a 3 mm nozzle diameter. Based on the predictions in Table 2.3 it can thus be concluded that the jet is expected to remain intact for the distances and nozzle diameter considered in this project.

Table 2.3: Breakup length predictions for DAF oil operating conditions.

Researchers	Correlation	Prediction (L/d)	Valid for
Grant & Middleman [27]	$8.51We_l^{0.32}$	203 - 282	$300 < We_l < 90,000$
Phinney [28]	$55 + 1.085We_l^{0.5}$	209 - 312	$100 < We_l < 60,000$
Sallam, Dai and Faeth [29]	$11(\rho_l/\rho_g)^{0.5}$	283	$30,000 < We_l$

2.1.3. Spreading

Besides the breakup of the jet, also the spreading is an important physical characteristic of the jet in a piston cooling configuration. Especially for the gallery cooling technique, a large spreading will result in an oil jet that cannot sufficiently fill the cooling gallery, and as a result of this the heat transfer will be affected. It is observed that the spreading behaviour is a relatively unknown research area, as there are not many studies available in literature on this topic.

Moghe and Janowiak (2017)

Moghe and Janowiak [6] are one of the few researchers that studied the spreading behaviour of oil jets (for a gallery cooling problem). They performed a LES study, in which they determined the spreading of the oil jet for different flow rates. Their results are presented in Fig. 2.4. A conclusion that can be drawn from these results is the spreading increases with increasing flow rate. This can be explained by the increasing turbulence levels in the flow, which results in a more intense interaction and a more chaotic jet behaviour. It can also be observed that the onset of spreading moves upstream with increasing flow rate, meaning that these interactions start earlier with increasing turbulence levels. The unsteady surface instabilities that initiate the disintegration of the jet are clearly visible in their LES results.

In order to relate these results to the DAF oil jets, one can compare the non-dimensional parameters discussed before (Re and Oh). It can be seen in Table 2.4 that case B of Moghe and Janowiak has exactly the

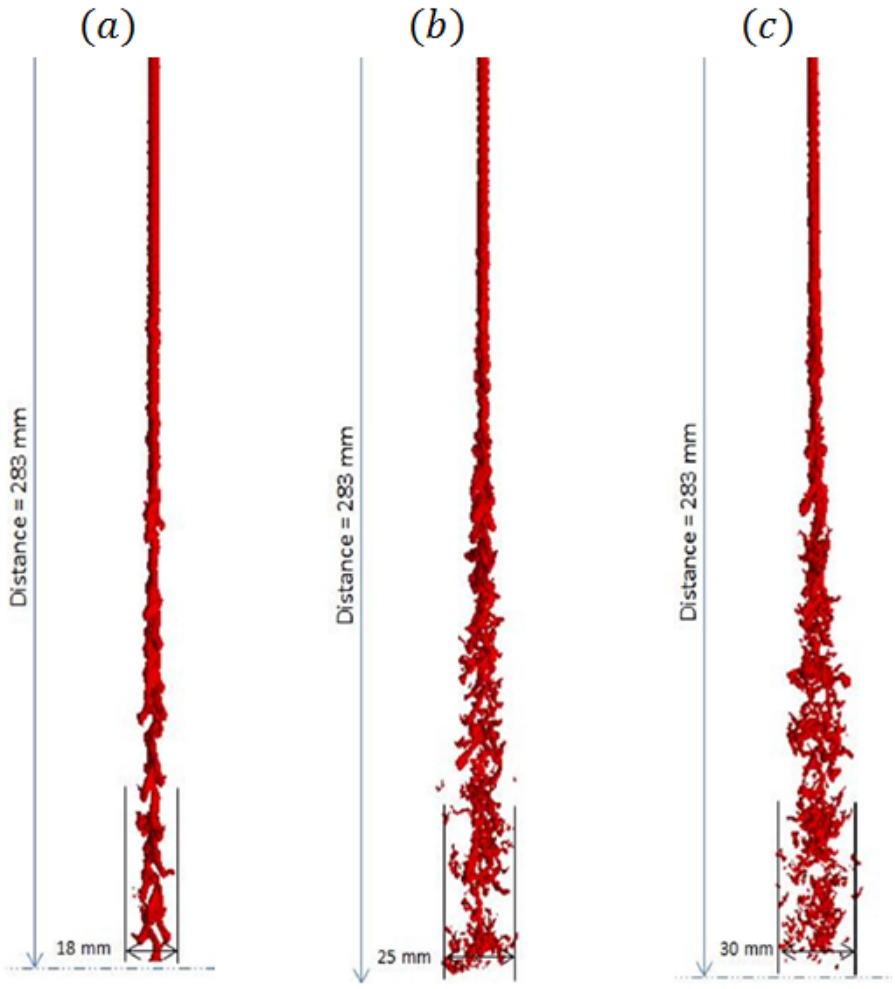

Figure 2.4: Results obtained by Moghe and Janowiak [6], for flow rates of (a) 6.3 L/min, (b) 11.1 L/min and (c) 14.4 L/min.

same Re and We values as the 8 L/min DAF jet, therefore the expectation is that the spreading of the DAF jets will be similar to the spreading of the Case B jet. The researchers determined that the spreading of the jet in Case B is equal to 25 mm, obtained for a 3.5 mm nozzle diameter and a target distance of 283 mm. Both the diameter and the target distance in the current project are smaller, therefore it can be said that the spreading is not expected to be larger than 25 mm for the 8 L/min DAF oil jet (at the TDC location of the piston). The exact determination of the spreading is part of the research, and is dealt with in Chapter 3.

Table 2.4: Comparison of non-dimensional parameters (Moghe and Janowiak vs. DAF)

	Case A	Case B	Case C	DAF 6 L/min	DAF 8 L/min
Re	2,700	4,800	62,00	3,600	4,800
We	11,000	36,000	60,000	20,000	36,000
Oh	0.039	0.039	0.039	0.0395	0.0395

DAF Experiment (2015)

Another case that can be used to gain more insight into the spreading behaviour of the jet is the flow rate efficiency experiment performed by DAF [30]. In this experiment, rather than directly determining the spreading, the aim was to determine the amount of oil that actually enters the cooling gallery at the TDC position of the piston. The cooling gallery is represented by a flat plate in this experiment. By comparing the flow rate exiting

the nozzle and the flow rate entering through the inlet orifice, the flow rate efficiency (η) can be determined:

$$\eta = \frac{FR_{orifice}}{FR_{nozzle}} \cdot 100. \tag{2.5}$$

The flow rate entering through the orifice was determined by running the experiment for a certain period of time, and by collecting the oil entering through the orifice in a sump. By using the run time and the weight of the collected oil in the sump, the flow rate through the inlet orifice can be determined. This is done for different flow rates between 3 L/min and 7 L/min. The setup of the experiment is shown in Fig. 2.5 and the results for the efficiency are presented in Fig. 2.6.

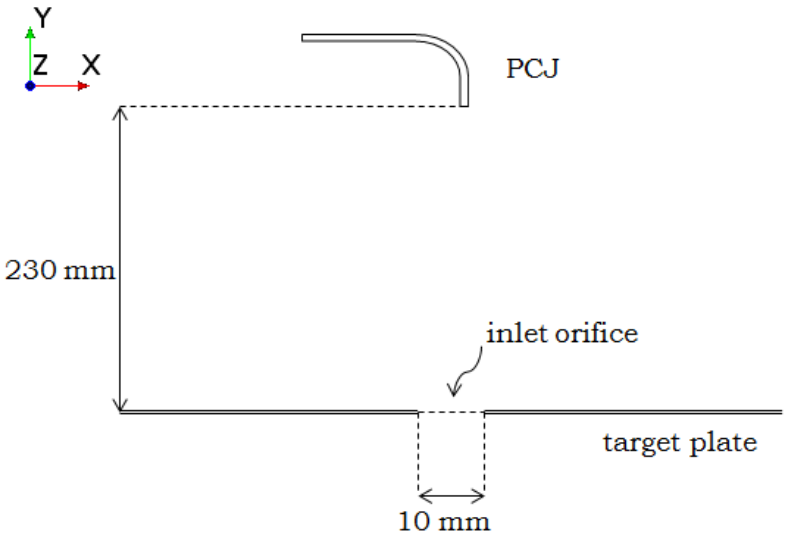

Figure 2.5: Setup of the experiment performed at DAF to determine mass flow efficiency.

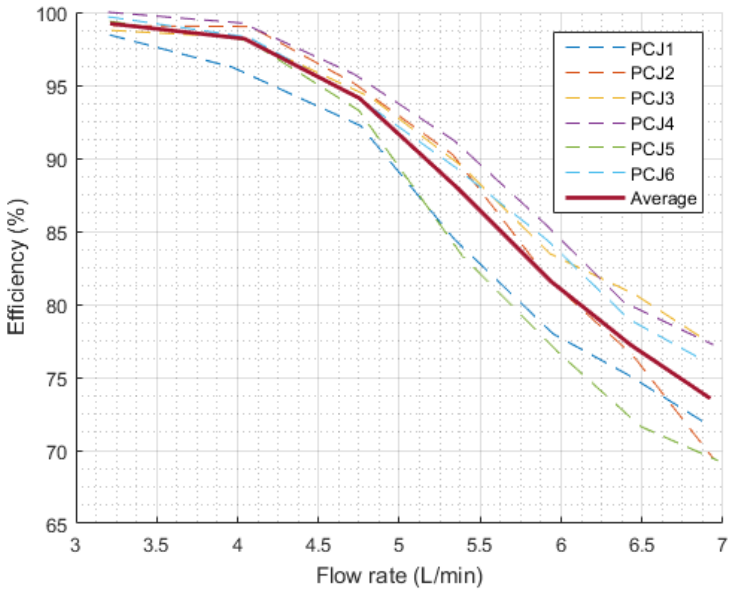

Figure 2.6: Results of the flow rate efficiency experiment by DAF, performed for 6 different MX-13 piston cooling jets.

It can be seen that the experiment is performed for downward facing jets, whereas the jets are upward directed

in reality. The effect of gravity is not mentioned in the documentation of the experiment. Nevertheless, it is clear that the flow rate efficiency decreases as the flow rate increases, which is an indication of the increasing spreading behaviour of the jet. The results are thus in accordance with the effects observed for the results of Moghe and Janowiak: with increasing Reynolds number (or flow rate), there is an increase of spreading, and thus a decrease of the flow rate efficiency.

Further it can be seen that the deviations with respect to the averaged results are increasing with increasing flow rates. This behaviour can be caused by two reasons: the first reason could be the small geometrical differences between the 6 nozzles tested in the experiment. These nozzles are provided by a supplier, which needs to produce these nozzles within certain tolerances, and it could very well be that these small geometrical differences are causing the deviating results for higher flow rates. Another reason could be the fact that with increasing flow rate the jet becomes more and more turbulent, resulting in an increasing chaotic and uncorrelated behaviour of the jet. It could be that the run time of the experiment was too short, and that a longer run time could eliminate or decrease the deviations.

2.2. Impingement

The second research area that is reviewed in this chapter is the impingement of free-surface liquid jets and the heat transfer characteristics related to this. Jet impingement offers a relatively simple but effective solution to remove excessive heat loads. It is widely used in industrial cooling or heating applications. Mostly air is used as the working fluid, resulting in a large amount of available literature related to gas jet impingement. Using liquids as the working fluid can increase the heat transfer capabilities by several orders [8], therefore liquid jet impingement is studied more and more in recent years. As was the case for liquid jets, only free-surface liquid jet impingement is considered in this chapter.

2.2.1. Heat Transfer

Heat transfer can be classified into three modes of heat transfer: conduction, convection and radiation. In the total piston cooling process all of these modes play a role. Radiation and convection are the dominating modes when heat is exchanged during the combustion process. However, this process takes place on the upper side of the piston, and therefore not relevant for the current project. On the lower side of the piston, where the piston cooling takes place, the relevant modes are conduction and convection and only these are discussed next.

Conduction

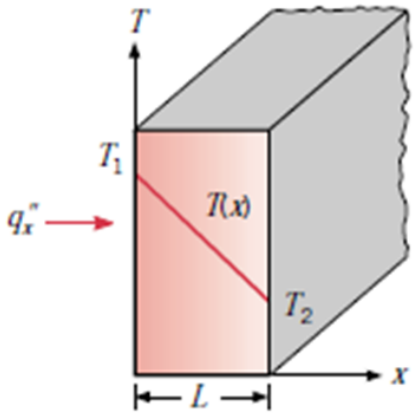

Figure 2.7: Example of one-dimensional conduction [7].

Conduction is the heat transfer in a stationary medium. It can also be seen as the transfer of energy from the more energetic particles to the less energetic ones. A particle with a higher temperature contains more

energy than one with a lower temperature. Thus after a collision of two particles with a different temperature, naturally an energy transfer occurs between the particles. Conduction can occur in solids, liquids and gasses [7]. An example of one-dimensional conduction is shown in Fig. 2.7.

The quantification of this mode can be done by using Fourier's Law, that can be expressed for one-dimensional conduction (in x-direction) as:

$$q''_x = -k\frac{dT}{dx}. \tag{2.6}$$

Where q''_x (W/m^2) is the heat transfer rate per unit area in the x-direction, and is proportional to the temperature gradient in the same direction. k $(W/m.K)$ is the thermal conductivity of the medium.

In the piston cooling problem, conduction takes place inside the piston. The temperature difference between the upper and lower side of the piston results in an energy transfer from the warmer parts to the colder parts. This heat transfer mode can be considered as relatively simple, as it is depending only on the temperature difference and the thermal conductivity of the piston material.

Convection

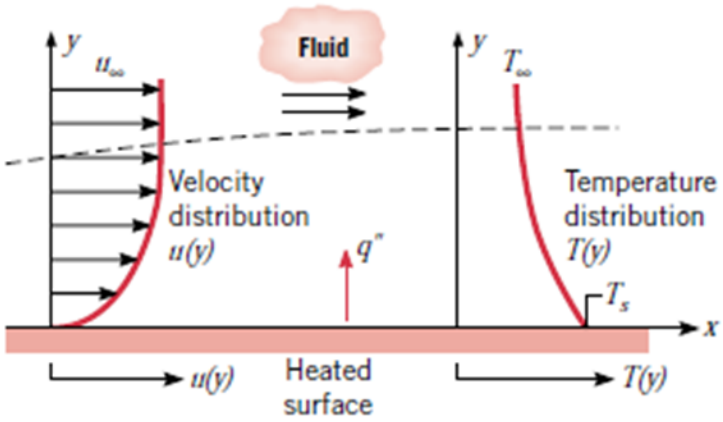

Figure 2.8: Example of one-dimensional convection [7].

When a cold fluid flows along a hot surface, a thermal boundary layer is formed on the surface, as can be seen in Fig. 2.8. Similar to the velocity distribution in a momentum boundary layer, there is a temperature distribution inside the thermal boundary layer that varies between the hot surface temperature and the cold fluid temperature. The thickness of the thermal boundary layer δ_T is defined as the thickness for which $(T_s - T)/(T_s - T_\infty) = 0.99$, with T_s as the surface temperature, T_∞ as the fluid temperature far from the wall and T as the varying temperature in the thermal boundary layer. The thermal and momentum boundary layer are related through the Prandtl number (Pr), which is a dimensionless number defined as the ratio of momentum diffusivity to thermal diffusivity [7]:

$$Pr = \frac{c_p \mu}{k} \tag{2.7}$$

The relation between the thermal boundary layer thickness and the momentum boundary layer thickness can then be estimated by [7]:

$$\frac{\delta}{\delta_T} = Pr^{1/3}. \tag{2.8}$$

In the convection mode, two mechanisms are involved: the heat transfer at the surface and the heat transfer due to the bulk motion of the flow. When assuming a hot surface and a colder moving fluid, the liquid at the surface is heated purely by conduction, because the velocity of the flow at the surface is zero (no-slip condition), and this layer of fluid can be considered as a stationary medium. The contribution of the bulk motion comes from the fact that the boundary layer grows and the transferred heat is swept away with the fluid motion [7].

The rate equation for convection is known as Newton's law of cooling:

$$q'' = h(T_s - T_\infty). \tag{2.9}$$

Where h ($W/m2K$) is the heat transfer coefficient (HTC), depending on conditions in the boundary layer, surface geometry, the nature of the fluid, and an assortment of fluid thermodynamic and transport properties [7]. With all these dependencies, the HTC is a very complex coefficient. Any study of convective heat transfer is therefore a study where the HTC needs to be determined, because of the complexity of this parameter. Eq. (2.6) can be used to quantify the heat flux at the surface (conduction):

$$q_s'' = -k_f \frac{dT}{dy}, \tag{2.10}$$

with q_s'' the heat flux at the surface, k_f the thermal conductivity of the fluid, and y the normal direction on the surface.

As mentioned, this only holds for the liquid with zero velocity on the surface. For the next layer of fluid, which has a non-zero velocity, the heat flux is given by Eq. (2.9):

$$q_S'' = h(T_s - T_\infty). \tag{2.11}$$

These two fluxes are equal, resulting in the following expression for the convective heat transfer coefficient h:

$$h = -\frac{k_f dT/dy}{T_s - T_\infty}. \tag{2.12}$$

Since the thermal and velocity boundary layer thickness increase along the surface, the temperature gradient dT/dy decreases, and thus the heat transfer coefficient decreases as the flow passes over a surface.

For the piston cooling process convection is the dominant heat transfer mode. After the oil jet impinges onto the lower surface of the piston (in spray cooling), it starts to radially spread out and starts to form a boundary layer on the surface of the piston. This is similar to a fluid moving with a finite velocity over a surface. The amount of heat transferred by the oil jet can be estimated with correlations derived in past studies. These are discussed in the following section.

2.2.2. Flow Field Predictions

In this section, two benchmark studies on axisymmetric liquid jet impingement are shortly discussed. The results of these studies are often used to compare jet impingement results with. The first study is an analytical study performed by Ma, et al. [8]. In this study, the researchers divide the flow field after impingement into several regions and for each of these regions they present correlations for the momentum boundary layer thickness and the heat transfer. The second study is an experiment performed by Stevens and Webb [9]. They investigated the effect of the Reynolds number, the nozzle diameter and the target distance on the heat transfer between a flat plate and an axisymmetric impinging liquid jet. Both cases are discussed in detail next.

Ma, et al. (1996)

An axisymmetric jet after impact creates a radially spreading flow, that can be schematically presented as given in Fig. 2.9. It should be noted that the thickness of the sheet after hitting the wall is not in scale in this figure: in reality this sheet is much thinner than the diameter of the jet. The radially spreading flow field can be divided into several regions according to [8].

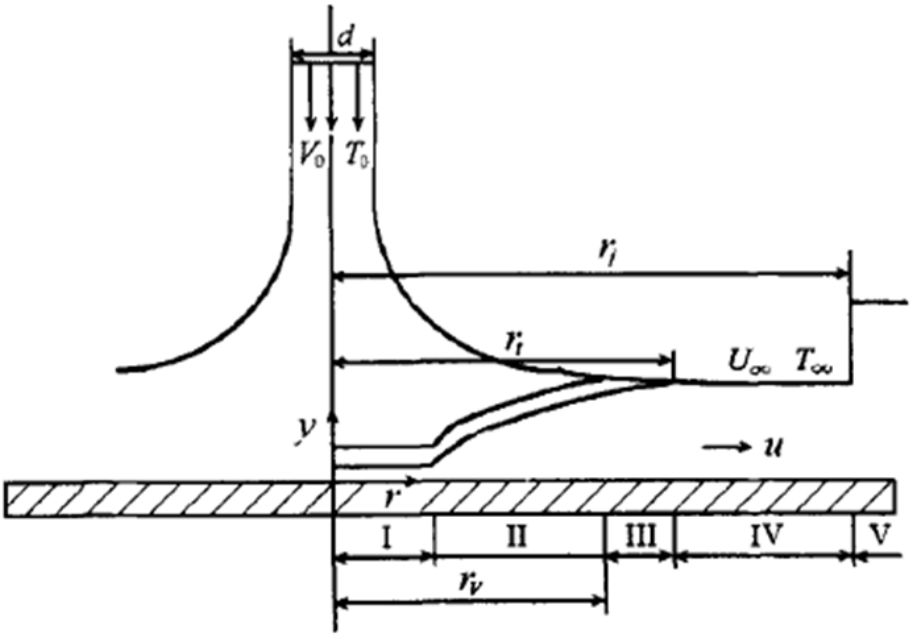

Figure 2.9: Division of the flow field after impingement [8].

Analytically derived expressions for the (momentum) boundary layer thickness and the heat transfer are given below for each of the regions in Fig. 2.9. The thermal boundary layer thickness can be determined with the momentum boundary layer thickness and the Prandtl number, using Eq. (2.8). The heat transfer is given in the form of the Nusselt number. The Nusselt number is the ratio between the convective and conductive heat transfer across a boundary:

$$Nu = \frac{hd}{k}. \tag{2.13}$$

All expressions are obtained from [8], unless stated otherwise. For a more elaborate explanation or the derivation of the expressions, the reader is referred to [8].

Region I

This is the stagnation zone, where the jet velocity decreases to zero and a very thin – constant – boundary layer is formed. The flow field in this region can be described by the classical stagnation zone boundary layer theory [23][9]. This theory states that the flow field can be split up into an inviscid outer layer and a viscous boundary layer. To determine the flow field in the viscous boundary layer, first the inviscid outer layer needs to be solved. When a flow is inviscid and irrotational, this can be done by using potential flow theory [23].

The result for the boundary layer thickness in the stagnation zone derived by Ma, et al. is:

$$\frac{\delta}{d} = 2.69246 Re^{-0.5}, \tag{2.14}$$

where δ is the momentum boundary layer thickness, d is the diameter of the jet at the nozzle exit and Re is the Reynolds number at the nozzle exit.

As discussed in Section 2.2.1, the convective HTC is inversely proportional to the normal temperature gradient on the surface. Since the boundary layer in the stagnation zone is extremely thin, there is a large temperature gradient. As the jet moves over the surface, the boundary layer thickness increases, and the CHT decreases. Therefore, the highest Nusselt numbers occur in the stagnation zone. Nu_0 can be estimated by:

$$Nu = 0.8597 Pr^{1/3} Re^{0.5}. \tag{2.15}$$

The stagnation zone is assumed to start at $r/d = 0$ and end at $r/d = 0.787$ [31].

Region II

In this region it is assumed that a laminar boundary layer starts to develop. The velocity outside the boundary layer remains constant. The growing momentum boundary layer thickness is now a function of r/d and can be estimated by:

$$\frac{\delta}{d} = 2.6795 \left(\frac{r}{d}\right)^{0.5} Re^{-0.5}. \tag{2.16}$$

The local Nusselt number in region II can be predicted by using the following equation:

$$Nu = 0.668 Pr^{1/3} Re^{0.5} \left(\frac{r}{d}\right)^{-0.5}. \tag{2.17}$$

Region II ends when the momentum boundary layer reaches the liquid surface, which is at radial position r_v:

$$r_v = 0.1773 Re^{1/3}. \tag{2.18}$$

Region III

After the momentum boundary layer reaches the liquid surface, the entire liquid sheet behaves as a thick boundary layer. The outer velocity is now part of the momentum boundary layer and thus not constant anymore [8]. The velocity at the surface decreases with r/d:

$$\frac{u_\infty}{v_0} = \frac{1}{25.735 \left(\frac{r}{d}\right)^3 \frac{1}{Re} + 0.8566}. \tag{2.19}$$

The momentum boundary layer thickness, which is now the same as the liquid sheet thickness, is given as:

$$\frac{\delta}{d} = \frac{5.147}{Re} \left(\frac{r}{d}\right)^2 + 0.17132 \frac{d}{r} \tag{2.20}$$

The Nusselt number solution for this region is:

$$Nu = 1.5874 Pr^{1/3} Re^{1/3} \left(\frac{25.735}{Re} \left(\frac{r}{d}\right)^3 + 0.8566\right)^{-2/3} \tag{2.21}$$

Region IV

It can be seen in Fig. 2.9 that region III ends when the thermal boundary layer reaches the liquid surface. It is given by [8] that liquids with $Pr > 9.7$ will never reach the liquid surface and region IV is not existing for these liquids. The working fluid in this thesis is engine oil with a Prandtl number of $Pr > 100$, therefore the equations for region III are valid for region IV as well.

Region V

This region only occurs in the case of a vertical jet impinging downwards onto a horizontal surface, where the liquid sheet is abruptly slowed down and the thickness of the sheet suddenly increases. This phenomenon is called the hydraulic jump. Knowledge about hydraulic jumps is relatively limited, however [8] provided an expression for the radius at which the jump occurs. In this thesis, upward facing jets are considered only, which means that a hydraulic jump cannot occur and the fluid will simply fall down because of gravity. The reader is referred to relevant literature for more information about hydraulic jumps [8].

Stevens and Webb (1991)

The second study is an experiment, aiming to determine the effect of the Reynolds number, the nozzle diameter and the target distance on the heat transfer. The working fluid used in the study is water, therefore the tested Reynolds number are much higher than the Reynolds numbers considered in this project. However, they included a Prandtl number dependency in their results, which makes it possible to use their correlations for other liquids as well. A similar dependency on the Prandtl number was already observed in the results of Ma, et al.

The researchers present three correlations, two for the stagnation point Nusselt number and one for the local Nusselt number profile along the surface:

$$Nu_0 = 2.67 Re^{0.567} Pr^{0.4} (L/d)^{-0.0336} (v/d)^{-0.237}, \tag{2.22}$$

$$Nu_0 = 1.51 Re^{0.44} Pr^{0.4} (L/d)^{-0.11}, \tag{2.23}$$

$$Nu/Nu_0 = a e^{b(r/d)}. \tag{2.24}$$

The values for the coefficients in Eq. (2.24) are depending on the nozzle diameter and are listed in Table 2.5.

Table 2.5: Correlation coefficient for the local Nusselt number [9].

d (mm)	2.2	4.1	5.8	8.9
a	1.15	1.34	1.48	1.57
b	-0.23	-0.41	-0.56	-0.70

Eq. (2.22) is the first correlation for Nu_0, and predicts the experimental data of Stevens and Webb with an average and maximum error of respectively 5 and 14 percent. It can be seen that this equation contains a dimensional term, v/d. The researchers found that there is a diameter dependency for Nu_0, and a way to include the diameter dependency was by using the radial velocity gradient, du/dr. However, they had difficulties to measure this quantity and used v/d instead, as an approximation of the radial velocity gradient. Since there is no obvious time scale that can be used to non-dimensionalise this term, they kept the dimensional term in the correlation. The downside of using this term is that, for v/d combinations outside the tested range of v/d values, the effect of this term can negatively influence the prediction of the Nusselt number.

The second correlation (Eq. (2.23)) is derived without the dimensional term and the researchers mention that this correlation is less accurate than the first correlation (for their own experimental data). The average and maximum error for Eq. (2.23) is respectively 15 and 60 percent. It can be seen that the exponents of the parameters have changed after dropping the dimensional term v/d out. This correlation is more similar to the correlation derived by Ma, et al. for the stagnation zone (Eq. (2.14)). The main difference is that the effect of the nozzle-to-target distance is not included in Eq. (2.14). The expectation is therefore that the correlations of Stevens and Webb are slightly more accurate. However, Stevens and Webb performed their experiment for a maximum L/d of 35, whereas the L/d values in this project are between 26 and 77 (for the BDC and TDC locations of the piston).

2.2.3. Effect of Problem Parameters

The two studies discussed before are performed for a relatively simple situation, where an axisymmetric liquid jet impinges onto a flat surface. The piston cooling problem itself is much more complex and these studies can only be used to obtain crude estimations of the heat transfer. Effects of parameters that are not considered in the two mentioned studies are discussed shortly in this section.

Turbulence

In most real life conditions the liquid jets are turbulent. Even though the flow can be considered as laminar flow after impingement, there is a significant difference in heat transfer coefficients between laminar and turbulent jets. Turbulent jets can increase the heat transfer coefficient up to 50% [23]. The turbulence in a jet is carried into the wall bounded flow after impingement, and disturbs the boundary layer, enhancing transition and thus increasing the heat transfer.

The critical Reynolds number above which a liquid jet can be considered as a turbulent one is around 4000 [23]. When looking at the Reynolds number of the DAF jets, the lowest Reynolds number considered is just below this critical value, whereas the highest Reynolds number is just above it. The expectation is therefore that the heat transfer will increase with increasing turbulence.

Nozzle-to-target distance

The nozzle-to-target distance is often used a problem parameter, hereby normalised with the jet diameter. For submerged jets this parameter is very important because of the large entrainment and interaction of the jet with the surroundings. For free-surface jets it is less important, as can be seen in Fig. 2.10. Stevens and Webb found that the Nusselt number decreases slightly with increasing nozzle-to-target distance [9].

The figure shows that the target distance dependency is relatively small. The maximum tested dimensionless target distance is around L/d = 30, which is much smaller than the distances considered in this project (L/d = 78 - 230). It is expected that for this range of distances the effect is much more significant, and this investigation is part of the research.

Oblique Jets

The expressions presented before are derived for jets that hit the surface perpendicularly. The Nusselt number distribution and thus the heat transfer distribution along the wall are therefore axisymmetric. When the jet hits the surface with an inclination, the Nusselt number distribution changes and it loses its symmetry. The inclination angle (θ) is defined as the angle between the jet and the target surface, as is shown in Fig. 2.11.

Ma, et al. found that the maximum Nusselt number decreases with inclination angle, according to the following equation [10]:

$$Nu_{max} = CPr^{0.33}Re^{0.5}. \tag{2.25}$$

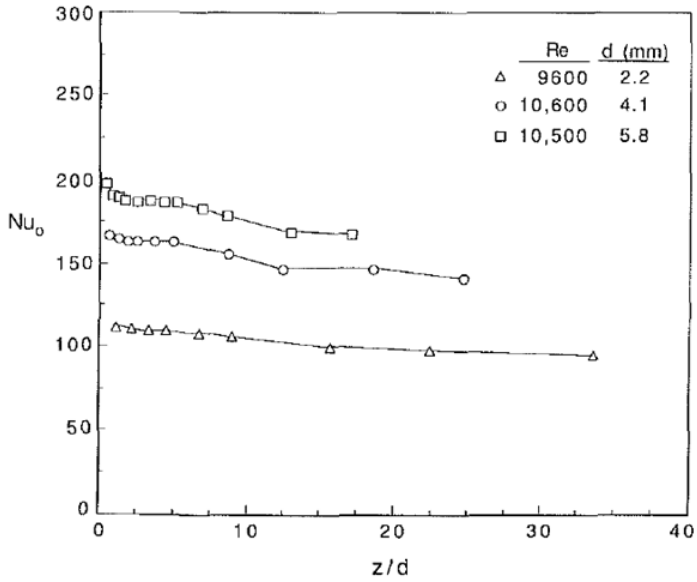

Figure 2.10: Effect of target distance on the stagnation zone Nusselt number by [9], with z/d as the non-dimensional target distance (L/d).

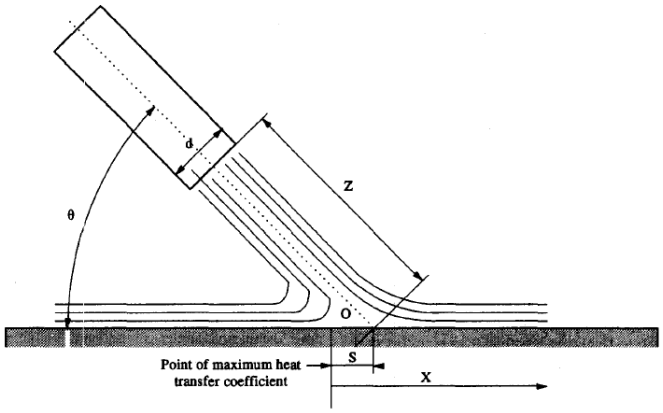

Figure 2.11: Definition of the inclination angle θ.

The coefficient in the equation depends on the inclination angle and its values are given in Table 2.6.

Table 2.6: Coefficients for different inclination angles, by [10]

θ [deg]	90	75	60	45
C	1.26	1.22	1.09	0.986

Besides a decrease in value of the maximum Nusselt number, there also occurs a shift in the location of the maximum Nusselt number. The correlation for this shift is given as [10]:

$$s/d = (0.119 + 0.00454\theta)cos\theta \tag{2.26}$$

It can be seen in Fig. 2.12 that decreasing the inclination angle results in the Nusselt number losing its symmetrical property. The Nusselt number profile is dropping down much more rapidly on the upstream side than on the downstream side. This can be explained by the positive dependence of the Nusselt number on the Reynolds number. Since the velocities on the downstream side are higher than the velocities on the upstream side, the Nusselt number is higher here. This effect increases with decreasing inclination angle.

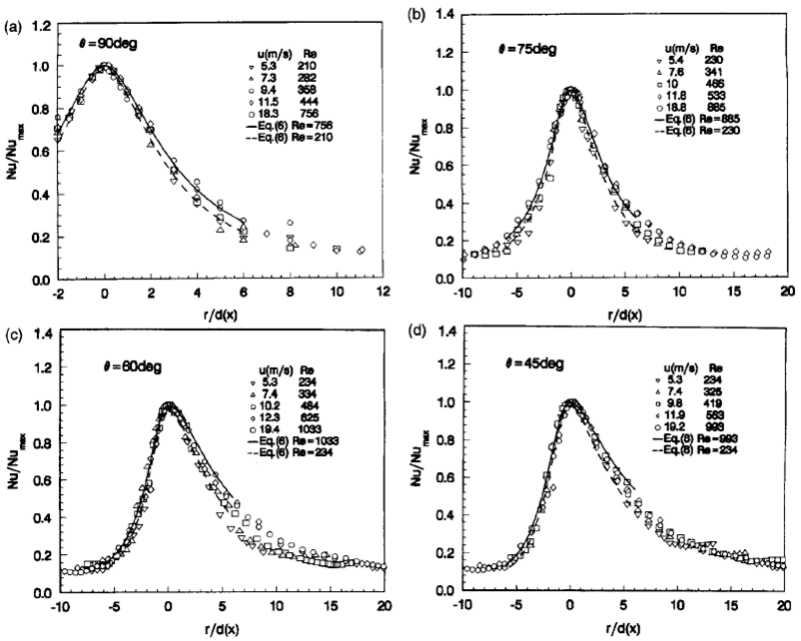

Figure 2.12: Effect of inclination angle on the Nusselt number distribution [10].

The effect of oblique jets is particularly interesting for the spray cooling method. As was shortly mentioned in the introduction, the lower surface of a piston used with spray cooling is curved and since the impingement is on the side of the piston, there is an inclination effect. For the gallery cooling method, the effects of an inclined impingement is less interesting. The cooling method itself is already very complex and it is not within the scope of this project to analyse the effect of inclined impingement for the complex flow inside the cooling gallery.

Surface Roughness

Another parameter of interest is the wall surface roughness. It is stated before that turbulence enhances the heat transfer, therefore wall roughness is expected to affect the heat transfer as well. The effect of wall roughness is investigated by Gabour [11] and the results are displayed in Fig. 2.13. The Nusselt number is measured for a water jet impinging onto different surfaces. The roughness of the surface is labelled in the figure as S1-S10, with S1 the smoothest surface and S10 the roughest surface.

It can be seen that the Nusselt number increases with increasing surface roughness. This can be explained by the fact that for rough elements, the boundary layer gets disrupted more and thus the turbulence level inside the boundary layer is increased, resulting in a higher heat transfer. The roughness is measured as a vertical distance relative to the boundary layer thickness, and therefore the effect is larger for larger Reynolds number, where thinner boundary layers are formed and the roughness is thus relatively larger than for a thicker boundary layer.

The DAF pistons are manufactured by a third party, and specific demands on surface roughness are only there for the combustion side of the piston. For the lower surface there are no demands or certain specifications, and the surface roughness here is thus unknown. The effect of surface roughness could be a valuable investigation for DAF, since it is expected to be a relatively simple way of increasing the heat transfer.

Concave Surfaces

The lower surface of a piston is not flat, and therefore the effect of the curvature needs to studied. The literature related to curved surface impingement is mostly related to air, and very few literature is available for liquid jets. Nevertheless, the main effects can be investigated and qualitative conclusions can be drawn.

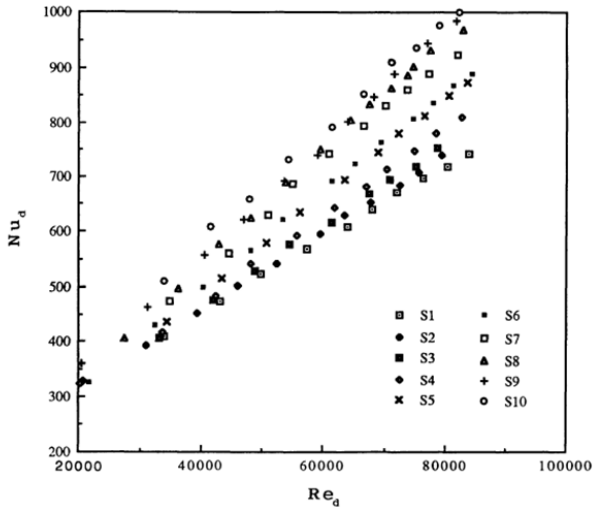

Figure 2.13: Surface roughness effect on stagnation point Nusselt number [11].

Mostafa [32] states that the flow structure after impingement is unsteadier for concave surface impingement than the impingement on flat or convex surfaces. Thomann [33] studied the heat transfer characteristics of concave surface impingement and found that the heat transfer was around 20% higher for concave surface impingement than for a flat surface. A possible reason is given by Thomann to be the destabilisation of the boundary layer because of the concave shape of the target. This in turn increases the turbulent mixing, which results in the production of large scale Taylor-Gortler vortices, shown in Fig. 2.14. These vortices are known to enhance momentum and energy transfer and thereby thus heat transfer from the concave surface [34].

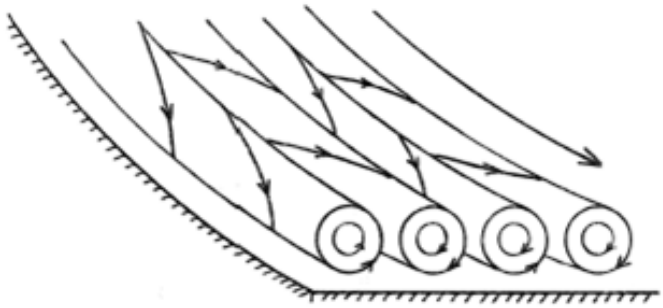

Figure 2.14: Example of Taylor-Gortler vortices after impingement onto a concave surface [12].

Piston motion

The major difference between the discussed cases and the actual piston cooling is the reciprocating motion of the piston. In order to accurately investigate the effect of motion, a transient CFD simulation is needed. Such an analysis is performed by Nasif, Barron and Balachandar [17]. They performed an analysis on a smaller gasoline piston, by determining the cycle-averaged temperature distribution on the piston surface. They compared these results to the temperature distribution obtained for a stationary piston. Their results show that the average temperature of their piston in a stationary configuration is between 192 and 194.5 $°C$, and that the cycle-averaged and surface-averaged temperature for a moving piston is 192.5 and 190.5 $°C$, for angular velocities of respectively 210 and 630 rad/s.

From this study it can be concluded that the effect of the motion is small. However, there is no proper validation presented in their work and therefore these results can not be considered as reliable and an investigation needs to be done in order to determine the effect of piston motion in a more accurate way.

2.3. Piston cooling

The two piston cooling techniques presented earlier in this thesis are the spray cooling and gallery cooling technique. In this section, several studies performed on these piston cooling techniques are discussed.

2.3.1. Spray cooling

The correlations presented in Section 2.2.2 are derived for liquid jet impingement onto a flat heated plate surface, which can be seen as a simplified version of spray cooling. Main differences are the more complex piston geometry, the longer target distances and the piston motion that are involved in spray cooling. Therefore these correlations can at most be used to make crude estimations for the heat transfer.

What may be a better way of making predictions for the spray cooling technique is by using correlations obtained from actual spray cooling experiments. Easter, et al. [18] indicate in their study that there is little engineering value in determining the local Nusselt number distribution, because of the highly complex and irregular undercrown geometry of the piston and the significant spatial variations in heat transfer. A more valuable output parameter is the area-averaged Nusselt number. Their correlation for Nu_{avg} is as follows:

$$Nu_{avg} = 0.028 Re^{0.652} Pr^{0.4} (L/d)^{-0.034}. \tag{2.27}$$

for ranges of validity of: $100 < Re < 4{,}500$, $90 < Pr < 750$, and $45 < L/d < 95$. It can be seen that the correlation is very similar to the correlations presented for the impingement onto the flat plate. This correlation can be used to make predictions for the DAF conditions, as is shown in Table 2.7.

Table 2.7: Prediction of Nu_{avg} for the DAF jets by using Eq. (2.27).

	Nu_{avg} (-)
6 L/min / BDC	40
8 L/min / BDC	48
6 L/min / TDC	38
8 L/min / TDC	46

2.3.2. Gallery cooling

The correlations presented for impingement heat transfer are less useful for a piston with a cooling gallery, since the motion of the flow is now dominated by the reciprocating motion of the piston. There is no flat or near-flat surface that is covered with oil in gallery cooling. The impingement surface is confined by the cooling gallery walls and thus the flow can not radially spread over the surface. The flow is decelerated by the walls of the gallery, and the behaviour of the flow is dominated by the reciprocating motion of the piston.

As mentioned before, this cooling technique is the one applied to the DAF engine pistons, and is known to be a better cooling technique than the spray cooling technique. A comparison between the two techniques for different power outputs is illustrated in Fig. 2.15. It can be seen that below a specific power of 50 kW/L, the maximum piston temperature is higher in spray cooling than in gallery cooling. One of the reason for the higher cooling effectiveness of gallery cooling is the larger surface area that is directly touched by the cooling oil and the much shorter heat flow paths from the hot side to the cold side of the piston.

According to Pan, et al. [14], the most important parameter of piston gallery cooling effectiveness is the oil fill ratio (OFR), defined as the ratio between the volume of the oil in the gallery and the volume of the total gallery, over one motion cycle. This ratio increases when the piston moves downwards, as the relative velocity between the gallery and the jet increases. Also, there is almost no outflow from the gallery when the piston moves downwards. When the piston moves back up, the OFR decreases again. Of course the behaviour of the OFR over a stroke depends on the design of the system (flow rate of oil, piston geometry, cooling gallery design). A typical variation of the OFR over one stroke is given by [14] in Fig. 2.16.

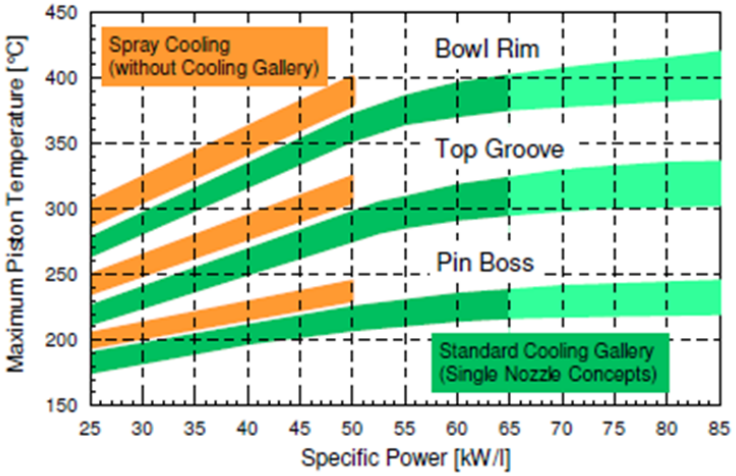

Figure 2.15: Comparison of spray cooling and cooling with cooling gallery[13].

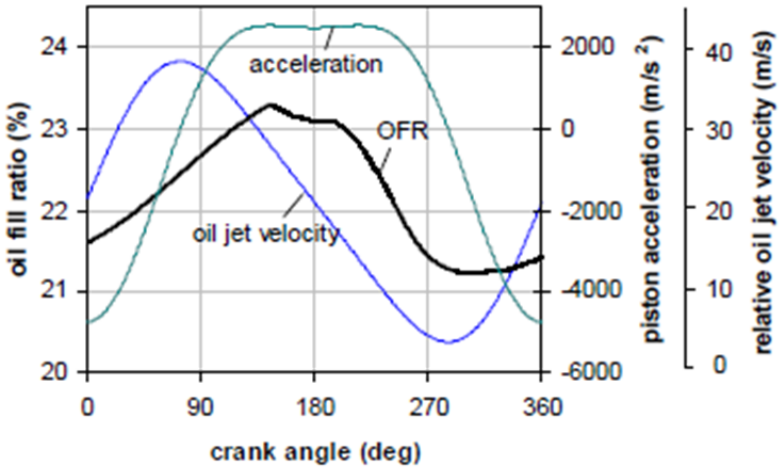

Figure 2.16: Variation of the OFR over one motion cycle of the piston [14].

Pan *et al.* also performed a study on the actual effect of the OFR on the heat transfer. The results of this analysis can be seen in Fig. 2.17. They divided the cooling gallery into several areas, as is also included in the figure. The most critical areas are the ones that form the top surface, thus areas 1, 2, 3 and 7. It can be seen from the figure that for these areas the most effective OFR would be between 30% and 80%. These results are obtained for one gallery design and a constant jet flow, therefore they can not be used to make predictions for the gallery cooling process of the DAF pistons. However, since the analysis is similar, the study can be used as an example for the development of a CFD methodology and CFD model.

2.4. Computational fluid dynamics

Computational Fluid Dynamics or CFD is a method to study fluid dynamics in a controlled environment, by solving the three fundamental conservation equations. These equations are the conservation equations for mass, momentum and energy, also referred to as the Navier-Stokes equations. For Mach numbers lower than 0.3 the flow can be considered as incompressible flow [35] and this means that density variations can be considered small enough to neglect them. The incompressible flow assumption is justified in the current

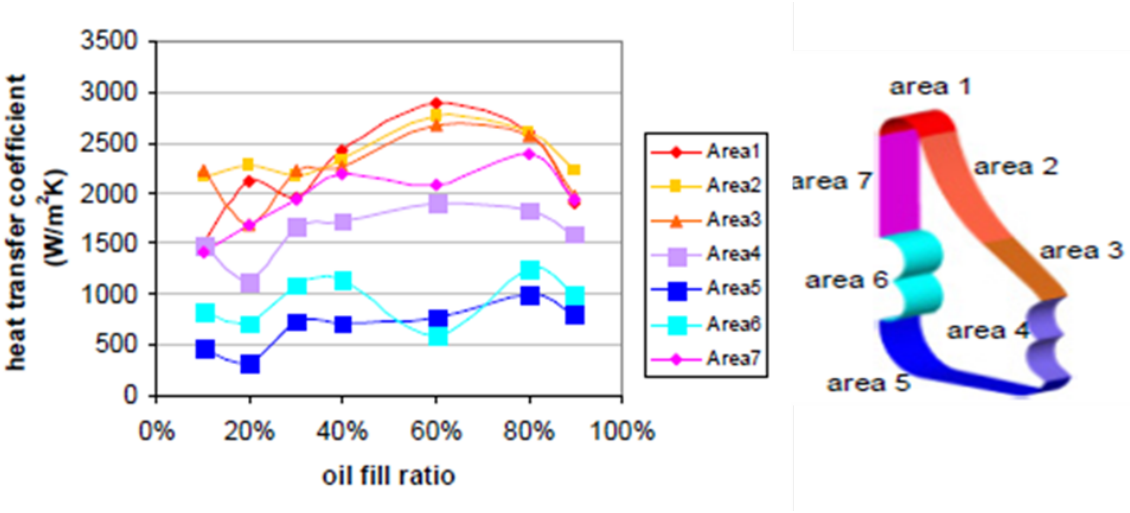

Figure 2.17: Effect of OFR on the heat transfer for different areas of the cooling gallery [14]

project, since the Mach number is much lower in liquids compared to air and the velocity range expected in this problem is safely in the incompressible regime. For oil at 100 °C, a Mach number of 0.3 corresponds to a velocity of around 400 m/s, which is much higher than the considered velocity range.

2.4.1. Incompressible Equations of Motion

The equation for conservation of mass, also referred to as the continuity equation, states that the rate of increase of mass in a fluid element is equal to the net rate of flow of mass into that fluid element. The unsteady, three-dimensional mass conservation equation at a point is given by [36]:

$$\frac{\partial u_i}{\partial x_i} = 0, \tag{2.28}$$

with u_i the velocity component in the x_i direction.

The second conservation law is the conservation of momentum. Newton's second law states that the rate of change of momentum of a fluid particle equals the sum of forces on that particle:

$$\frac{\partial u_i}{\partial t} + u_j \frac{\partial u_i}{\partial x_i} = -\frac{1}{\rho}\frac{\partial p}{\partial x_i} + \nu \frac{\partial^2 u_i}{\partial x_j^2}, \tag{2.29}$$

with p the pressure and ν the kinematic viscosity.

The final equation of the incompressible Navier-Stokes equations is the equation for conservation of energy equation, assumed that the flow is thermally perfect and the flow is heat-transfer dominated (enthalpy changes >> kinetic energy) [37]:

$$\frac{\partial T}{\partial t} + u_j \frac{\partial T}{\partial x_j} = a \frac{\partial^2 T}{\partial {x_j}^2}, \tag{2.30}$$

with T the temperature and a the thermal diffusion coefficient. This equation is also called the heat-convection-diffusion equation.

2.4.2. Turbulence

It was shown in Section 2.2 that the Reynolds number of the jets considered in this study vary around the critical Reynolds number (Re = 4000) [23]. There are three methods to deal with turbulence in CFD, which are discussed next.

Direct Numerical Simulation (DNS)

The exact solution to any turbulent problem can, in theory, be found by using the Navier-Stokes equations. This way all length scales and time scales are resolved in an exact way. The major drawback of DNS is the high computation costs, which can be estimated by estimating the number of grid points and time steps needed to resolve the smallest scales. Kolmogorov predicted in 1941 with his theory of homogeneous, isotropic turbulence that the smallest scales exist down to $O(Re^{-3/4})$, resulting in $N = Re^{9/4}$ grid points for a 3D simulation [38]. Even with current possibilities, DNS is therefore only suited for small, low Reynolds number problems and major developments in computer hardware are needed before DNS can be applied to larger problems with higher Reynolds number. For these reasons, DNS is not considered in this thesis.

Large Eddy Simulation (LES)

LES is a method where only the largest turbulent scales are resolved, whereas the small scales (eddies) are modelled. The idea behind this method is that, because the largest eddies contain most of the energy, they determine the main flow dynamics. The large eddies are known to be produced by external energy inputs and they depend on the geometry and boundary conditions of the model. The smallest eddies however are assumed to be isotropic and similar in all turbulent flows. The flow is thus decomposed in resolved scales and unresolved (modelled) scales. The boundary at which a scale is resolved or modelled is determined by a spatial filter, which is mostly the grid size. Although the computational expense is much lower compared to DNS, it can still be considered as excessive [16].

A proper LES simulation needs to meet several requirements in order to produce reliable results. The first requirement is that the cut-off scale needs to be small enough. When this is too high, the assumption of isotropic small scales is not valid and the results will be affected. A way to check if the cut-off scale is small enough is by checking the LES quality metric, which is an indication of the ratio between the resolved turbulent kinetic energy and the modelled turbulent kinetic energy [6]. The LES quality metric is defined as:

$$\gamma = \frac{TKE_{resolved}}{TKE_{resolved} + K_{SGS}}, \tag{2.31}$$

with K_{SGS} the kinetic energy of the subgrid scales (SGS). The LES quality metric needs to be above 0.8 according to [39].

Once a suitable mesh size is selected, a corresponding time step needs to be selected, that is small enough to maintain a sufficiently small Courant–Friedrichs–Lewy (CFL) number. The CFL number is defined as:

$$CFL = \frac{v\Delta t}{\Delta x} \tag{2.32}$$

with v the maximum velocity in the region of interest, Δt the time step and Δx the grid size in the region of interest. For LES, it is recommended in [16] to keep the CFL number below 1, such that fluid properties are convected not more than one cell size per time step.

Another reason why LES can be time consuming is the initialisation and sampling stages that need to be performed. In the initialisation stage, the flow develops from the initial conditions to a stage for which it is possible to collect flow statistics from. The effect of initial conditions needs to eliminated before this is possible. This stage takes usually around 2-5 flow through cycles [16]. A flow cycle is defined as the time

between the moment when a particle enters the domain and leaves the domain. The duration of this stage can be reduced by using better initial conditions and by monitoring the behaviour of relevant flow parameters. Once the initial condition effect is eliminated, the sampling stage can start. This is when the parameters of interest are sampled and statistical data is collected. This stage also takes around 2-5 flow through cycles [16].

It was shown in Section 2.1.3 that LES can be used for the simulation of the disintegration of free-surface liquid jets. The total computation time for those LES simulations was between 55 and 83 hours on 48 cores [6]. This is considered as acceptable and the use of LES can be considered for the simulation of the liquid jet. For the simulation of impingement and/or heat transfer this is not feasible, because of the high mesh requirements for wall-bounded flow[39].

For the modelling of the subgrid scales there are three SGS models available in Star-CCM+:

- **Smagorinsky Subgrid Scale model**
  The Smagorinsky SGS model is the original and most basic form SGS model, and uses a mixing length hypothesis to model the SGS stresses. A shortcoming of this model is that it contains a model constant C_s that is not universal and depends on the local flow conditions. Additionally, a damping function is needed for proper results in wall-bounded flows.

- **Dynamic Smagorinsky Subgrid Scale model**
  The Dynamic Smagorinsky SGS model has the same basic form as the Smagorinsky model, instead of using a single user-defined constant C_s, the model computes a local timevarying C_s value by test-filtering the flow field at a length scale greater than the grid length scale. This dynamic variation of the constant gives the model its name, and allows it to compute the correct result for wall-bounded flows without the use of damping functions.

- **WALE Subgrid Scale Model**
  The WALE (Wall-Adapting Local-Eddy Viscosity) SGS model is a more modern subgrid scale model that uses a novel form of the velocity gradient tensor in its formulation. Similar to the Smagorinsky Subgrid Scale model, it suffers from the limitation that the model constant C_w is not universal. But validations using STAR-CCM+ have shown that the WALE model is seemingly less sensitive to the value of the constant than the Smagorinsky model. Another advantage of the WALE model is that it does not require any form of near-wall damping: it automatically gives accurate scaling at walls. It is, therefore, the recommended SGS model by [16].

Reynolds Averaged Navier-Stokes (RANS)

The final method of dealing with turbulence is using RANS, which is the most common way in industry. This method is known for its simplicity and low computation cost. In RANS all the turbulent scales are modelled. First the fluid properties are decomposed into a mean and fluctuating part:

$$u_i = \bar{u}_i + u_i'$$
$$p_i = \bar{p}_i + p_i'$$

The averaging can be considered as a time-averaging for steady state simulations (RANS), and an ensemble-averaging for transient simulations (URANS), as is depicted in Fig. 2.18.

After substitution of the decomposed parameters in the Navier-Stokes equations and after applying an averaging operator, the incompressible Reynolds Averaged Navier-Stokes (RANS) equations are obtained:

$$\frac{\partial \bar{u}_i}{\partial x_j} = 0 \tag{2.33}$$

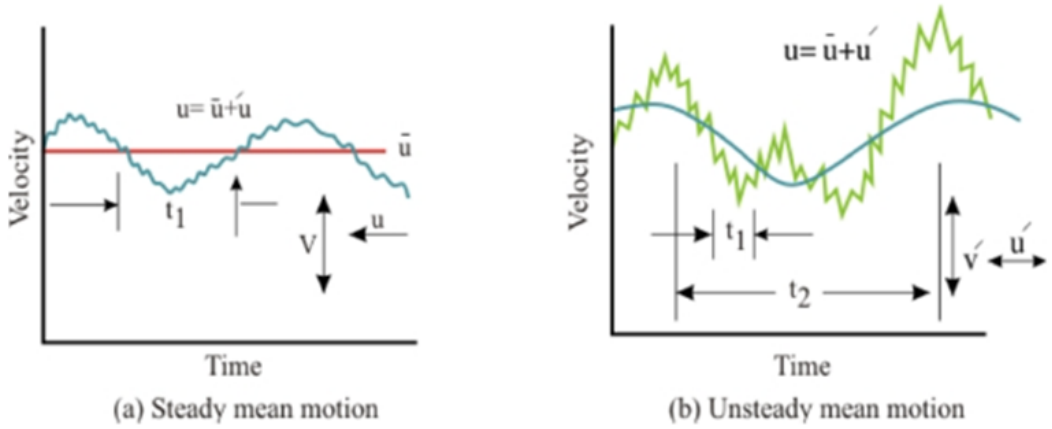

Figure 2.18: Representation of (a) RANS and (b) URANS modelling [15].

$$\frac{\partial \bar{u}_i}{\partial t} + \bar{u}_j \frac{\partial \bar{u}_i}{\partial x_i} = -\frac{1}{\rho}\frac{\partial \bar{p}}{\partial x_i} + \nu \frac{\partial^2 \bar{u}_i}{\partial x_j^2} - \frac{\partial \overline{u_i' u_j'}}{\partial x_j}. \tag{2.34}$$

It can be seen that a new term appeared in the momentum equation as a result of the averaging $\left(\frac{\partial \overline{u_i' u_j'}}{\partial x_j}\right)$. This non-linear term, called the Reynolds Stress Tensor (RST), contains all the turbulent fluctuations and can be approximated by turbulence models. The accuracy of a RANS simulation is depending on how well the RST is modelled/approximated. This is mostly done by using turbulence models, which are discussed next.

It is observed that in literature mostly the k-ϵ model is used to model free jet flows [40][41][14], and the k-ω model is used for wall bounded flow or heat transfer problems [42][43][15][17]. Therefore only these turbulence models are discussed next.

k-ϵ model

Advantages [36]:

- Simplest turbulence model for which only initial and/or boundary conditions need to be supplied
- Excellent performance for many industrially relevant flows
- Well established; the most widely validated turbulence model

Disadvantages [36]:

- Poor performance in a variety of important cases such as:
  - unconfined flows
  - flow with large extra strains (curved boundary layers, swirling flows)
  - rotating flows
  - fully developed flow in non-circular ducts

k-ω model

Advantages [16]:

- Better performance for near-wall flow than the k-ϵ model
- Good performance for boundary layers under adverse pressure gradients
- Can be applied throughout the entire boundary layer

Disadvantages [16]:

- Sensitive to initial conditions
- Over-prediction of separation
- More difficult to converge than the k-ϵ model

k-ω SST model

Advantages [15]:

- Uses near-wall qualities of the k-ω model and the far-field qualities of the k-ϵ model
- Applies a limit on the shear stress in the occurrence of large pressure gradients
- Accurately predicts onset and extend of separation

Disadvantages [15]:

- Does not include compressibility
- Slightly over-predicts turbulence in regions with large normal strain, like stagnation regions
- Shares also some disadvantages of the k-ϵ and k-ω models

2.4.3. Multiphase Modelling

One of the challenges in this thesis project is to accurately model the multiphase interaction between the oil jet and the surrounding air, and the heat transfer between the oil jet and the piston surface. The desired multiphase model is one that is able to predict the temporal and spatial evolution of a liquid jet that exits from a nozzle into a still gas. For short target distances it was shown that there is not much interaction and the jet remains reasonably straight. For large target distances however, the interaction becomes more complex and therefore a suitable multiphase model needs to be selected. The two suitable models in Star-CCM+ are: the Volume of Fluid (VOF) model and the Multiphase Segregated Flow (MSF) model.

The VOF model is a relatively simple and robust multiphase model, suited for simulating several immiscible fluid mixtures, free surfaces and phase contact time. The fluids involved are assumed to share the same velocity, pressure and temperature fields. The equations of motion are solved for one (single-phased) fluid, whose properties are calculated based on the volume fraction of the involved phases. The only extra equation that is needed besides the Navier-Stokes equations is the transport equation for the volume fraction [16]:

$$\frac{d}{dt}\int_V a_i\,dV + \int_S a_i \mathbf{v}\cdot da = \int_V \left(S_{a_i} - \frac{a_i}{\rho_i}\frac{D\rho_i}{Dt}\right) dV, \tag{2.35}$$

where a_i is the volume fraction of phase i, defined as $a_i = \frac{v_i}{v}$. S_{a_i} is a source or sink term, $\mathbf{v}$ is the velocity and V is the volume of the cell.

An important requirement for the VOF model is to make sure that the mesh is fine enough to represent the geometry of interest, as is shown in Fig. 2.19. For the current problem, it is desired to maintain a sharp interface between the oil and the air phases, and a sufficiently fine mesh is thus needed in the regions where the interaction is expected to occur. Once the grid size is determined, a suitable time step can be determined. It is advised to keep the CFL number below 0.5 for VOF simulations [16].

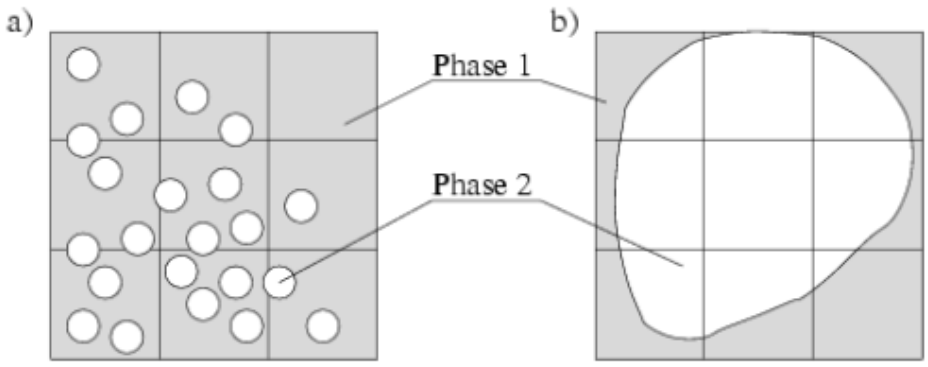

Figure 2.19: Mesh requirements for the VOF model [16].

The second suitable multiphase model is the MSF method, in general named Eulerian Multiphase Model (EMP), where both phases have their own set of equations of motion. Different multiphase interaction models are available to model the influence exerted by one phase to the other across the interfacial area. This model is known to be more accurate than the VOF method. The downside is the higher computation time because of the higher number of equations that are solved [16].

2.4.4. Wall Treatment

For heat transfer problems, it is important to have an accurate representation of the flow on the near-wall mesh. There are different wall-treatment models available in Star-CCM+, depending on the non-dimensional wall distance, y^+:

$$y^+ = \frac{u^* d}{\nu}, \tag{2.36}$$

with u^* the friction velocity, d the distance to the wall and ν the kinematic viscosity.

The three options for the wall treatment are:

- **The low y^+ wall treatment**
  This model resolves the viscous sublayer and needs no modelling. The transport equations are solved in all cells. For high Reynolds numbers, the boundary layer becomes very thin and results in a high number of required cells to meet the low y^+ condition. The y^+ value needs to below 1 for this wall treatment model. In order to accurately model the wall bounded flow or accurately solve heat transfer problems, this model should be used, as it is the most accurate treatment.

- **The high y^+ wall treatment**
  This model does not resolve the viscous sublayer, but uses wall functions to model the flow near the wall. The turbulent properties of the flow are derived from equilibrium boundary layer theory. The conditions for y^+ are that this value needs to be larger than 30. The main advantage of this model is the

significant savings on near-wall cells. However, this gain in computation time comes with a decrease in accuracy.

- **All y^+ wall treatment**
  This model is a combination of the two mentioned treatments models, where a varying y^+ value can be applied and the model automatically picks the correct wall treatment model. Both are combined by means of a blending function. This treatment can be considered as the least accurate of the three treatments.

2.4.5. Flow solver

There are two ways of solving the non-linear Navier-Stokes equations. This is either done with the coupled solver or the segregated solver. With the coupled solver, the conversation equations are solved in a coupled manner. This means that the equations are solved simultaneously as a vector of equations [16]. The velocity field is obtained from the momentum equations and from the continuity equation, the pressure is calculated. The downside of the coupled solver is the high memory requirements since all equations are solved at the same time. The convergence is however quite fast.

The segregated solver solves the integral conservation equations in a sequential manner. The solution variables, such as u, v, w and p are solved iteratively one after the other. This way the solver requires less memory, but is known to converge slower than the coupled solver. The solver is mostly applied to constant-density flows, although it can also handle mildly-compressible flows. It cannot be used for shock-capturing or high Mach number flows [16].

2.4.6. Spatial discretisation

The solver in Star-CCM+ is based on the finite volume method. All conservation equations can be written in the form of a transport equation:

$$\frac{d}{dt}\int_V \rho\phi dV + \oint_A \rho\phi V \cdot dA = \oint_A \Gamma\nabla\phi \cdot dA + \int_V S_\phi dV, \tag{2.37}$$

with ϕ the transport scalar property, A the surface area of the control volume, dA the surface vector, Γ the diffusion coefficient and S the source terms. It can be seen that Eq. (2.37) contains four terms. These are the transient term, the convective flux, the diffusive flux and the source term [16].

This partial differential equation is solved numerically to determine the solution for the scalar property, which can be $1, u, v, w$ or E. Since a finite volume method is used, the value of the scalar property is defined in the cell centres. To obtain the value of ϕ on the faces of the cells and to determine the gradients, an interpolation is needed. In general the convection calculations are advised to be done with the second-order scheme, unless there is a poor grid quality or other reasons [16]. The gradients are calculated with the Hybrid Gauss-Least Squares Method. For a detailed description of these models the reader is referred to the Star-CCM+ User Guide [16].

2.4.7. Temporal discretisation

Time is an additional coordinate when transient calculations are performed. The implicit unsteady solver in Star-CCM+ offers two options for the temporal discretisation: the first-order and second-order schemes. The first-order scheme, also called the Euler implicit scheme, approximates the transient term in Eq. (2.37) using the solution at the current time level, $n+1$, and the solution at the previous time level, n:

$$\frac{d}{dt}\left(\rho\phi V\right)_0 = \frac{\left(\rho\phi V\right)_0{}^{n+1} - \left(\rho\phi V\right)_0{}^{n}}{\Delta t}. \tag{2.38}$$

The second-order discretisation scheme uses the solution at the current time level and the solutions from the previous two time levels:

$$\frac{d}{dt}\left(\rho\phi V\right)_0 = \frac{\{(a^2-1)[\left(\rho\phi V\right)_0{}^{n+1} - \left(\rho\phi V\right)_0{}^{n}] + [\left(\rho\phi V\right)_0{}^{n-1} - \left(\rho\phi V\right)_0{}^{n}]\}}{a(a-1)\Delta t^{n+1}}, \tag{2.39}$$

with

$$a = 1 + \frac{\Delta t^{n+1}}{\Delta t^{n}}, \tag{2.40}$$

$$\Delta t^{n+1} = t^{n+1} - t^{n}, \tag{2.41}$$

$$\Delta t^{n} = t^{n} - t^{n-1}. \tag{2.42}$$

The first time step calculation with the second-order discretisation is done by using the first-order discretisation, since only two time levels are available at the start.

3

The liquid jet

This chapter presents the research performed on the isolated oil jet. It was shown in Fig. 2.10 that for short jets ($L/d < 30$) the level of interaction with the surrounding air is relatively low, resulting in a small effect on the heat transfer (10%). The jets involved in this project are much longer and can be considered as long jets (L/d = 60 – 115), for which the effect on the heat transfer is expected to be much larger. The goal in this analysis is therefore to determine the varying jet properties when it reaches the piston. By isolating the oil jet from the piston cooling problem, the research can be focused on correctly simulating the complex interactions between the oil and the air rather than on the impingement or heat transfer.

The structure of the chapter is as follows. First the problem description is discussed in Section 3.1, followed by the presentation of the two validation cases that are used to develop the CFD model, in Section 3.2. The investigation conducted with RANS is discussed in Section 3.3 and these results are presented in Section 3.4. The CFD model used for LES is presented in Section 3.5, followed by the LES results in Section 3.6. After the validation of the CFD model, a trend analysis is performed, by varying relevant input parameters and determining the effect on the jet behaviour. This is discussed in Section 3.7. Finally, the main conclusions are summarised in Section 3.8.

3.1. Problem description

The analysis of the isolated oil jet is the first part of this research project. The goal of this analysis is to accurately simulate the DAF oil jet and to make accurate predictions of the condition just before impacting the piston. The output of this analysis is used in later stages of this project to determine the effect of on the cooling process.

Before investigating these effects, the flow properties of interest need to be determined. The cooling technique investigated in Chapter 5 is the spray cooling technique and it was shown in Chapter 2 that the Nusselt number is depending on the Reynolds number and the Prandtl of the jet. However, these two numbers are determined with the jet properties at the nozzle exit. When the jet properties at impact are significantly different, the properties at the nozzle cannot be used and the local properties thus need to be determined. The parameters of interest are thus the flow properties that are needed to determine the Reynolds number and Prandtl number: $\rho, \nu, \mu, Cp, \sigma$ and the local jet diameter d_{local}.

The other cooling method discussed in Chapter 2 is the gallery cooling technique, which is also the cooling technique used by DAF in their engines. This technique is not investigated in this thesis, nevertheless a very important parameter for this cooling technique is produced as an output: the flow rate efficiency. This efficiency can be used to determine the flow rate (or mass flow) that enters through the cooling gallery inlet orifice.

The methodology is to isolate the oil jet from the piston cooling environment, such that the focus can be on accurately modelling the complex interactions with the surrounding air. Several simplifications and assumptions are thus needed. The most important one is that the surrounding air is assumed to be still, whereas in reality this region is dominated by turbulent waves created by the reciprocating motion of the piston. Next, the effect of the nozzle on the jet behaviour is neglected. Since the DAF oil jets disintegrate according to the second-wind induced and/or the atomization breakup regime (as discussed in Chapter 2), the dominant contributor to the disintegration is the aerodynamic effect. This assumption is related to near-wall mesh requirements and computation time, as will be explained in more detail in Section 3.5.

The CFD model is developed by reproducing two test cases. Once the CFD model is able to reproduce these cases within acceptable accuracy, the model is used to analyse the DAF piston cooling jets. Since a moving piston is involved in the problem, the flow properties are determined at different piston locations. Both the RANS and the LES methods are used to reproduce the test cases. The analysis of the DAF jets is done by varying relevant input parameters and investigating the effect on the jet behaviour.

3.2. Validation material

There is a limited availability of studies in literature on the determination of characteristics of free-surface liquid jets. Especially for the jets in the breakup regimes in which the DAF jets are operating, there is little known about the breakup mechanism. The selected test cases are therefore the two cases discussed in Chapter 2: the flow rate efficiency experiment by DAF [30] and the LES study on oil jet spreading by Moghe and Janowiak [6]. The relevance of these cases is shortly discussed next.

3.2.1. Flow rate efficiency experiment (DAF)

The first test case is the experiment performed by DAF to determine the flow rate efficiency of the piston cooling jets. The experiment is performed with the nozzle used in the MX-13 engine, which is also the reference nozzle considered in this project. The experimental setup and results of the experiment are shown before in Fig. 2.5 and Fig. 2.6. The main conclusion that can be drawn from this experiment is that the flow rate efficiency decreases with increasing flow rate. This can be explained by the increasing turbulence levels in the jet. The jets show a more intense interaction when the flow rate is increased, resulting in more ligament and droplet formation. This results in more oil not entering the gallery orifice, and thus affecting the flow rate efficiency. The parameter of interest is therefore the flow rate efficiency at the TDC location of the piston, and will be used for the validation.

3.2.2. Moghe and Janowiak (Case B)

The second test case is a LES study on the spreading of an oil jet. The similarity of this test case with the current project was already shown in Chapter 2, by comparing the similarity parameters in Table 2.4. The results of this study are shown in Fig. 2.4. The main conclusion that can be drawn from this study is similar to the conclusion for the previous test case: the spreading increases with increasing flow rate/turbulence. Fig. 2.4 shows that the level of interaction increases, which results in a larger spreading. The downside of this test case is that the instantaneous spreading is measured instead of a sampled spreading. This is done because they compared their LES results to experimental results, which is also an instantaneous measurement (photograph). The parameter of interest in this test case reproduction is thus the instantaneous spreading of the oil jet at a target distance of 283 mm.

3.3. RANS

In this section, the CFD model developed in Star-CCM+ for the RANS investigation is discussed. It was addressed in Chapter 2 that the DAF oil jets breakup according to the second wind-induced and atomization breakup regimes. The disintegration of these jets are initiated by the short wavelength disturbances on the

liquid surface. Since the RANS method is only solving for mean flow properties, it is not expected that these large scale eddies on the liquid surface can be modelled. However, since RANS is the only suitable way to deal with turbulence in later stages of this project, it is important to investigate the accuracy of the RANS results when the jet is modelled.

3.3.1. Computational domain

The free jet problem can be considered as an axisymmetric one. Since RANS is used and only mean flow properties are simulated, this axisymmetric property can be used to reduce the problem to a 2D-axisymmetric one. The 2D-axisymmetric domain can be seen in Fig. 3.1. In an axisymmetric simulation, the 2D domain is swept trough an angle of 1 radian around the axisymmetric axis. The dash-dotted line in the figure represents this axis. The dashed vertical lines represent the minimum and maximum target distances considered in this study: the distance between the nozzle and the BDC and TDC locations of the piston.

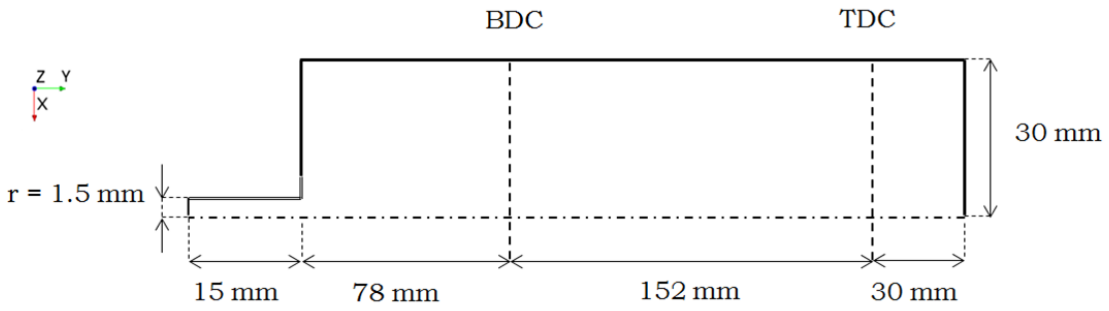

Figure 3.1: RANS computational domain with dimensions. The dashed vertical lines represents the BDC and TDC locations of the piston.

The dimensions presented in Fig. 3.1 are determined by performing a boundary sensitivity analysis. The size of the domain is varied by keeping the mesh the same, such that really only the boundary effect is monitored. The monitored flow property is the turbulent kinetic energy, which is a function of the velocity fluctuations and thus a measure of the turbulence. The reason for selecting this flow property, and not more relevant properties such as the volume fraction profile or spreading, is related to the limitations of the RANS method, as will be shown later in Section 3.4.1.

First, a region of interest needs to be defined in both directions of the domain. In y-direction this is set at the TDC location of the piston, since this is closest to the boundary. In x-direction, the maximum expected spreading distance can be used. Since the determination of this spreading is part of the research and a priori unknown, the results of [6] can be used. Case B of their study was shown in Chapter 2 to be most similar to the DAF jets, and the resulting spreading (at a target distance of 283 mm) for this jet was 25 mm, obtained with a 3.5 mm nozzle diameter. Both the diameter and the maximum target distance considered for the DAF jets are smaller than these numbers and therefore the spreading will most likely be smaller than 25 mm. Assuming a region of interest of 25 mm can thus be considered as a safe assumption.

The sensitivity analysis is performed by first varying the dimension in x-direction. The first tested height is the dimension used by [6], which is equal to 17d. The other two tested dimensions are 20d and 23d. The results for the TKE can be seen in Fig. 3.2 (left). It appears from this figure that the boundary effect is very small, as there are no serious differences observed. The relative difference between the results is plotted in Fig. 3.2 (right). Increasing the height of the domain from 17d to 20d results in a relative difference smaller than 6% in the defined region of interest. For the second domain increase, this relative difference decreases to below 2.5%. An error smaller than 2.5% is accepted and the final width of the domain is set at 20d. For a 3 mm jet, this dimension is then equal to 60mm (30 mm for the axisymmetric domain).

The next step is to determine the length of the domain (in y-direction), by performing a similar analysis. Again the starting point is the domain length used by [6]. The tested extension lengths of the domain (with respect to the maximum target distance of 230 mm) are 20, 30 and 40 mm. The results are presented in Fig. 3.3. The

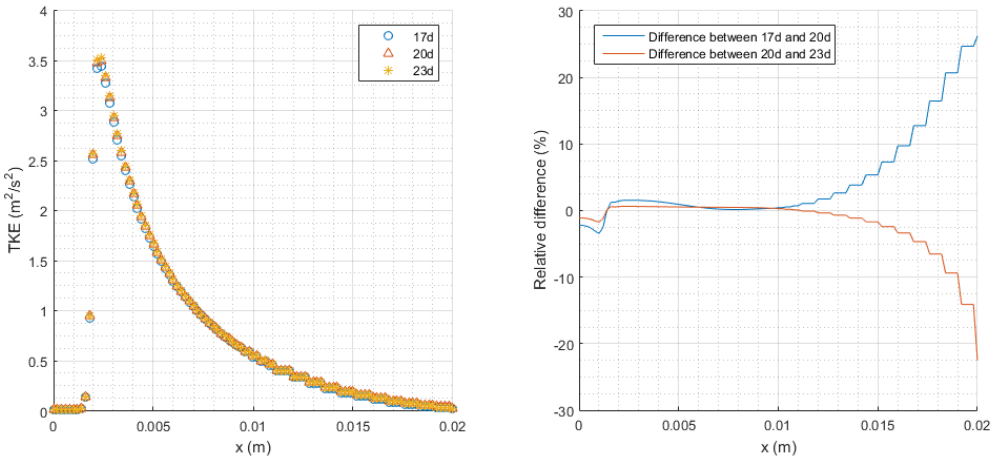

Figure 3.2: (Left) results for the TKE obtained for different domain widths. (Right) relative difference between the tests.

relative error shows that increasing the extension of the domain from 20 mm to 30 mm, results in differences that are larger than 5%. Increasing the extension from 30 mm to 40 mm results in a relative error which smaller than 1% in the region of interest. Therefore the final length of the domain is set equal to the target distance of interest (230 mm) plus an extra 30 mm to eliminate the boundary effect.

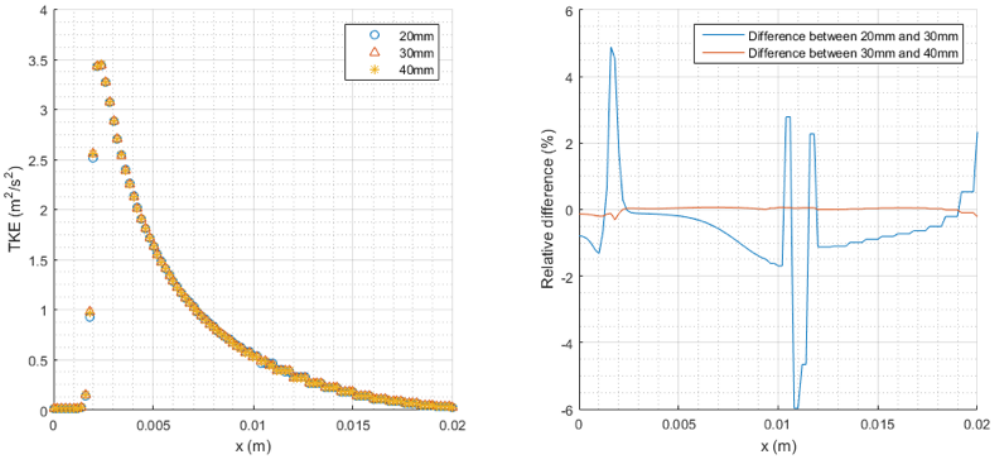

Figure 3.3: (Left) results for the TKE obtained for different domain lengths. (Right) relative difference between the tests.

The only length that still needs to be determined is the nozzle length, which is determined at 5d. This is the minimum length needed in LES, such that the turbulence specified at the inlet can develop into natural turbulence when entering the domain. This is explained in more detail in Section 3.5.

3.3.2. Boundary conditions

The boundary conditions of the computational domain presented before are discussed next. Four boundary conditions are used to represent all the boundaries of the domain: the inlet, the outlet, the nozzle and the axisymmetric axis. These boundaries are shown in Fig. 3.4.

Inlet

The inlet is represented by a *velocity inlet* boundary condition. For this boundary condition, the user needs to define a mean velocity profile and to specify the turbulence. The velocity profile used for the inlet is a fully

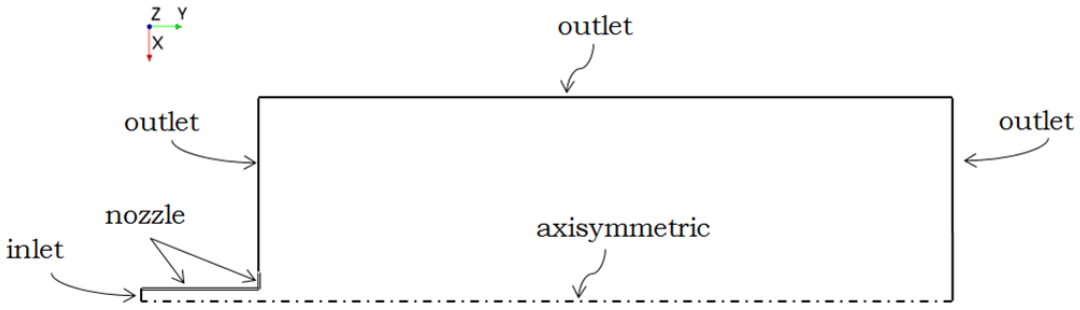

Figure 3.4: Boundary conditions applied to the RANS 2D-axisymmetric domain.

developed turbulent velocity profile obtained from a separate precursor simulation, explained in Appendix C. The turbulence is specified with the turbulence intensity (I = 0.05) and a turbulent length scale (σ = 0.07d), obtained from respectively [6] and [16] for fully developed turbulent pipe flow.

Outlet

The outlet boundaries are represented by a *pressure outlet* boundary condition. The reference pressure is set at the atmospheric pressure (101325 Pa). The back flow specification is such that only air can flow back into the domain.

Nozzle

For the nozzle, the *no-slip wall* boundary conditions is applied with the default settings for surface roughness (smooth).

Axisymmetric axis

This boundary is represented by the *axis* boundary condition.

3.3.3. Mesh

The mesh is one of the dominant factors in both the accuracy of the final results and the computation time. With decreasing mesh sizes, the discretisation error introduced by the mesh decreases, while the computation time increases. Therefore it is opted for to only locally refine the mesh in those parts of the domain where the oil-air interaction is expected to take place. This refinement strategy is similar to the strategy used by [6]. Two examples of the mesh are shown in Fig. 3.5. It can be seen that both the polyhedral and the structured mesh types are tested. The effect of the mesh type on the results is discussed in Section 3.4.1.

The mesh size is determined by the conditions used by [6]. They have used a mesh size in the refinement zone, such that the jet diameter is covered by 12 cells. For a 3 mm nozzle, the mesh size in the refined zones of the mesh is then equal to 0.25 mm. The mesh size in the coarse parts of the mesh is equal to 4 times this mesh size: 1mm. The total number of cells of the structured and polyhedral grids is respectively 54,000 and 67,000 cells.

3.3.4. Physics models

Next, the physics models and CFD settings used for the RANS analysis are presented. The detailed explanation of these models is already given in Section 2.4

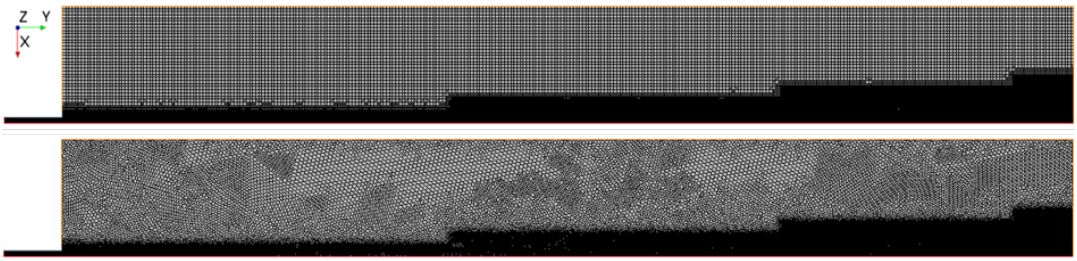

Figure 3.5: Examples of the mesh used for the RANS analysis: (upper) structured grid and (lower) polyhedral grid.

Spatial discretisation

It was observed that the VOF convection scheme is one of the dominant parameters in the outcome of the results (only in combination with a polyhedral grid). Both the first-order and second-order VOF convection schemes are tested. It is advised by [16] to use the second-order scheme, unless a less accurate or more robust discretisation is needed. This will be shown in the results of the RANS simulations in Section 3.4.1. All other convection calculations are done by using second-order schemes.

Temporal discretisation

The unsteady simulations are performed with the first-order discretisation schemes.

Gravity

The gravity model is activated, acting in the negative y-direction.

Turbulence model

As was discussed in Chapter 2, free jets are often modelled with the $k-\epsilon$ model. Therefore this turbulence model is selected, and the effect of other turbulence models is not investigated.

Multiphase model

VOF is used for all multiphase interaction modelling in this chapter. The EMP/MSF model is also investigated because of its higher accuracy. However, the main findings were that the EMP model is extremely unstable and even for this relatively simple RANS problem all simulations systematically diverged. Possible reasons for this outcome are not searched for, as it is not within the scope of this thesis.

3.4. Results and validation (RANS)

The RANS model described before is now used to reproduce the the test cases discussed in Section 3.2. The results of these reproductions are presented next.

3.4.1. Flow rate efficiency experiment (DAF)

The experiment is conducted for flow rates between 3 and 7 L/min. In this section, only the reproduction results for the 7 L/min oil jet are presented. Other tested flow rates resulted in a similar outcome, and therefore not included.

It was mentioned in Section 3.2 that the 7 L/min jet is very similar, in terms of Reynolds number and Ohnesorge number, to the jet (Case B) considered by Moghe and Janowiak in their LES study. Based on their LES

results one can thus expect a certain outcome for the RANS results. Since mean flow properties are solved for, the expected shape should look like the shape shown in Fig. 3.6. The first part of the jet should remain reasonably straight without any spreading behaviour and without the unsteady surface instabilities (because of RANS). The oil volume fraction in this part should be equal to 1 (oil only). When the jet starts to spread, this should result in a decrease of the oil volume fraction, since the cells are now (in time) filled with both oil and air.

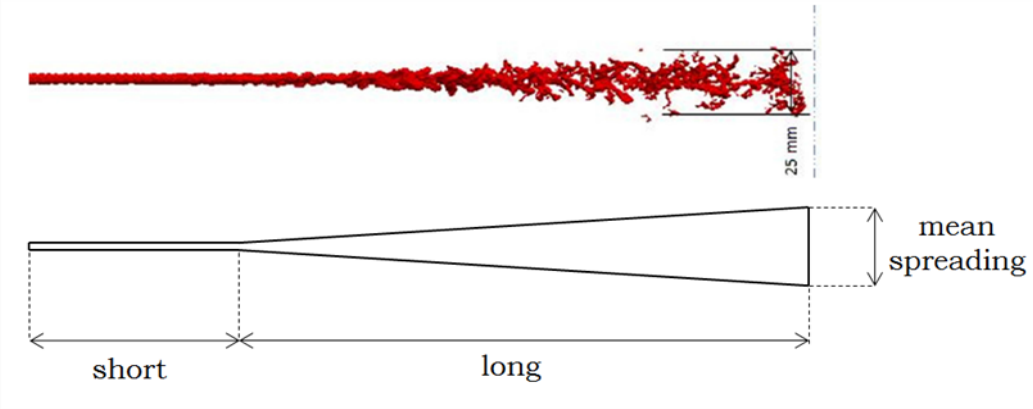

Figure 3.6: Expected RANS results for the oil volume fraction based on results of Moghe and Janowiak, with α between 0.1 and 1.

The results obtained on a structured grid and with the second-order VOF convection scheme are presented in Fig. 3.7. These results show the oil volume fraction, the velocity (magnitude) and the turbulent kinetic energy in the domain.

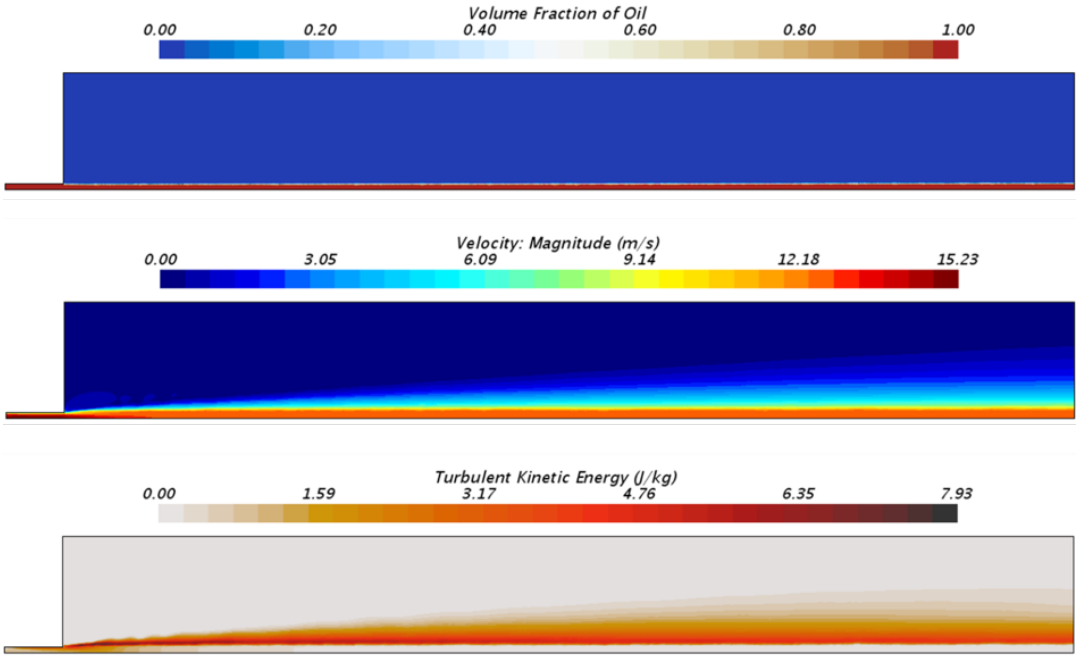

Figure 3.7: Results obtained on a structured grid and second-order VOF convection scheme.

The first thing that can be observed from these results is that the spreading and interaction is clearly not modelled. The volume fraction result show a completely straight jet. The shape of the jet can also be observed in the results for the velocity and TKE, where the velocity is constant and the TKE is zero. There is no point of comparing these results to the test case results, since the flow rate efficiency is clearly equal to 100%.

It can be noticed that in the air phase, just above the oil-air interface, there is a layer of air with a certain velocity and TKE. This layer is growing in thickness as the jet length increases. The TKE should normally

indicate turbulent fluctuations or in this case interaction between the phases. However, since the oil phase is clearly unaffected by these layers, this cannot be considered as interaction. The conclusion from these results is that the results are not physical and the RANS-VOF combination is not capable of producing accurate results for the jet behaviour. A possible reason for this outcome could be the mesh type, since the oil-air interface is not perfectly aligned with the mesh. Therefore, the same simulation is repeated on the polyhedral mesh (again with the second-order VOF convection scheme), for which the results are shown in Fig. 3.8.

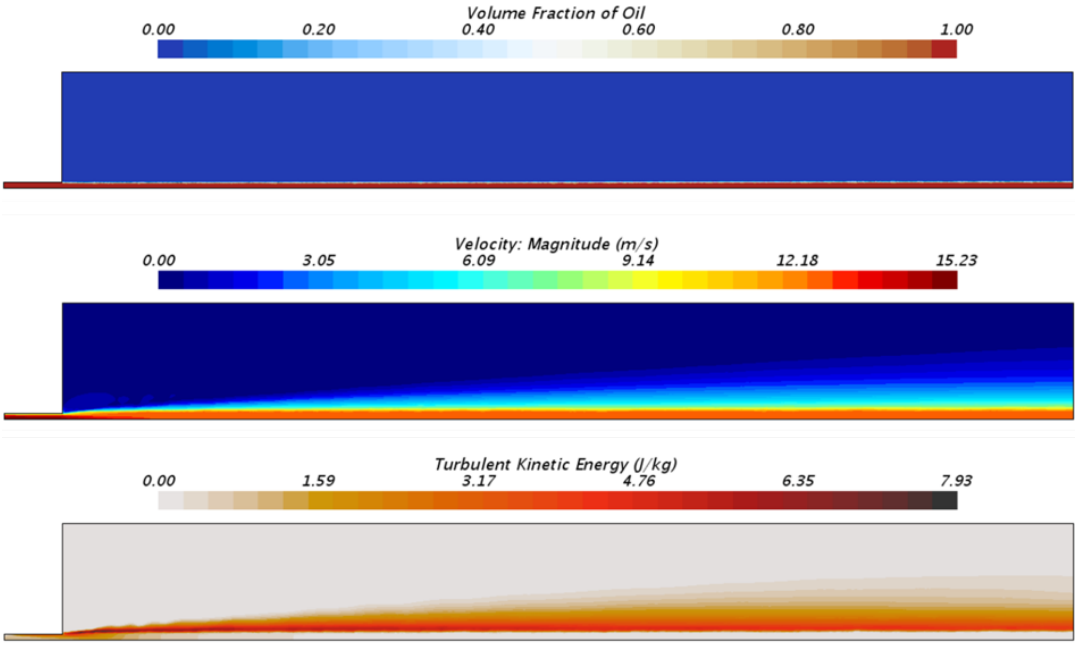

Figure 3.8: Results obtained on a polyhedral grid and second-order VOF convection scheme.

The outcome is the same: there are layers that indicate interaction between the phases in the velocity and TKE plots, however these have no effect on the oil volume fraction. It can be seen that the interface is again sharp and straight, although the mesh is not aligned with the flow now. Because of the second-order VOF convection scheme, the VOF model forces the interface to be sharp. The next test is therefore to switch to a lower order VOF convection scheme. First these results on the structured mesh are shown, in Fig. 3.9. It can be seen that the outcome is again very similar. Even though the VOF model is not forcing the interface to be sharp, the alignment with the structured mesh results in a sharp interface.

Finally, the first-order VOF convection scheme is used on the polyhedral mesh. These results are shown in Fig. 3.10. It can be seen that the results are totally different now, and there is a clear effect when the order is decreased on polyhedral grids. The jet starts to spread out straight from the nozzle exit and it can be observed that the volume fraction quickly decreases as the jet length increases. These results are much more similar to the expected outcome shown in Fig. 3.6.

In order to investigate if these results show a physical phenomenon (spreading) or if it is simply the introduction of numerical diffusion by the lower order VOF convection scheme, a mesh sensitivity analysis is performed. The mesh size is decreased and the effect of this on the volume fraction is monitored. The results of this study are shown in Fig. 3.11. The dashed line represents the volume fraction obtained with the second-order convection scheme, and remains equal to 1 for the entire jet length.

It can be seen that there is a clear trend visible: the volume fraction approaches the value of 1 as the mesh size is decreased. In the limiting case of decreasing the mesh size, it is expected that both schemes will produce the same results, and therefore it can be concluded that the observed phenomenon in Fig. 3.10 is caused by the introduction of numerical diffusion. If the numerical diffusion did not play a role, the results would not be realistic either, as the spreading starts straight from the nozzle exit (spray-like behaviour), which is not the case in reality.

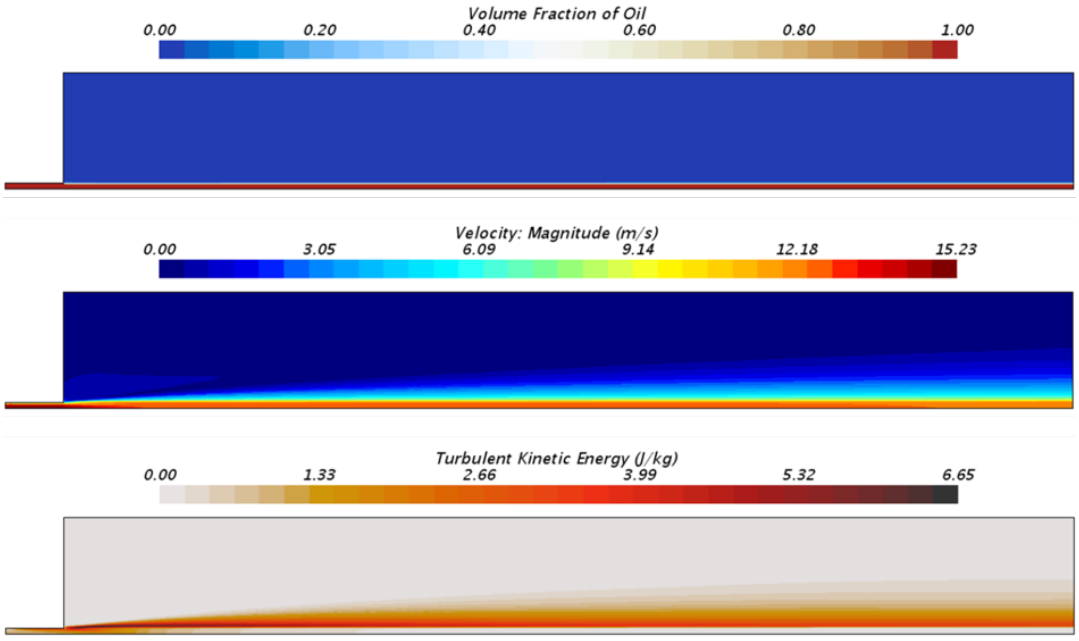

Figure 3.9: Results obtained on a structured grid and first-order VOF convection scheme.

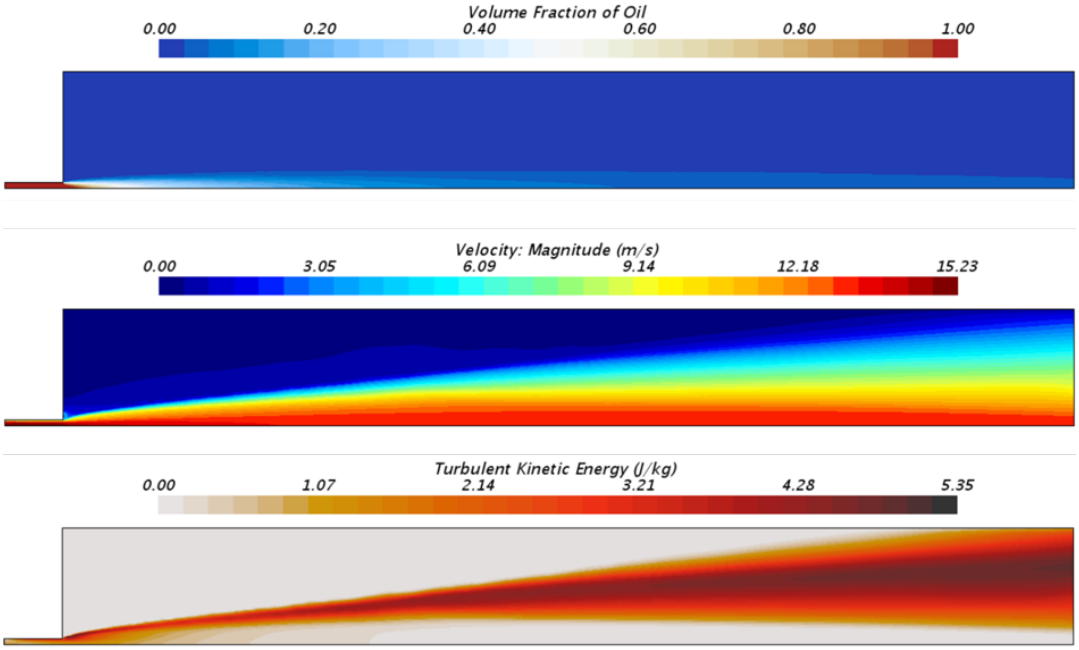

Figure 3.10: Results obtained on a polyhedral grid and first-order VOF convection scheme.

The final test is performed by running a transient simulation, resulting in exactly the same results, as can be seen in Fig. 3.12.

The main conclusion that can be drawn from these results is that the RANS-VOF combination is not able to correctly model the jet behaviour. The reason is believed to be the counteracting models that are used, as the VOF model is trying to maintain a sharp interface between the phases and the RANS model is trying to represent a time-averaged solution of the jet, which is one where the volume fraction should gradually decrease, and thus not with a sharp interface. As was mentioned before, the disintegration and breakup of the DAF jets (based on the mechanism of breakup) is initiated by the unsteady surface instabilities that form

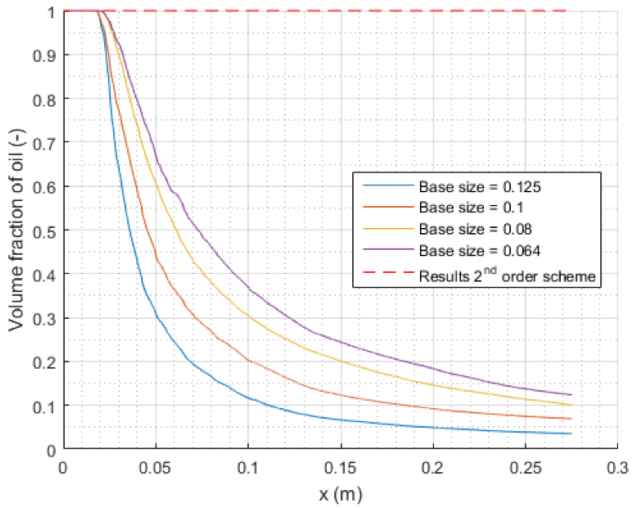

Figure 3.11: Effect of the mesh size on the volume fraction at the jet axis, for the polyhedral grid and first-order VOF convection scheme.

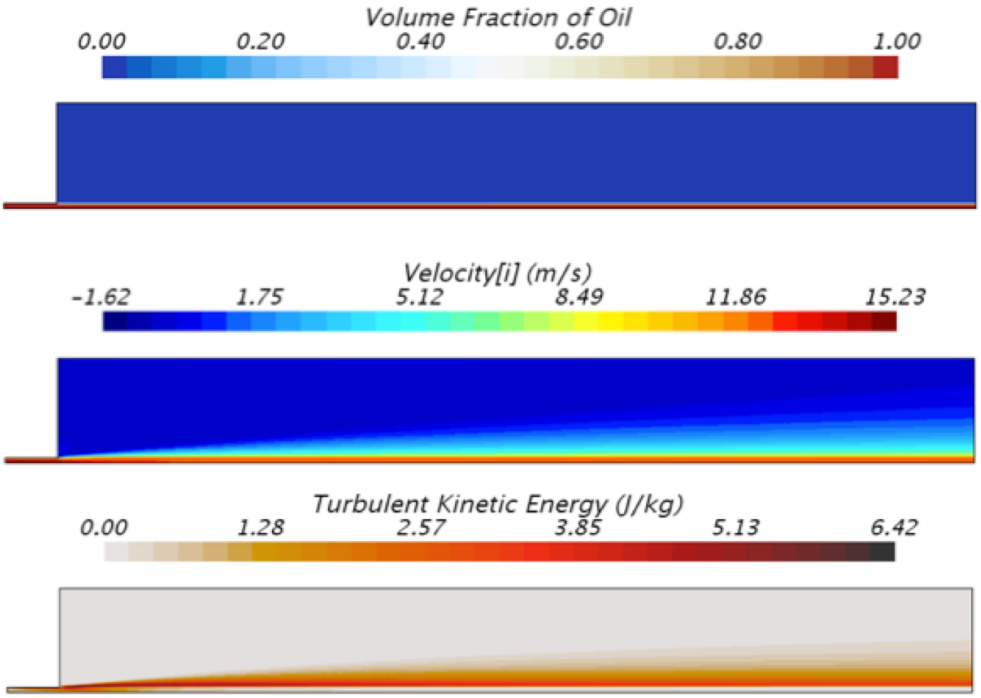

Figure 3.12: Results obtained for a transient run, on a structured grid and second-order VOF convection scheme.

close to the nozzle exit, and these cannot be modelled when both with the RANS-VOF combination.

3.4.2. Moghe and Janowiak (Case B)

This test case is not reproduced since the RANS-VOF combination is not able to produce physical results for the oil jet behaviour.

3.5. LES

This section presents the LES model developed in Star-CCM+ to analyse the isolated oil jets. The model is developed by reproducing the two test cases discussed in Section 3.2. The results of this reproduction and the comparison of these results to the test case results are presented in Section 3.6.

3.5.1. Computational domain

As turbulence is a three-dimensional phenomenon, the computational domain needs to be in 3D as well, which is one of the reasons for the high computation time related to LES. The 2D schematic of the cylindrical 3D domain is shown in Fig. 3.13.

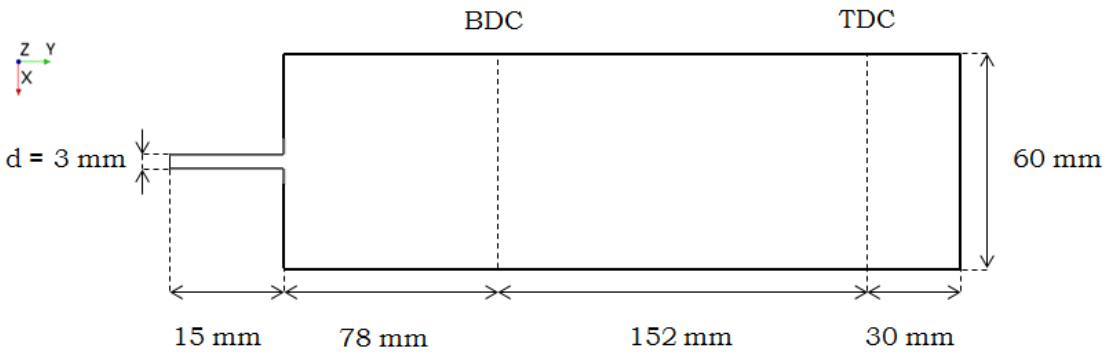

Figure 3.13: Dimensions of the computational domain for the LES simulations, with the dashed line as the indication of the BDC and TDC locations of the piston.

Because of the high computation time related to LES, a domain sensitivity analysis by using LES is not performed. The dimensions determined earlier for the RANS domain are therefore used for the LES computational domain as well.

3.5.2. Boundary conditions

Three boundary conditions are used to represent all the boundaries of the domain: the inlet, the nozzle and the outlet. These boundaries are shown in Fig. 3.14.

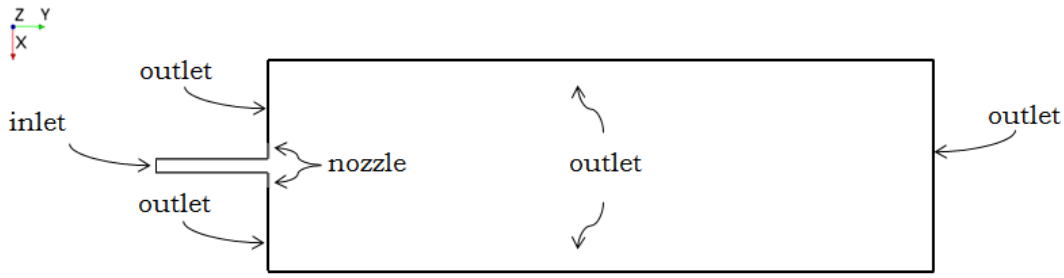

Figure 3.14: Boundary conditions of the 3D LES domain.

Inlet

The inlet of the domain is represented by a *velocity inlet* boundary condition. In order to study turbulence effects with LES, a requirement for the inflow condition is that this needs to be turbulent. Without doing this, the spatial development of the flow will not be realistic and possibly not even turbulent. To trigger the turbulent characteristics of the flow, there are several ways of generating realistic (turbulent) inflow conditions [44].

The first method is to obtain inflow data from a separate precursor simulation for the flow in the nozzle only. The downside of this method is that it is computationally expensive because of large data that needs to handled and an a priori unknown run time. A second and more efficient method is the recycling method, which has proven to be successful [44]. The most efficient method is by creating artificial turbulence at the inlet. This can be done by using the Synthetic Eddy Method (SEM), which is available in Star-CCM+. The goal with SEM is to generate turbulence which resembles the actual flow by matching a reduced set of statistics. This method is used to create realistic inflow and a short explanation of the method is given next. For more details about this method, the reader is referred to relevant literature [16][44].

The SEM method requires three inputs: the mean velocity (v), the turbulence intensity (I) and a turbulent length scale (σ). The length scale is used to create an imaginary box in which the turbulence is convected and recycled [44]. An example of this box is shown in Fig. 3.15. Since the velocity profile is only provided for the normal direction, only fluctuations in this directions will be created. The mean velocity profile that is applied to the inlet is a fully developed turbulent velocity profile, as was done for the RANS inlet boundary condition. This profile is obtained from a separate precursor simulation for the nozzle, explained in more detail in Appendix C. The values for the turbulence intensity (I = 0.05) and the turbulent length scale (σ = 0.07d) are obtained from respectively [6] and [16] (for fully developed turbulent pipe flow).

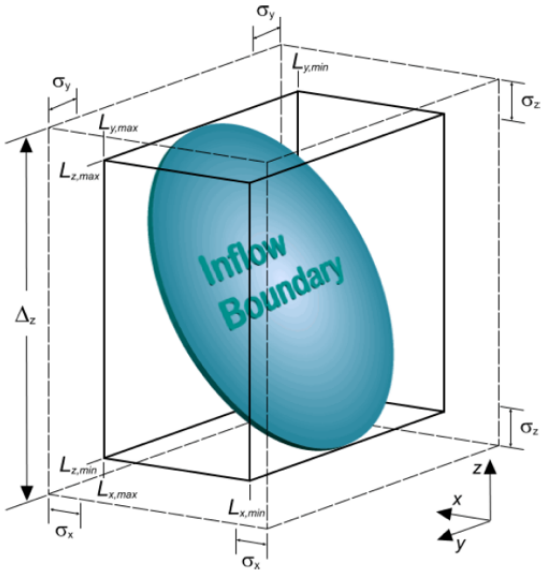

Figure 3.15: Imaginary box created with SEM, to produce artificial turbulence at the inlet[16].

Finally, there is one requirement left for the SEM to perform properly. The created turbulence at the inlet resembles turbulence, however it is still artificial turbulence. A certain distance is required between the inlet and the domain of interest, such that this artificial turbulence can develop into natural turbulence. The length needed for this development to occur is given in [16] to be 5 times the diameter of the pipe. The nozzle length is therefore determined at 5d.

Nozzle

The boundary condition applied to the boundaries that represent the nozzle is the *no-slip wall* boundary condition, with the default value for the surface roughness (smooth).

Outlet

The *pressure outlet* boundary condition is assigned to all remaining boundaries. The reference pressure is set at the atmospheric pressure (101325 Pa) and the backflow specification is such that only air can flow back into the domain.

3.5.3. Mesh

Results obtained with LES are very sensitive to the grid resolution. Varying the grid size not only influences the discretisation error but also the modelling of the subgrid scales. It is mentioned by [45] that grid independence cannot really exist in LES, as grid-independent LES is actually a DNS. The computation benefits of LES compared to DNS are lost when the LES is approaching a DNS. Nevertheless, the effect of the mesh size is investigated. Only structured grids are considered in this investigation, because of their low requirement of computational memory and cost [16], compared to polyhedral grids. The refinement of the mesh is done in the same way as was done for the RANS mesh, by only refining in the regions where the jet interaction between the phases is expected to occur. This refinement strategy is similar to the strategy used by [6] in their LES study. An example of the mesh refinement is shown in Fig. 3.16.

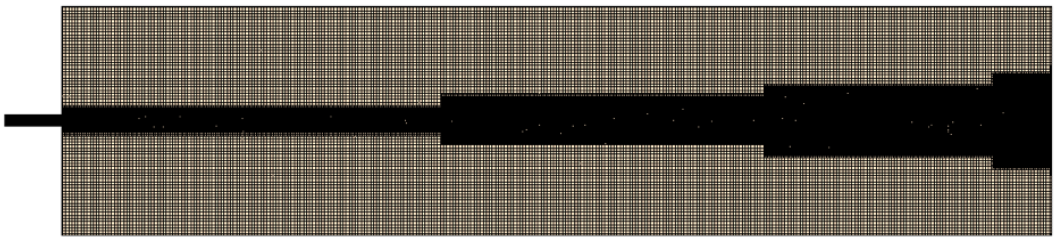

Figure 3.16: Example of the mesh and mesh refinement used for the LES simulations.

The mesh size in the region of interest is determined by testing three different (feasible) mesh sizes. The LES quality metric, discussed in Section 2.4, is checked for these grids, which needs to be above 0.8 in the region of interest. The first mesh size is based on the condition set by [6] in their LES study. They selected a mesh size such that the jet diameter is covered by 12 cells in the nozzle, and applied this mesh size throughout the entire refined mesh region. With a reference diameter of 3 mm for the DAF jets, the first mesh size is then equal to 0.25 mm. The mesh size in the coarse parts of the mesh is chosen to be 4 times the mesh size in the refined zones. The resulting total cell count with these mesh settings is equal to 3.2 million cells. The other two tested mesh sizes (in the refinement zone) are 0.2 mm and 0.3125 mm, resulting in a total cell count of respectively 6.1 million and 1.7 million cells. The results for the LES quality metric are shown in Fig. 3.17.

It can be seen that for all three mesh sizes the LES quality metric in the region of interest remains above 0.8 and thus all tested mesh sizes meet this requirement. Regions in which the LES quality metric is smaller than 0.8 can be observed near the nozzle, which are growing in size with increasing mesh size. Based on these results, it is difficult to determine a suitable mesh size, since all three of the tested mesh sizes are sufficiently small based on the criteria. A second output parameter is used to determine the suitable mesh size: the flow rate efficiency. The jet that is simulated corresponds to the 5 L/min jet of the flow rate efficiency experiment. The results for the flow rate efficiency obtained from the experiment is around 91%. The CFD results for the flow rate efficiency for the tested mesh sizes is 97%, 93% and 90%, for respectively a mesh size of 0.3125 mm, 0.25 mm and 0.2 mm. Based on these results, the final mesh size is determined at 0.2 mm in the refinement zones, resulting in a total cell count of 6.1 M cells.

From the results for the flow rate efficiency, it appears that there is still a mesh effect present when the 0.2

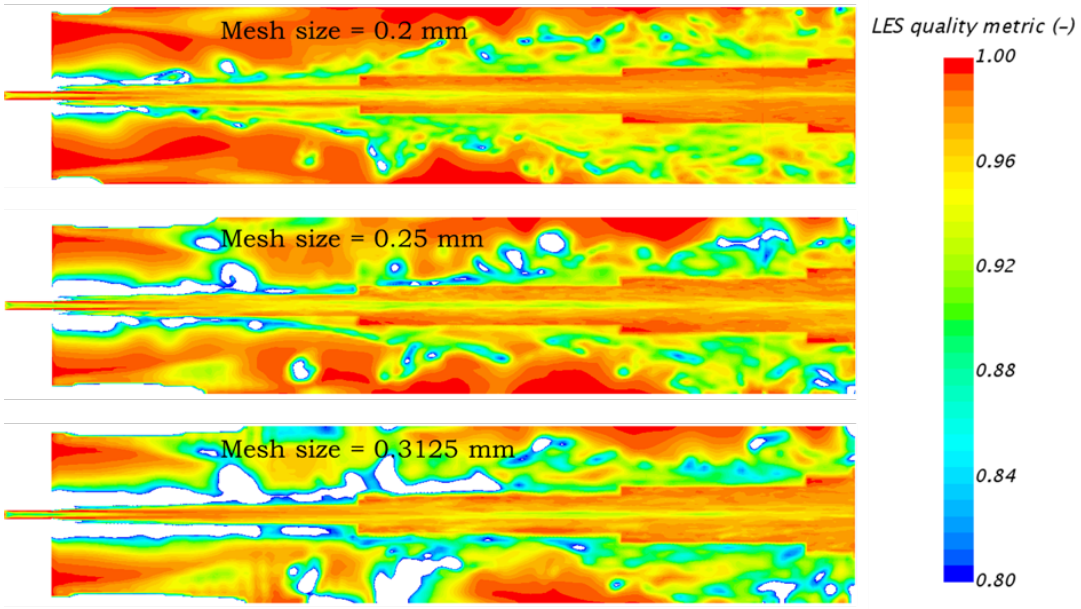

Figure 3.17: Results for the LES quality metric for the different tested mesh sizes.

mm mesh size is used. A possible further decrease of the mesh size by another factor 1.25 will result in a mesh size of 0.16 mm and a total cell count on 12 million cells. In combination with the smaller time step needed to meet the CFL condition, the estimated computation time will be equal be larger than 150 hours, which is considered to be computationally too expensive.

Finally, there is the mesh in the nozzle. Wall-bounded turbulent flows are complex and inhomogeneous, with the eddy size decreasing as the wall is approached [39]. In order to resolve these eddies, a very fine mesh is needed [46], with the result that the computation time increases (as a power of the Reynolds number[39]). Further, it was mentioned in Chapter 2, that the DAF oil jet is in between the second wind-induced and atomization breakup regimes. For these jets, the main contributor to the disintegration and the aerodynamics interaction with the surrounding air. Therefore, no special care is given to the mesh in the nozzle and this simplification is justified with the two mentioned reasons.

3.5.4. Time step

After the determination of the mesh size, the next step is to determine a suitable time step. It was already obtained from literature that for LES studies the CFL number in the region of interest needs to around 1, whereas for the VOF multiphase model this number needs to be below 0.5. The determination of the CFL number with a fixed mesh size can thus be achieved by changing the time step. With a lower time step, the run time of a simulation will increase and therefore this number should be determined with care.

However, it was found that when the CFL number is kept below 0.5 a serious mass imbalance was introduced. By reducing the time step even further, and thus the CFL number, the mass imbalance was eliminated. The final CFL number that solved this mass imbalance was found to be significantly lower than 0.5. Also it was observed that this CFL number was depending on the Reynolds number of the considered jet, as it needed to be decreased further for higher Reynolds number jets to eliminate the mass imbalance. The values used for the CFL number are discussed in Section 3.6, when the results are presented and discussed.

3.5.5. Initialisation and sampling

A large eddy simulation consists of two stages: the initialisation phase and the sampling phase. The initialisation phase is needed to get rid of the effect of the initial conditions. Once these effects are lost, one can

start the sampling. The sampling is done until the parameters of interest are converged to a certain averaged value and further sampling does not change this averaged value. The typical duration of these stages were mentioned in Chapter 2 to be around 2-5 flow cycles for each stage.

In order to decrease the computation time, both stages are kept as short as possible by tracking the behaviour of the parameter of interest. The selected parameter is the area-averaged mass flow through the inlet orifice at the TDC location of the piston. An example of the typical initialisation and sampling stages for the reproduction of test case 1 is shown in Fig. 3.18. In this figure, the area-averaged mass flow at the target plane is plotted versus the physical time. It can be seen that the mass flow is zero, until the flow reaches the considered plane. Then there is a large mass imbalance, related to the high CFL number, as explained before. A decrease of the CFL number then results in a decrease of the mass flow. When it is observed that this area-averaged mass flow starts to vary around a certain (expected) value, the sampling can start.

It can be seen that in this case the initialisation stage takes up to 0.075 seconds, which corresponds to 4.5 flow cycles. The sampling starts at 0.075 and takes about 0.045 seconds until a converged solution is reached. This corresponds to 2.8 flow cycles. The sampling time is considered to be sufficient, as longer sampling is will not change the sampled mass flow. The same initialisation and sampling methodology is applied to all other LES simulations in this chapter.

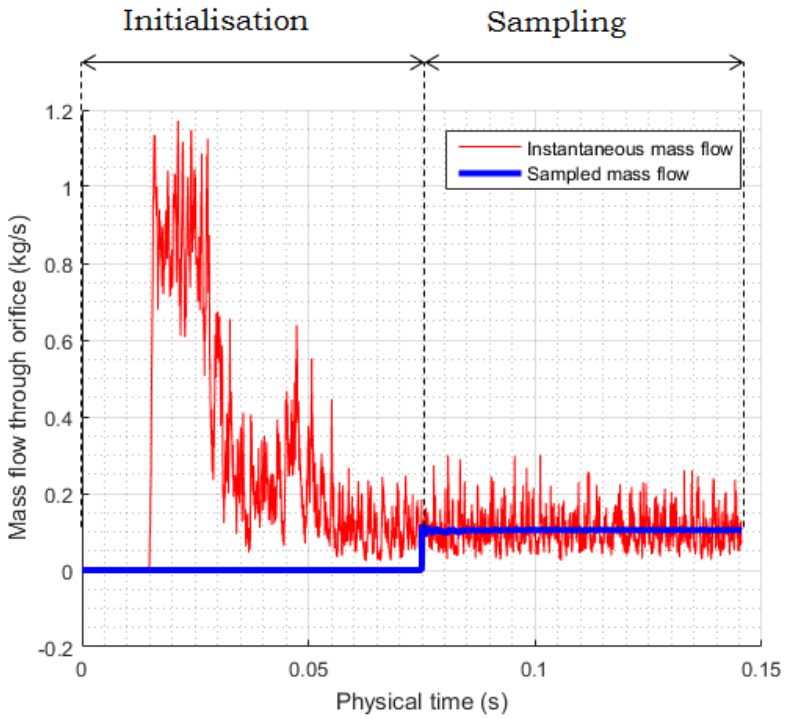

Figure 3.18: Typical initialisation and sampling monitor, obtained from the reproduction simulation of test case 1 (7 L/min case).

3.5.6. Physics models

Next, the physics models and CFD settings used for the LES simulations are discussed. The detailed explanation of these model is already given in Section 2.4

Spatial discretisation

All convection calculations are done by using second-order schemes.

Temporal discretisation

The second-order time discretisation is advised to be used in LES [16], for a more accurate discretisation.

Gravity

The gravity model is activated, acting in the negative y-direction, unless a different direction is mentioned.

SGS model

The recommended SGS model in Star-CCM+ is the WALE SGS model, and therefore this model is used for all LES simulations. The effect of a different SGS model is not investigated.

Multiphase model

The VOF model is selected to model the multiphase interactions between oil and air, as it proved to be successful in the work of Moghe and Janowiak. The EMP is not considered as it showed diverging behaviour for the RANS simulations and is more expensive than the VOF model.

3.6. Results and validation (LES)

The LES model described before is developed by reproducing the two test cases discussed in Section 3.2. The results of these reproductions are presented next.

3.6.1. Flow rate efficiency experiment (DAF)

This test case is considered to be the most reliable study available, since the jets used in the experiment are the same as the piston cooling jets considered in this project. The simplicity of the experiment is another reason for the high reliability of the case. The only downside of the experiment is that downward facing jets are considered, whereas in reality the oil jets are upward facing jets. In the experiment it is assumed that the effect of gravity on the flow rate efficiency can be neglected. This is tested by simulating the 5 L/min jet in an upward and downward facing situation. The iso-surface results of these two tested jets are shown in Fig. 3.19, with an oil phase volume fraction filter between 0.1 and 1.

It can be seen that the results are quite similar in terms of jet behaviour. It appears that the upward facing jet (left) shows slightly more interaction with the surroundings than the downward facing jet (right). Since the main contributor to the disintegration of these jets is the aerodynamic effect, which is higher for an upward facing jet, this outcome makes sense. An indication of the higher level of interaction is the larger droplet and ligament production for the upward facing jet. To determine the effect of gravity more accurately, the results for the flow rate efficiency need to be compared to the experimental results for the 5 L/min jet.

An exact determination of the flow rate efficiency is not possible from these figures, since these are instantaneous representations of the jet. The chaotic and random behaviour that characterises turbulent flows makes it unreliable to use instantaneous measurements. The sampled results are used instead. To calculate the flow rate efficiency, first the flow rate through the inlet orifice is needed, which can be calculated with the mass flow. The mass flow is defined as:

$$\dot{m} = \rho A v,$$

with ρ the density, A the area of the inlet orifice and v the velocity. The multiphase interactions are modelled with the VOF method, for which the volume fraction (α) is an important problem parameters. Flow properties

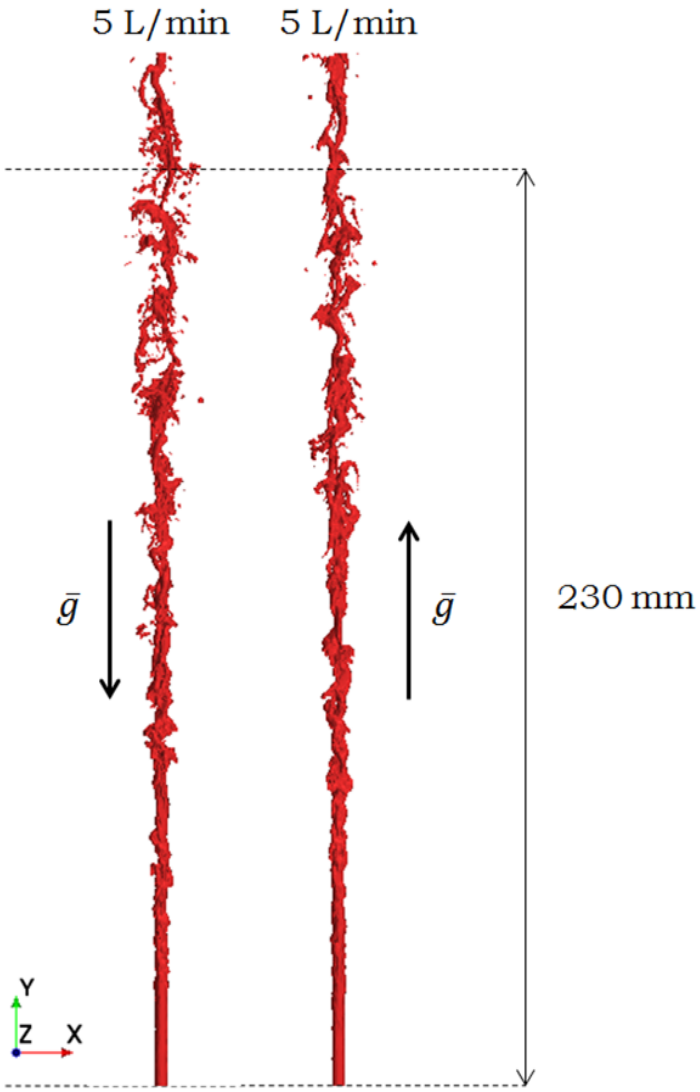

Figure 3.19: Iso-surface results obtained for the reproduction of the 5 L/min jet, for gravity acting in the positive and negative y-direction.

such as ρ and μ are a function of the volume fraction. The interest is in the mass flow of the oil phase only, therefore the density can be defined as a function of the volume fraction of the oil phase:

$$\rho = \alpha_{oil}\rho_{oil}.$$

The area and the oil density are constants, therefore only the volume fraction and the velocity need to be included in the sampling (and the oil density can be used afterwards). However, it is important to explicitly sample the product of these two variables instead of sampling the variables separately and calculating the mass flow at the end of the sampling. Similar to the Reynolds averaging process, the averaged values of separate variables are not the same as the averaged value of their product. The difference between these two is called the covariance:

$$\langle uv \rangle = \langle u \rangle \langle v \rangle + \langle u'v' \rangle .$$

When the sampling is done, the sampled term ($\alpha_{oil}u$) is multiplied with the oil density, resulting in the mass

flow in each cell. Summing these terms for the cells that cover the inlet orifice results in the sampled mass flow of oil through the orifice. The sampled mass flow can then be used to determine the sampled flow rate and the flow rate efficiency. The flow rate efficiency results for both the upward facing and the downward facing jets are plotted in Fig. 3.20.

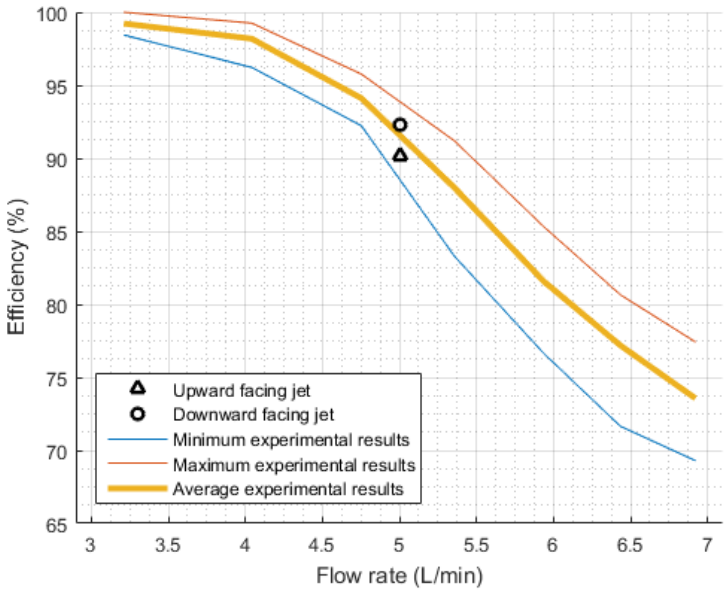

Figure 3.20: CFD results for the flow rate efficiency of the upward and downward facing jets, compared to the experimental results.

It can be seen that both jets show a good agreement with the mean experimental results. It was already shown in the iso-surface figures that the downward facing jet encounters less aerodynamics drag, and shows a slightly smaller spreading behaviour. This is confirmed by the results for the flow rate efficiency, as the efficiency is 2% lower for the downward facing jet. The conclusion that can be drawn from these results is that there is indeed a gravity effect present on the flow rate efficiency, however this difference in very small (2%) and the assumption made in the experiment can be considered as acceptable.

Now that the effect of gravity is shown to be negligible, the remaining flow rates that are reproduced are done for an upward facing situation. This way the results can be used in future studies in this thesis as well, and there is no need to simulate downward facing jets. The tested flow rates are 3, 5 and 7 L/min, such that the range of tested flow rates in the experiment is covered. The input variables to the CFD model and resulting problem parameters are listed in Table 3.1.

Table 3.1: Input parameters to the CFD model for the reproduction of the flow rate efficiency experiment.

Flow rate (L/min)	d (m)	v (m/s)	Re (-)	We (-)	Oh (-)
3	0.003	7.1	1,800	5,100	0.0395
5	0.003	11.8	3,000	14,100	0.0395
7	0.003	16.5	4,200	27,600	0.0395

The flow rate variations are accomplished by varying the velocity and by keeping the diameter of the nozzle constant, resulting in an increase of the Reynolds number. The results for the three tested jets are presented in Fig. 3.21. Again the oil jets are represented by iso-surfaces with a phase-fraction filter between 0.1 and 1.

When analysing this figure, it can be seen that there is clearly more interaction with increasing flow rate, resulting in more disintegration and a larger spreading of the jet. Further, it can be observed that the onset of interaction moves closer to the nozzle with increasing flow rate, as was the case in Fig. 2.4. All these observations indicate indeed that the spreading increases, and thus the flow rate efficiency decreases with increasing flow rate.

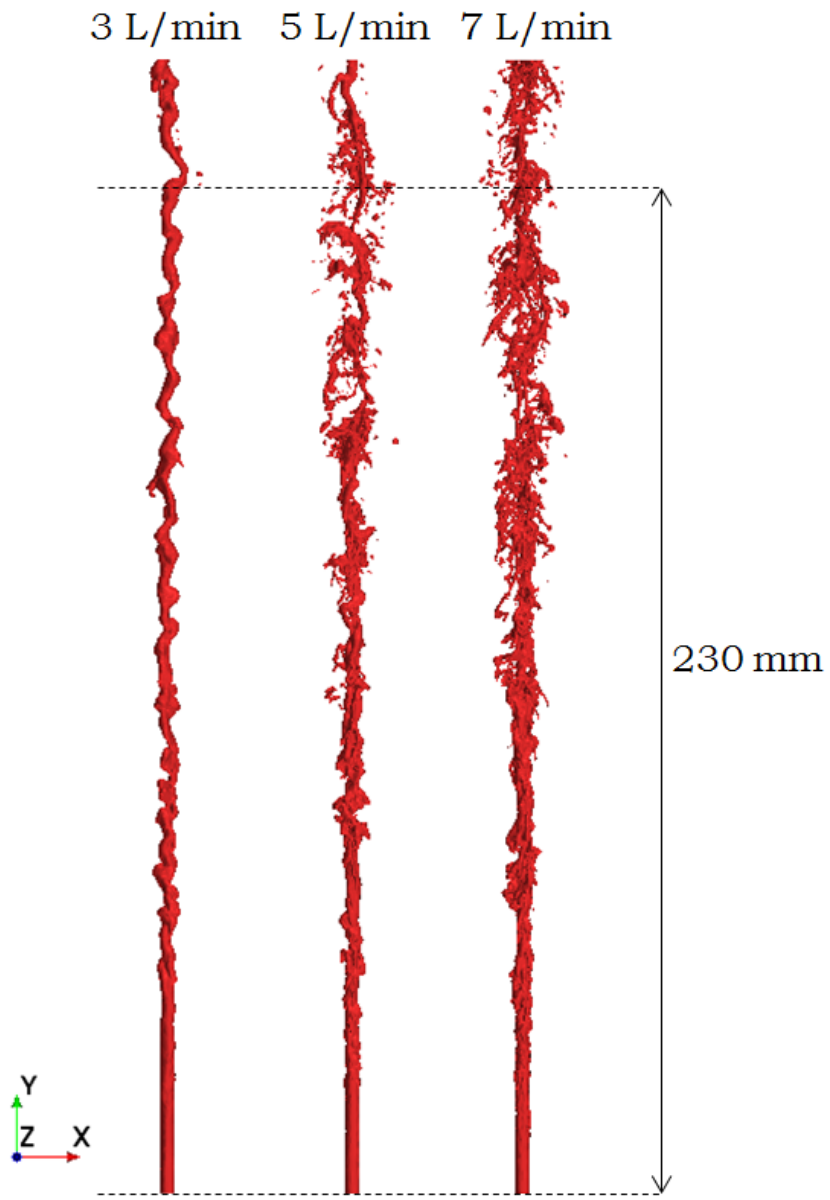

Figure 3.21: Iso-surface results obtained for the reproduction of test case 1, with an oil volume fraction filter between 0.1 and 1.

Further, there is a clear distinction between the type of breakup of the 3 L/min jet and the other two jets. The Reynolds number of the 3 L/min jet is far below the critical Reynolds number (Re = 4,000) and based on Re and Oh, the type of breakup should be in the lower range of the second wind-induced breakup regime. However, based on the results, the breakup shows more agreement with the first-induced breakup mechanism, which is characterised by sinuous waves or oscillations around the jet axis, with no or low droplet formation. The other two jets have a Reynolds number closer to the critical Reynolds number, and this turbulent behaviour is clearly visible in the iso-surface results. A chaotic turbulent breakup can be observed, with a lot of ligament and droplet formation.

To visualise how large the spreading actually is compared to the gallery inlet orifice, the orifice is included to the iso-surface figures, shown in Fig. 3.22.

The next step is to determine the flow rate efficiency and to compare these to the test case results. Again the sampled results are used to determine η. The results are compared to the experimental results in Fig. 3.23,

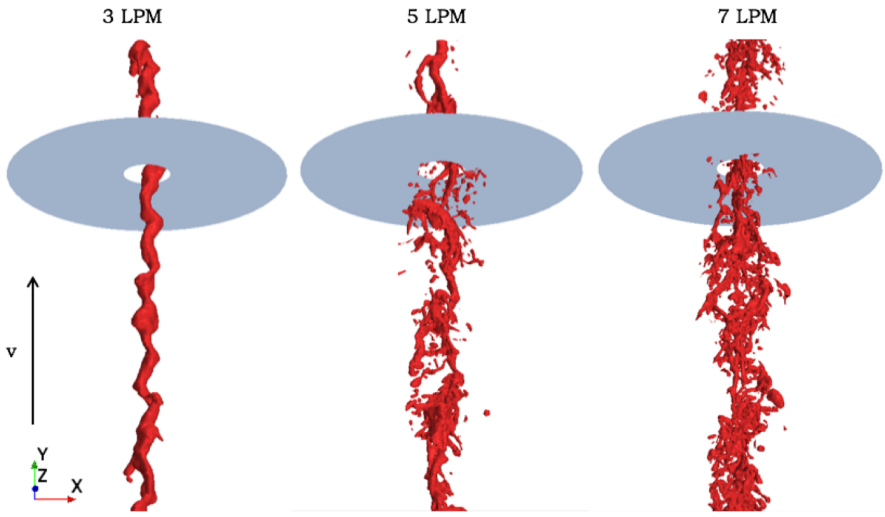

Figure 3.22: Comparison of the iso-surface results of the reproduction of test case 1 to the inlet orifice.

plotted with a vertical uncertainty bar of ±2.5%. The +2.5% of this uncertainty bar is derived by matching the results for the 3 L/min to the experimental results, for which all 6 results are close to η = 99% at 3 L/min. The -2.5% of the uncertainty bar is assumed to contain the discretisation error, which appeared to be present from the mesh sensitivity study.

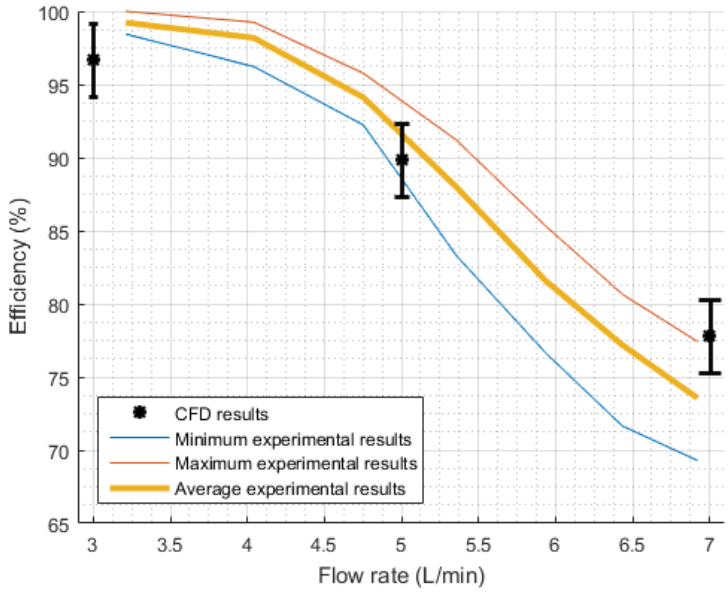

Figure 3.23: CFD results for the reproduction of the DAF flow rate efficiency experiment.

The efficiency calculated for the 3 L/min case is equal to 97%, and the difference with the mean experimental results is 2%. The reason for not having an efficiency of 100% is most likely related to modelling errors or the presence of outliers in the sampled data. From Fig. 3.21 it can be seen that the jet shows an oscillating behaviour, and it could very well be possible that during the sampling the oscillation amplitude exceeded the orifice radius, resulting in oil not entering through the orifice. A longer sampling time would most likely eliminate the effect of these outliers.

A similar observation can be made for the second tested flow rate, which also shows a good agreement with the experimental results (as was shown before). The difference with the averaged results is smaller than 1%.

Even though the level of interaction and type of disintegration is different than the 3 L/min case, the results for the flow rate efficiency are in good agreement with the test case.

The 7 L/min jet is the most turbulent jet that is tested. This was also observed from the iso-surface results in Fig. 3.21. The determined flow rate efficiency for this jet is equal to 78% and is slightly over-predicting the mean experimental results, with a difference of 5%. The reason for the larger deviation (compared to the other two flow rates) could very well be the same reasons given for the deviations of the experimental results itself for higher flow rates, as discussed in Section 2.1.3. The increasing turbulent nature of the jet results in a more chaotic behaviour of the jet, with more ligament and droplet production. For the numerical results this means that more and more outliers are included to the sampled results, and a much longer sampling time could reduce the effect of these outliers. Nevertheless, the flow rate efficiency is still in agreement with the maximum experimental results, and therefore these results are accepted.

An indication of the increasing interactions and chaotic behaviour can be obtained by checking the mass imbalance of the system, which is used to optimise the initialisation and sampling time, as discussed in Section 3.5. The CFL number (or the time step) plays a role in the elimination of this mass imbalance, and if this number is too high, mass is created inside the domain and this directly influences the calculation of the flow rate efficiency. The final CFL numbers needed to eliminate the mass imbalance for the three cases are shown in Table 3.2. It can be seen that the CFL numbers need to be decreased with increasing turbulence levels to eliminate the mass imbalance.

Table 3.2: Indication of the CFL numbers needed in order to balance the mass for the three tested flow rates.

Flow rate (L/min)	grid size (mm)	time step (s)	v (m/s)	CFL (-)
3	0.02	$5{\cdot}10^{-6}$	7.1	0.19
5	0.02	$3{\cdot}10^{-6}$	11.8	0.17
7	0.02	$1.8{\cdot}10^{-6}$	16.5	0.15

The final step to take is to assess whether the LES results are reliable by checking the LES quality metric, presented in Fig. 3.24. It can be seen that this value is clearly above 0.8 in the region of interest for all three cases.

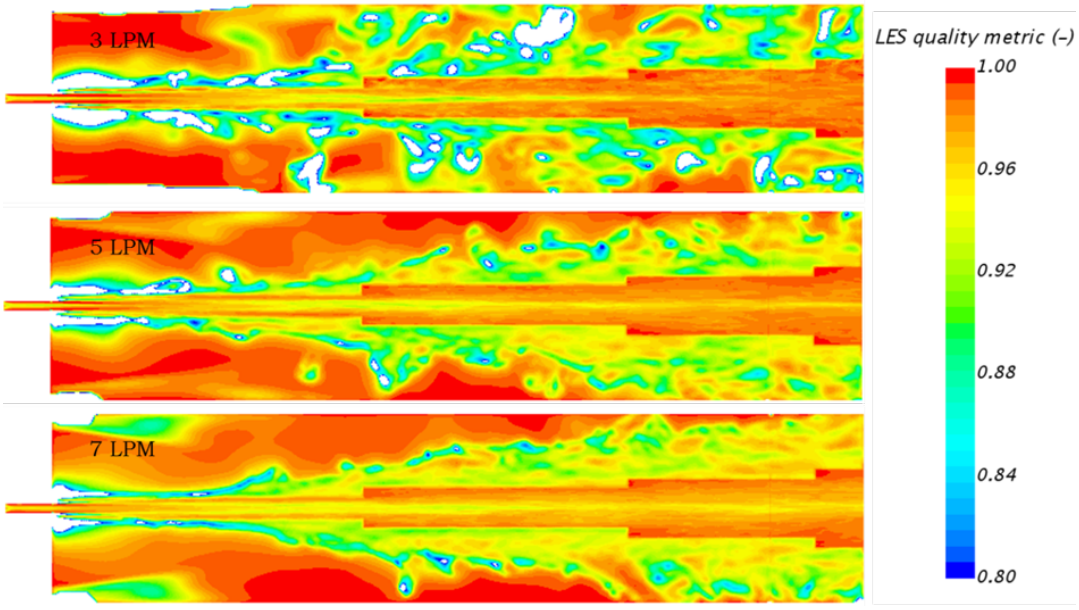

Figure 3.24: Results for the LES quality metric, obtained from the reproduction simulations of test case 1.

3.6.2. Moghe and Janowiak (Case B)

Since the jet with Re = 4800 is most similar to the DAF jets in terms of the Reynolds number, only this jet is reproduced for the reproduction of test case 2. There are several reasons for not reproducing the other two cases. Firstly, the method used in the test case to determine the spreading is not reliable. The researchers used the instantaneous spreading, for which it is known (from the results presented in Section 3.6.1) that this spreading varies in time. Secondly, the domain needed to simulate these jets is larger than the domain needed for the DAF jets, resulting in a significant increase of computation time per simulation. Lastly, the agreement obtained with test case 1 is considered to be good enough to proceed to the trend analysis with this CFD model.

The input parameters to the CFD model for the reproduction of test case 2 are listed in Table 3.3.

Table 3.3: Input parameters to the CFD model for the reproduction of test case 2.

Flow rate (L/min)	d (m)	v (m/s)	Re (-)
11.1	0.0035	19.24	4,800

The results of the test case contain only the iso-surfaces, and therefore only this figure is produced and compared to the test case, in Fig. 3.25. It can be seen that the shape of the jet is very similar to the test case results. The surface instabilities that lead to the disintegration are similar in size and the onset of spreading starts at around 40% of the target distance, which is also in agreement with the test case results. The main difference is the amount of droplet and ligament productions, which appears to be larger for the CFD results. A possible reason for this is the smaller cell size used (1.5 times smaller than the cell size used in the test case). An indication of how the cell size determines the size of the droplets is indicated in Fig. 3.26. Since a certain number of cells are needed to resolve (and visualise) these droplets, smaller and more droplets can be resolved on a finer mesh.

The main parameter of interest is the spreading distance of the jet at a target distance of 283 mm. The spreading measured in the test case is 25 mm for their LES results and 26 mm for their experimental results. As mentioned before, this is obtained from an instantaneous iso-surface for the volume fraction. When the same strategy is used for the CFD results, the larger number of droplets produced makes it difficult to decide which droplets to include and which droplets not to include to the measurement of the spreading. Therefore, instead of measuring the spreading, a 25 mm bar is plotted in the iso-surface results and this is analysed. As the chaotic nature of the turbulent jet results in a different spreading at different time instants, three different iso-surface figures are produced, shown in Fig. 3.27.

It can be seen that the first and second iso-surfaces show a reasonable agreement with the 25 mm spreading bar, whereas the agreement of the third iso-surface figure is less good. The spreading at this time instant is much smaller than 25 mm. The conclusion that can be drawn is that, firstly, the method of measurement is very questionable because of the droplets and, secondly, the highly turbulent jet results in a spreading that varies in time and therefore it is not reliable to use instantaneous results. It cannot be said that a proper validation with test case 2 is done for the spreading distance, nevertheless there is a positive outcome when a visual comparison is done.

3.6.3. Computation time

The high computation time related to LES is already addressed several times throughout this chapter. In this section, an indication of this computation time is given. The problem parameters that are affecting the computation time are listed in Table 3.4, for the three simulations of the DAF jets.

It can be seen that with increasing Reynolds number, there is a longer sampling time needed in order to obtain converged results for the mass flow through the inlet orifice. The scalability of the LES simulations on different number of CPU's is determined and plotted in Fig. 3.28. It can be seen that up to 240 cores there is a good agreement with the theoretical speedup, and above this number the deviation starts to increase and certain computational limit is approached.

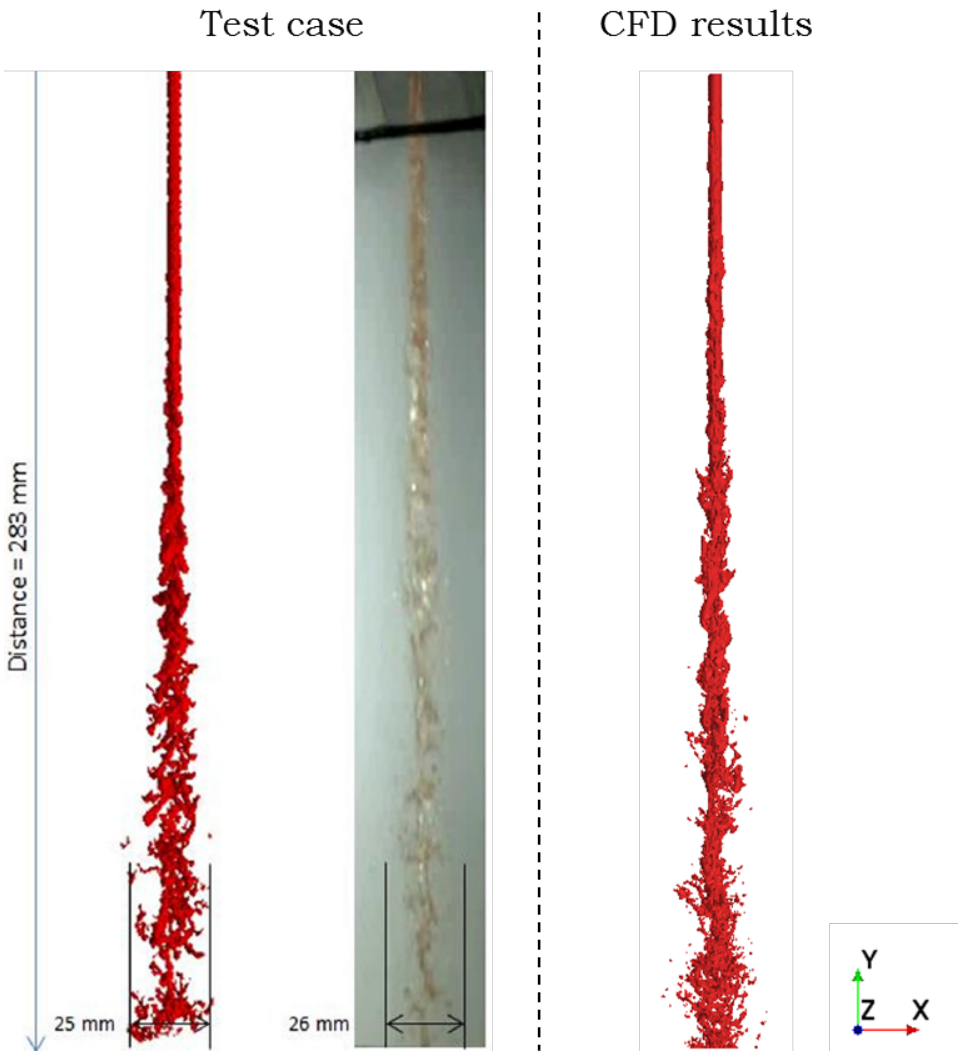

Figure 3.25: Comparison of iso-surface results to the test case results.

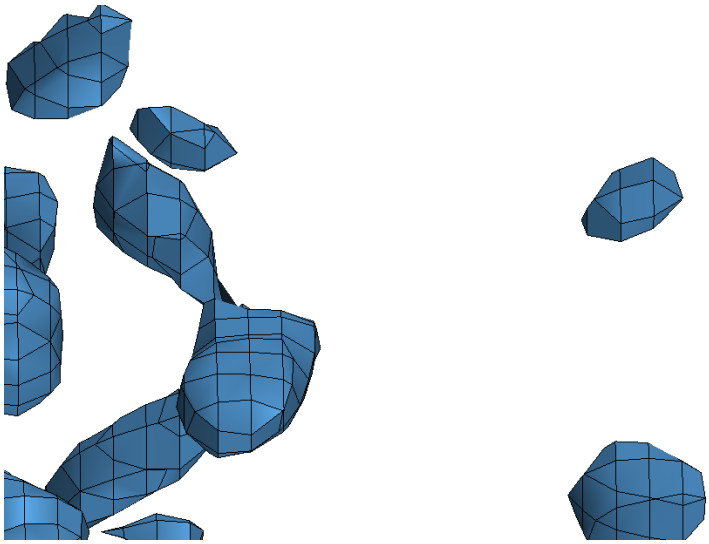

Figure 3.26: Indication of how the mesh size determines the size of produced droplets (and ligaments).

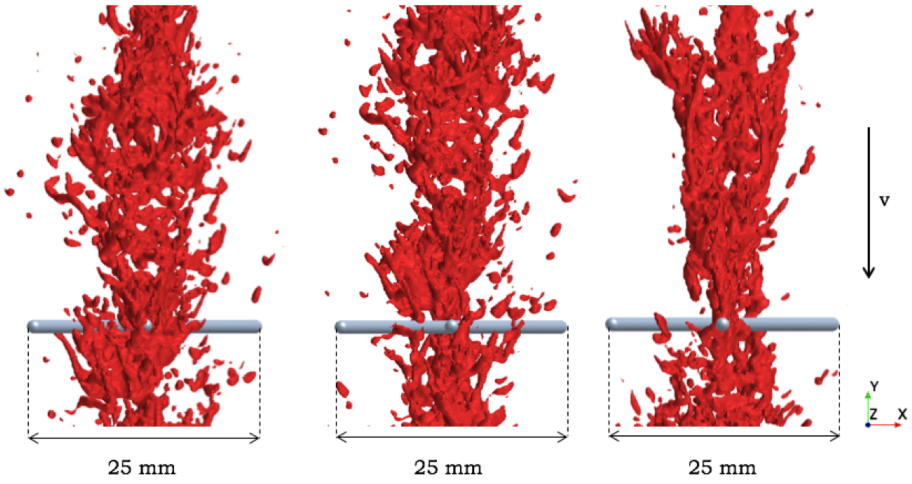

Figure 3.27: Close-up of CFD results with a 25 mm bar included to compare the spreading distance.

Table 3.4: Indication of the computation time needed for the different reproduction simulations.

	$3\ L/min$	$5\ L/min$	$7\ L/min$
Number of cells (-)	6.1M	6.1M	6.1M
Reynolds number (-)	1,800	3,000	4,200
Initialisation (time steps)	32,000	32,000	32,000
Sampling (time steps)	14,000	18,000	20,000
Computation time on 192 cores (hrs)	65	70	74

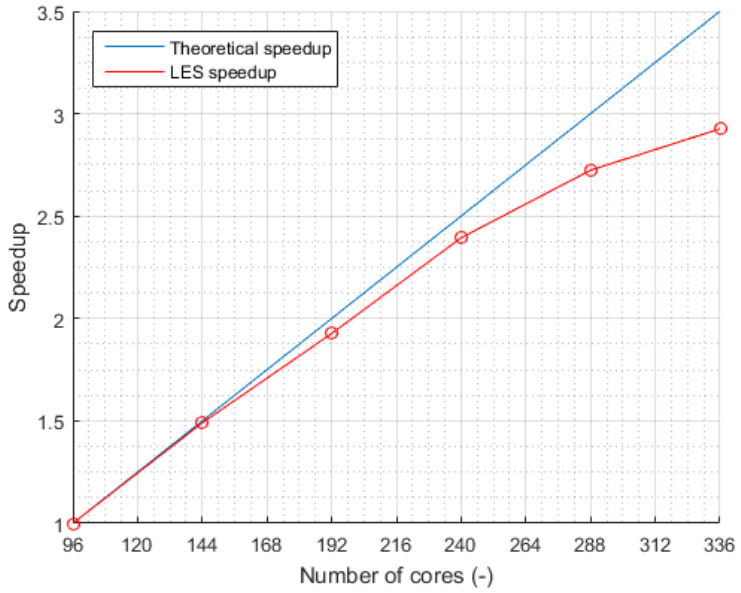

Figure 3.28: Estimation of total computation time for the reproduction simulations versus the number of cores used.

3.7. Trend analysis

Now that the CFD model is able to reproduce the test cases within an acceptable accuracy, the model is now used to analyse the DAF jets. This is done in the form of a trend analysis, by varying several problem parameters and determining the effect of these variations on relevant output parameters. Because of the extremely high computation time needed for a reliable set of samples, this analysis is done varying three

input parameters only: the flow rate, the oil temperature and the nozzle diameter. The test set-up of the trend analysis is shown in Table 3.5. The effect of one input parameter is investigated by keeping the other two input parameters at their reference value.

Table 3.5: Trend analysis set-up for the analysis of the DAF oil jet.

Input parameter	Range	Reference value
Flow rate (L/min)	[3, 5, 7]	7
Temperature ($°C$)	[80, 100, 120]	100
Diameter (mm)	[2, 3, 4]	3

The trends are investigated for the output parameters that are relevant for the two piston cooling techniques discussed in Chapter 2: the gallery cooling technique and the spray cooling technique. The relevant parameter for the gallery cooling technique was mentioned to be the flow rate efficiency. For the spray cooling technique, the relevant flow parameters are the parameters that determine the Reynolds number and Prandtl number, as mentioned in Section 3.1. Since VOF is used as the multiphase model, all flow properties (except for the velocity) can be determined with the volume fraction. The relevant output parameter for the spray cooling technique is therefore the sampled volume fraction and the sampled velocity.

To evaluate the effect of varying input parameters for a complete engine cycle, 5 equally spaced piston locations are defined first: BDC, Q1, Q2, Q3 and TDC. These piston locations and their position with respect to the nozzle exit are shown in Fig. 3.29.

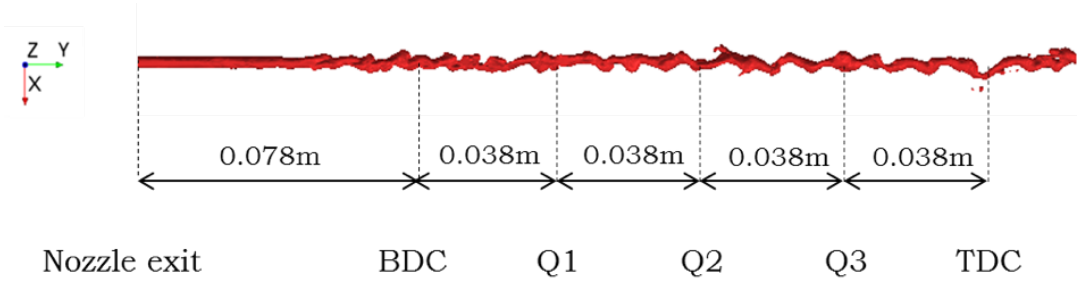

Figure 3.29: Equally spaced piston locations (between BDC and TDC) to evaluate the trends.

3.7.1. Flow rate effect

The first test is performed by varying the flow rate. The reason for investigating the flow rate effect is because variations in flow rate are directly related to the oil pressure provided by the oil pump. The power needed for the pump is provided by the engine output power, and thus is a loss of shaft power. Decreasing the power requirements of the pump means that less fuel is needed to provide the same shaft power.

The flow rates and the resulting parameters that are tested are listed in Table 3.6. The reproduction of test case 1 was already an investigation of the effects of different flow rates on the upward facing oil jets, therefore these results are used and extended in this trend analysis. With the extremely high computation time needed to obtain a reliable set of samples (and with the increase of computation time with increasing flow rates/turbulence levels), the investigation of the 9 L/min is not considered.

Table 3.6: Flow rates that are tested and resulting problem parameters.

Flow rate (L/min)	d (m)	v (m/s)	T ($°C$)	Re (-)	We (-)	Oh (-)
3	0.003	7.1	100	1,800	5,100	0.0395
5	0.003	11.8	100	3,000	14,100	0.0395
7	0.003	16.5	100	4,200	27,600	0.0395

The iso-surface results for the three tested flow rates are shown in Fig. 3.30, with a phase volume filter between 0.1 and 1. The output parameters will now be determined by using the sampled results.

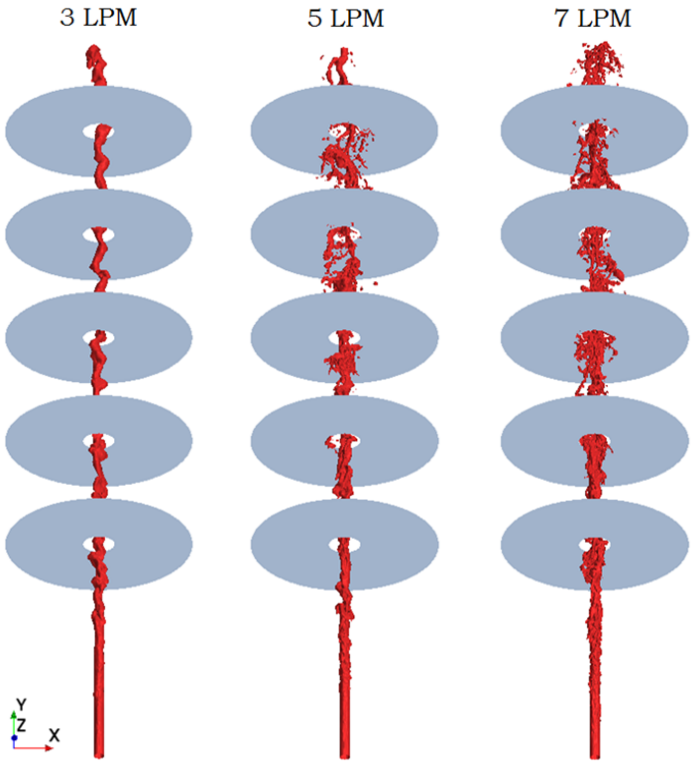

Figure 3.30: Iso-surface results for the flow rate effect, with a phase-fraction filter between 0.1 and 1.

Flow rate efficiency

The efficiency determined for each piston location is plotted in Fig. 3.31. All three tested flow rates result in an efficiency between 99% and 100% at the BDC position of the piston. This means that all the oil is entering the cooling gallery when the piston is at its lowest position. The BDC location of the piston with the currently used nozzle (3 mm) is at a nozzle-to-target distance of $L/d = 31$. It was mentioned in Chapter 2 that short jets ($L/d < 30$) can be considered as jets that remain reasonably constant in terms of interaction and spreading, which is thus confirmed by these results.

For the other locations, a (close to) linear decrease of the flow rate efficiency can be observed as the piston moves upwards. The slope of the plots is an indication of how high the level of interaction is. The conclusion drawn earlier for the reproduction of test case 1 is also valid for the other piston locations: the increasing flow rate results in more spreading, and thus a decrease of flow rate efficiency. With respect to gallery cooling this would mean that less oil will enter the cooling gallery as the piston moves up, resulting in a decrease of the oil-fill ratio (OFR), as explained in Chapter 2. However, it is unknown how the OFR influences the cooling for the DAF pistons and therefore no conclusions on this can be drawn.

Volume fraction and velocity

The flow rate effect on the volume fraction and the velocity of the jet are investigated next. Again, these are obtained for the defined piston locations. The results for the sampled volume fraction are shown in Fig. 3.32. These results are obtained by performing a radial averaging on the piston locations. The dashed lines represent the inlet orifice walls, to indicate how large the spreading is compared to the cooling gallery inlet.

At all piston locations, a similar flow rate effect can be observed: the volume fraction on the jet centre axis decreases with increasing flow rate. Due to the increasing level of interaction and spreading, the volume fraction sample contains more and more air. Further, it can be observed that there is also a widening of the

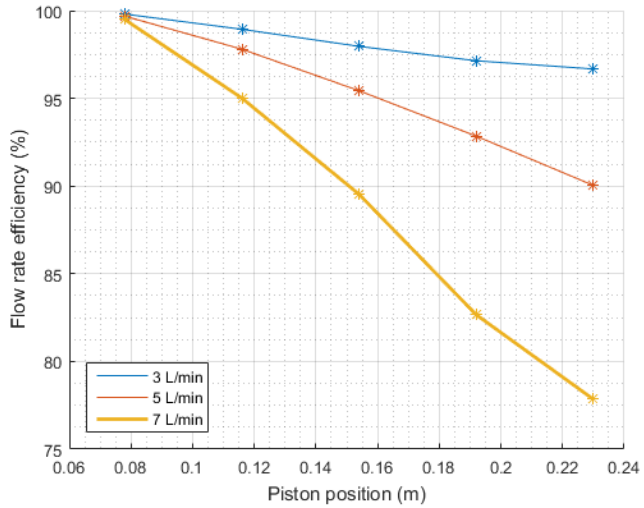

Figure 3.31: Flow rate efficiency results for the tested flow rates at the defined (five) piston location.

volume fraction plots with increasing flow rates, which is indication of the spreading behaviour of the jet. It can be seen that these two effects are stronger when the piston moves upwards. The conclusion that can be drawn is similar to the conclusion drawn before: increasing flow rates result in increasing chaotic and spreading behaviour. More oil is observed at outer parts of the jet (the spreading) and less oil in the centre of the jet (decrease of centre line volume fraction).

The same plots can be obtained for the sampled velocity (in axial direction) of the jet, shown in Fig. 3.33. The flow rate effect on the velocity is not surprising, as the velocity is varied to vary the flow rate. However, when the results are compared for the different piston locations, a similar trend can be observed as was the case for the volume fraction: there is widening of the profiles with increasing piston position. In contrary to the volume fraction, the maximum velocity (in the centre of the jet) remains reasonably constant for increasing piston position.

It should be noticed that the velocity cannot be used to extract additional information from, as there is no information about which part of the profile is the velocity of the oil phase and which part of the air phase. The sampled volume fraction results are sufficient to observe the behaviour of the jet. Therefore, the sampled velocity plots for the remaining trend analyses are not included in this chapter, but can be found in Appendix B. These plots are used in Chapter 5 to investigate the effect on the heat transfer in spray cooling.

3.7.2. Temperature effect

The second tested input parameter is the oil temperature. Since engine oil is a fluid for which the fluid properties are very sensitive to changes in temperature, this is an interesting trend. In practice it is difficult for DAF to control the oil temperature, as this is determined by all sorts of different factors in a running engine. Nevertheless the effect is of interest for the company. The test set-up is again presented in Table 3.7. A detailed overview of the variations of oil properties with temperature can be found in Appendix A.

Table 3.7: Temperatures that are tested and resulting problem parameters.

T (°C)	Flow rate (L/min)	d (m)	v (m/s)	Re (-)	We (-)	Oh (-)
80	7	0.003	16.5	2,600	28,000	0.0653
100	7	0.003	16.5	4,200	27,600	0.0395
120	7	0.003	16.5	6,300	27,100	0.0261

It can be seen that, besides the Reynolds number, now also the Ohnesorge number is affected by the varying fluid properties. Fig. 2.2 can help in the determination of what can be expected from this trend analysis. The

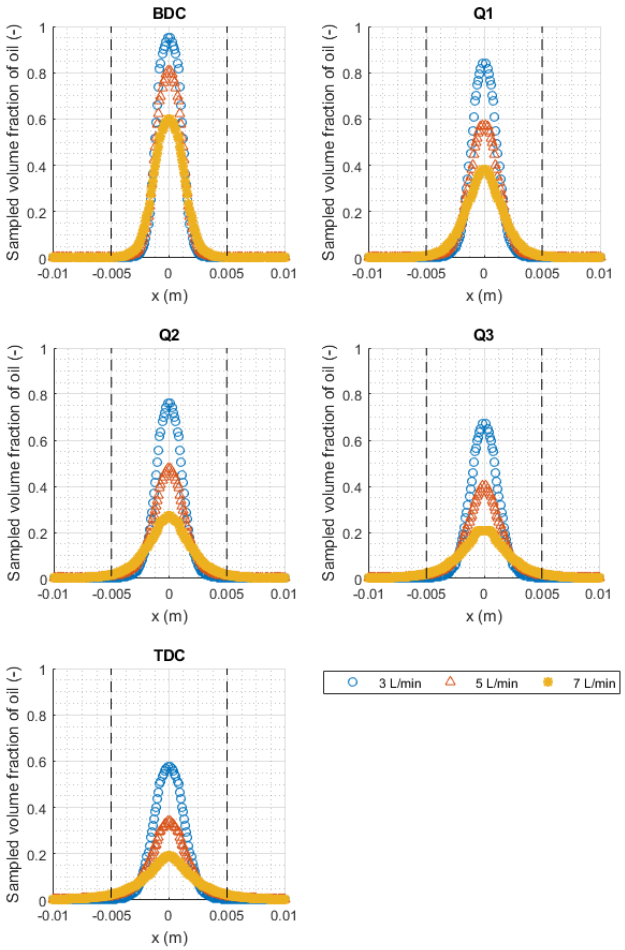

Figure 3.32: Sampled oil volume fraction results for different flow rates at different piston locations.

increasing Reynolds number is equivalent to moving to the right in Fig. 2.2, which means that the level of interaction should increase, and a more chaotic and spreading behaviour can be expected. The decreasing Ohnesorge number is equivalent to moving upwards in Fig. 2.2, which should results in a similar outcome.

The tested range of Reynolds numbers is larger than it was for the flow rate effect, thus it can be expected that the difference between lowest and highest tested oil temperatures are even larger. When the iso-surface results are produced, this expected outcome is not observed, as can be seen in Fig. 3.34. There is certainly an increase of interaction and spreading behaviour with increasing oil temperature, however it is much less than what was observed for the flow rate. A more reliable investigation is again done by determining the flow rate efficiency and the sampled volume fraction plots.

Flow rate efficiency

The flow rate efficiency is again calculated in a similar way as was explained before. The results are plotted in Fig. 3.35. It can be seen that again the efficiency at the BDC location is hardly affected by the oil temperature, as was also observed the flow rate effect. These results again confirm that for short jets ($L/d < 30$), the jet properties remain reasonably similar to the nozzle exit conditions.

For the other locations, the observed oil temperature effect is that the flow rate efficiency decreases with increasing oil temperature, as was expected. However, also from these results it is clear that the temperature effect is not as strong as the flow rate effect. Especially the differences between the 100 °C and the 120 °C jet remain below a flow rate efficiency of 5%, and this can be considered as small.

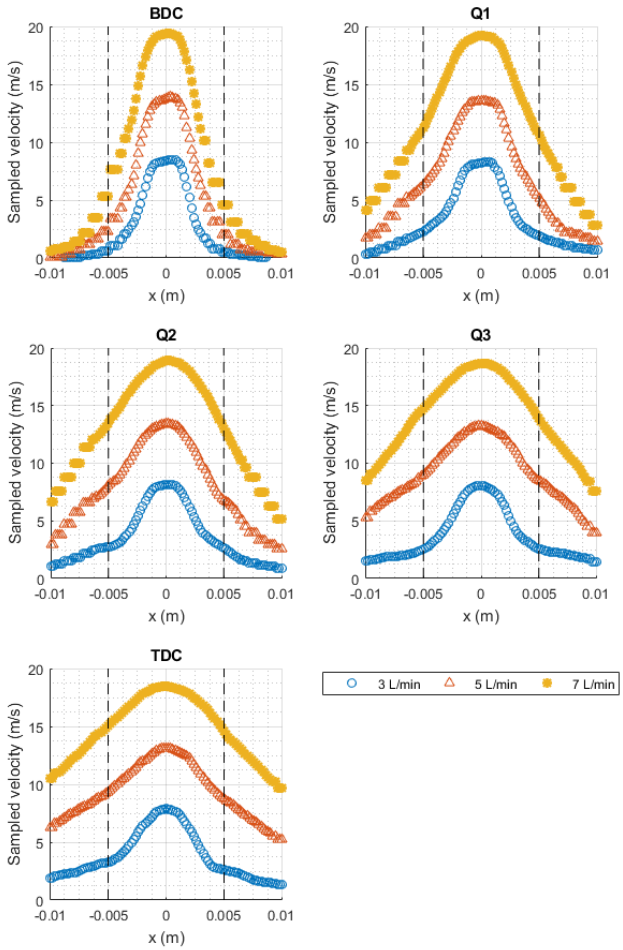

Figure 3.33: Sampled velocity (in y-direction) results for different flow rates at different piston locations.

A reason for this outcome could be that the behaviour of the jet is not a function of only the Reynolds number. There could be a (stronger) dependency on dimensional parameters as well, such as the velocity of fluid properties ρ and/or μ. Another reason could be that a certain limiting case is reached (in terms of interaction and chaotic behaviour) when the jets are in the fully turbulent region ($Re > Re_{critical}$), and that all jets in this region behave similarly. A third reason for this outcome could be the surface tension effect. An important assumption made was that the surface tension is assumed to be the same for all tested oil temperatures, while in reality the surface tension decreases with increasing temperature. One can expect that with a lower surface tension, more disintegration will occur, and the differences will be larger. The relation between oil temperature and surface tension is unknown for the 10-W30 engine oil at DAF (and in literature), and needs to be determined first before this effect can be investigated (in future studies).

Volume fraction

The sampled volume fraction results are presented in Fig. 3.36. From these figures, it can be observed that there is a clear effect when the oil temperature is increased form 80 to 100 °C. When the temperature is increased from 100 to 120 °C, this effect is much smaller. This is thus in accordance with what was observed for the flow rate efficiency results.

It can be seen that again there is a decrease of volume fraction in the centre, with increasing oil temperature, for the same reasons as given before. The widening of the jet appears to be similar for all tested temperatures and not really affected by the oil temperature.

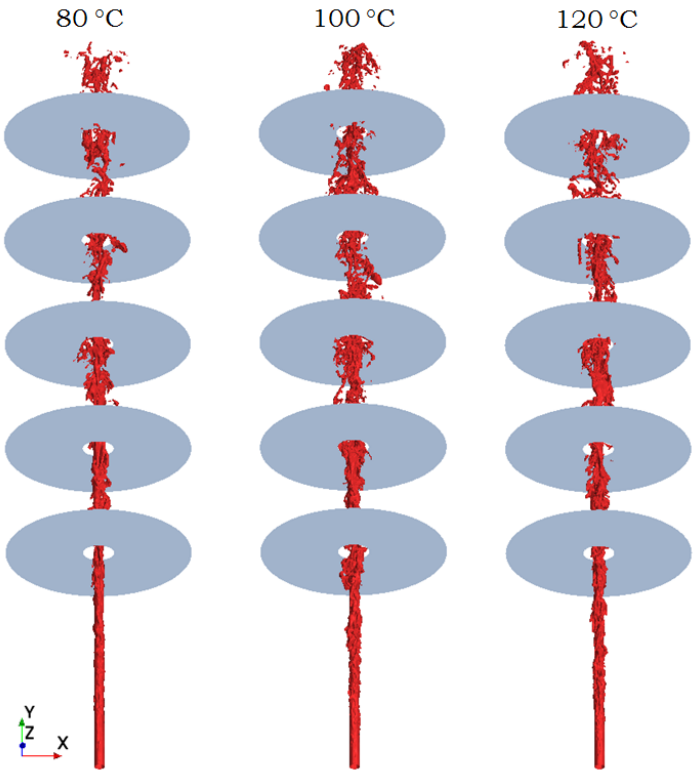

Figure 3.34: Iso-surface results for the temperature effect, with a phase-fraction filter between 0.1 and 1.

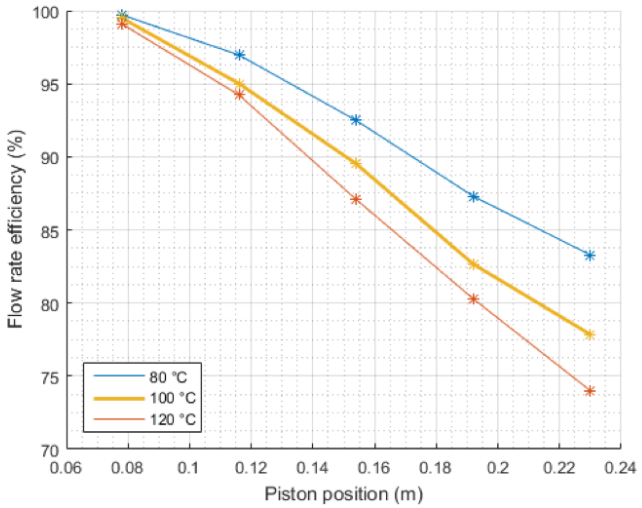

Figure 3.35: Flow rate efficiency results for the tested temperatures at the defined (five) piston location.

3.7.3. Diameter effect

The nozzle diameter is the final tested input parameter. From an industrial point of view, this effect is very interesting because the jet behaviour can be influenced in a relatively easy manner: by implementing a different nozzle (diameter). Especially compared to varying (or controlling) the oil temperature. The tested diameters and the resulting problem parameters are listed in Table 3.8.

In order to maintain a constant flow rate, the velocity needs to be varied with varying nozzle diameter. The range of Reynolds that are tested is similar to the range for the temperature effect, between 3,200 and 6,300.

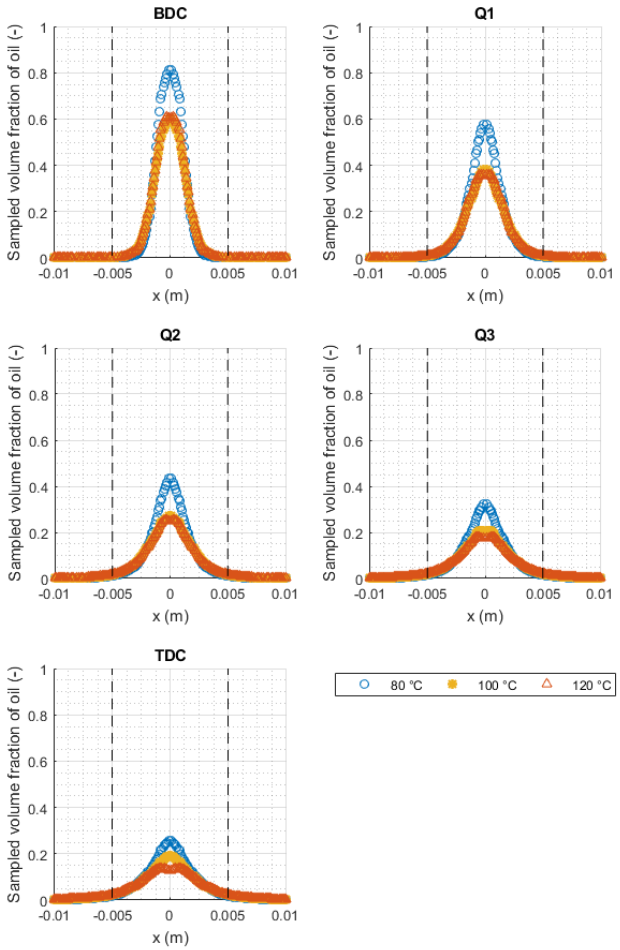

Figure 3.36: Sampled oil volume fraction results for temperatures at different piston locations.

Table 3.8: Nozzle diameters that are tested and resulting problem parameters.

d (m)	T (°C)	Flow rate (L/min)	v (m/s)	Re (-)	We (-)	Oh (-)
0.002	100	7	37.1	6,300	92,900	0.0484
0.003	100	7	16.5	4,200	27,600	0.0395
0.004	100	7	9.3	3,200	11,600	0.0342

The results for the iso-surfaces are shown in Fig. 3.37.

Flow rate efficiency

The results for the flow rate efficiency for the three tested diameters are plotted in Fig. 3.38. In this test both the diameter and the velocity of the jet are varied, therefore the effect is more difficult to understand. The flow rate efficiency is affected when the spreading of the jet is such that the local diameter of the jet exceeds the inlet orifice diameter. When a larger nozzle diameter is used, this would mean that less spreading is needed to affect the flow rate efficiency. The opposite is true for a smaller nozzle diameter: this jet needs to spread much more in order to affect the flow rate efficiency. If variations in diameter were the only variations, one could say that the jet with the largest diameter will have the largest spreading and thus the lowest efficiency.

For the velocity effect (or flow rate effect), it was shown that the flow rate efficiency decreases with increasing velocity. This means that when both variations are combined, two counteracting effects will be present. Which of the two variations is more dominant for the flow rate efficiency can be investigated by plotting again

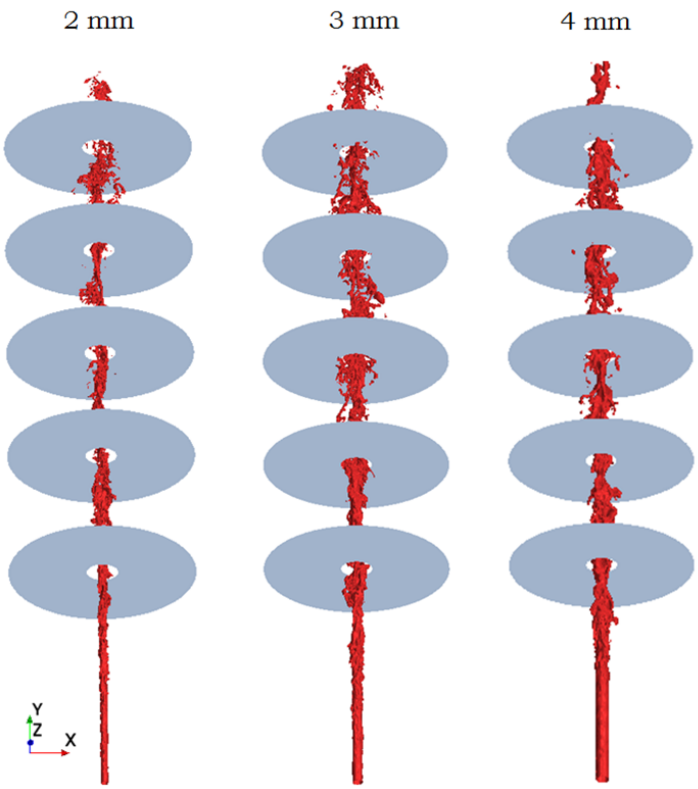

Figure 3.37: Iso-surface results for the diameter effect, with a phase-fraction filter between 0.1 and 1.

the efficiency at the different piston locations. These plots are shown in Fig. 3.38.

It can be seen that this is the first time that the efficiency at the BDC location is affected, for the largest tested diameter. It can thus be said, that variations in diameter are dominant at this piston locations, since the highest diameter shows a decrease, and not the jet with the highest velocity. This does not mean that the 4 mm jet is more turbulent or shows more interaction than the other two jets: the 2 mm jet is the most turbulent one, but this jet simply is not wide enough (yet) to affect the flow rate efficiency.

When the highest piston location is analysed, it can be seen that the lowest efficiency is obtained with the smallest diameter. At this piston location, the most turbulent jet also results in the lowest flow rate efficiency. The dominant variation is the velocity now, and not the nozzle diameter. When the slopes of the plots are analysed, it can be seen that indeed the flow rate efficiency is decreasing much faster when the diameter is decreased and the velocity is increased (for these piston locations).

The main conclusion is thus that at a lower piston location, the diameter effect is more dominant. As mentioned before, this does not mean that this jet is showing more interaction or chaotic behaviour; it is simply the widest jet and needs the least amount of spreading to affect the flow rate efficiency. For higher piston location the opposite is observed. The turbulent behaviour of the jets are now dominant, and the smallest diameter jet now results in the lowest flow rate efficiency.

Volume fraction

The sampled volume fraction profiles for the investigation of the diameter effect are presented in Fig. 3.39. The results at the BDC location of the piston nicely shows the difference in spreading, which is clearly caused by the initial nozzle diameter. As the piston moves upwards, the volume fractions in the centre again are decreasing and the widening of the plots is increasing.

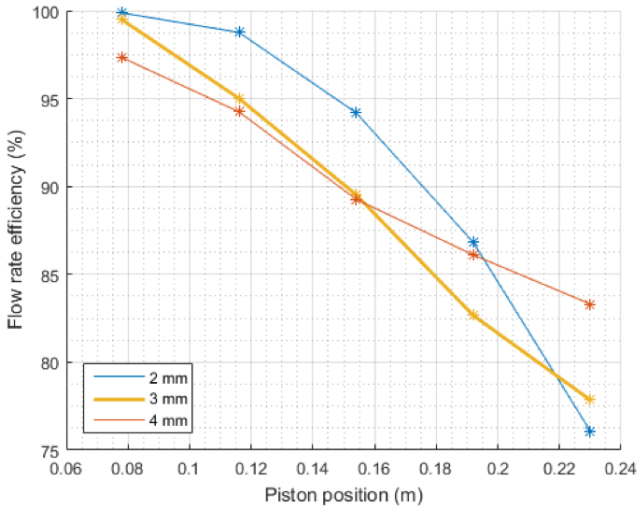

Figure 3.38: Flow rate efficiency results for the tested diameters at the defined (five) piston location.

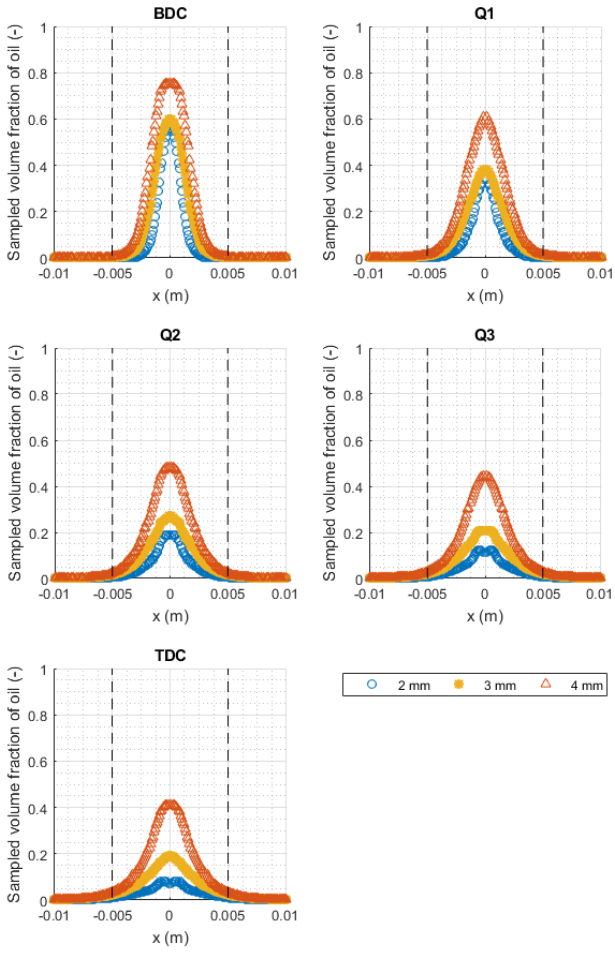

Figure 3.39: Sampled oil volume fraction results for different nozzle diameters at different piston locations.

3.8. Conclusions

The first sub-project of this thesis contains the investigation on the isolated oil jet. The main conclusions from this investigation can be summarised as follows:

- The RANS-VOF combination proved to fall short in modelling the oil jet characteristics. It was found that the tendency of the VOF multiphase model to maintain a sharp interface between the phases is the reason for this outcome. When the VOF convection order is lowered to decrease this tendency, the results are unaffected on a structured grid. On a polyhedral grid this results in the introduction of numerical diffusion and a significantly different outcome.
- The LES-VOF combination was successfully used to reproduce the flow rate efficiency experiment by DAF, showing a decreasing flow rate efficiency with increasing flow rates. This is an indication of the increasing spreading behaviour of the jet.
- The gravity effect on the flow rate efficiency was shown to be negligible (2%).
- The reproduction of the LES study of Moghe and Janowiak could not properly be validated because of (1) their unreliable method for measuring the spreading and (2) the fact that they have used one instantaneous result for these measurements.
- The trend analysis results for the flow rate effect showed that at different piston locations (except for the BDC) there is a clear flow rate effect: a decreasing flow rate efficiency as the flow rate is increased. The volume fraction plots confirmed this, as there was a larger spreading with increasing flow rate.
- The effect of the oil temperature was shown to be not as strong as was expected, based on the dimensionless numbers that determine the breakup mechanism. Possible reasons were given to be either a strong dependency on dimensional numbers (instead of the Reynolds number), the approach of a limiting behaviour for Reynolds numbers above the critical Reynolds number and/or the assumption of constant surface tension for the tested jets. Nevertheless, there was a decreasing flow rate efficiency observed when the oil temperature is increased, and thus an increasing spreading behaviour.
- The diameter effect was shown to be more difficult than the first two tests. There are two counteracting effects present when the diameter is varied (at constant flow rate): the diameter and the velocity. At lower piston locations, the diameter itself was shown to be dominant for the flow rate efficiency, whereas for higher locations the velocity of the jet was more dominant in the determination of the flow rate efficiency.
- It is shown that all three tested input parameters can be used to influence jet behaviour, in terms of spreading. The effect on piston cooling cannot be determined yet and is investigated in later stages of the project (or needs to be investigated in future studies).

4

Impingement

Now that the isolated oil jet is investigated and the jet properties at relevant piston locations are determined, the next step in this research project is to investigate the impingement of the jet. Instead of performing a full scale investigation of piston cooling, first the problem is simplified to the impingement of an oil jet onto a flat surface. The goal is to develop a reliable CFD model in Star-CCM+ by again reproducing test cases and applying the validated CFD model to perform a trend analysis. The developed CFD model is extended to a more realistic (piston cooling) configuration in the next chapter.

This chapter is structured as follows. The problem description is discussed in more detail first in Section 4.1. Next, past work selected as validation material is shown in Section 4.2, followed by the presentation of the CFD model in Section 4.3. Section 4.4 shows the results obtained with the CFD model and the comparison of these results with the validation data. Finally, a trend analysis is performed to show the effect of input parameters on the heat transfer, in Section 4.5. The chapter ends with a concluding section.

4.1. Problem description

A full scale investigation of the piston cooling problem is a complex problem involving several complex phenomena, such as a reciprocating piston, interactions between the piston and the jet, interactions between the jet and surrounding air, effect of the piston geometry on the flow field and finally the heat transfer between the oil and the piston. From a modelling point of view, one can combine all of these phenomena in one simulation and produce results for the heat transfer and the piston temperature. The remaining question then is: how reliable are these results? Since there is no (experimental) data available for the DAF pistons and this is the first CFD study performed at DAF on piston cooling, it is difficult to develop this CFD model and validate it properly.

The methodology is therefore to simplify the piston cooling problem in such a way that a validation is possible. This simplified problem is analysed in this chapter, by first reproducing the selected test cases, then validating the CFD model and finally applying it to the operating conditions of the DAF jets. The starting point for this simplified problem is the spray cooling method. The first simplification is the representation of the piston as a constant thickness disc, removing the confinement caused by the cylinder walls in which the piston is moving and shifting the impingement location to the centre of the disc. By doing this, the complex lower surface of the piston is now represented as a flat surface and the problem is reduced to an axisymmetric one, which is very beneficial from a modelling point of view. The removal of the cylinder is also related to a decrease of computation time. According to [43], the results for the Nusselt number in the stagnation zone are unaffected by the confinement for $R/d > 11.5$. The smallest R/d considered in this project is equal to 16, with $R = 64$ mm and the largest tested jet diameter $d = 4$ mm.

The second simplification is the assumption of a short and constant target distance. The real piston operates

between the BDC and TDC locations and it was shown in the previous chapter that the jet composition significantly changes when the jet reaches the piston. Since the LES method is considered to be too expensive for a heat transfer problem, the RANS method is used, for which it is shown that it can only be used to model short jets, with low levels of interaction with the surrounding air. Another important result of this simplification is that the motion of the piston is not considered. The motion of the piston affects the effective velocity of the jet, and by neglecting the motion of the piston, the focus can be on determining the heat transfer for a static configuration.

The final simplification is related to the thermal boundary conditions. In reality the heat is created by combustion, which is a complex process resulting in a heat flux that is depending on the piston bowl geometry. For the simplified problem it is assumed that there is a constant heat flux, applied to the top surface of the disc, and that this heat is removed only through the lower surface of the disc. A schematic of the final configuration is shown in Fig. 4.1.

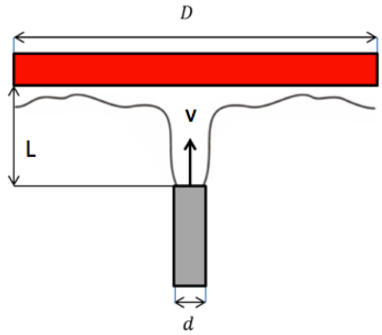

Figure 4.1: 2D schematic of the simplified heated disc problem.

4.2. Validation material

The validation material is selected based on the similarity between the performed study and the simplified problem. Three test cases are selected: an experiment, a simulation and an analytical study on liquid jet impingement. These cases are discussed next.

4.2.1. Stevens and Webb

The first test case is the experiment performed by Steven and Webb, and is already discussed in detail in Chapter 2. The goal of the research was to determine the effects of Reynolds number, nozzle diameter and target distance on the Nusselt number. The researchers present three correlations: two for the stagnation zone Nusselt number and one for the local Nusselt number. These correlations are presented before, as Eq. (2.22), Eq. (2.23) and Eq. (2.24). The experiment is performed with water as the working fluid, however a material dependency ($Pr^{0.4}$) is included in the correlations, making it possible to use the correlations for other fluids as well.

4.2.2. Nasif, Barron and Balachandar

The second test case is a CFD simulation performed to solve a piston cooling problem. The researchers investigated the effect of piston motion on the heat transfer, by simplifying the problem in a similar way as is done in the current project. Although they were interested in the effects of motion, they provided results for a stationary piston as well. These results are used for the validation. Their results for the Nusselt number are listed in Table 4.1. The researchers divided the target disc into several regions and determined the area-averaged Nusselt number for each region.

Table 4.1: Area-averaged Nusselt number results obtained by [17].

Section	Section range	Nusselt number
1	$0 < r/d < 1$	151.0
2	$1 < r/d < 3$	109.5
3	$3 < r/d < 6$	77.0
4	$6 < r/d < 10$	48.0
5	$10 < r/d < 15$	20.5
6	$15 < r/d < 20$	10.5

4.2.3. Ma, et al.

The third test case is the analytical study performed by Ma et al., which is also discussed in Chapter 2. The researchers divided the flow field after impingement into several regions as is depicted in Fig. 2.9. For each of these regions, they derived expressions for the boundary layer thickness and the Nusselt number.

4.3. CFD model

This section describes the CFD model developed in Star-CCM+ to analyse the heat transfer between the jet and the heated disc.

4.3.1. Computational domain

A schematic of the 2D – axisymmetric domain and corresponding boundary conditions are shown in Fig. 4.2 and Table 4.2. The dimensions of the domain are depending on the problem, since the length of the domain is determined by the nozzle-to-target distance and the height is determined by the target disc diameter. The length of the nozzle is not investigated, and is assumed to be equal to 5d for all simulations, for the same reasons as was the case for the LES simulation of the oil jet.

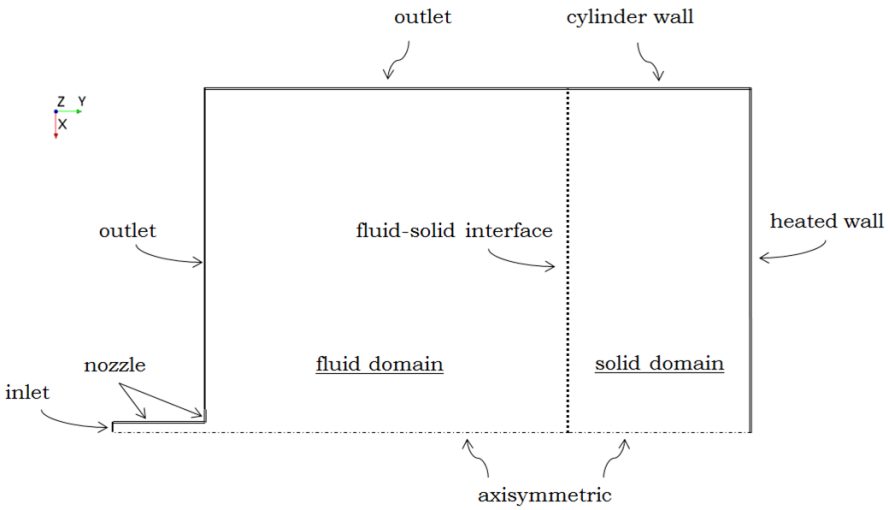

Figure 4.2: 2D schematic of the computational domain.

Table 4.2: (Thermal) boundary conditions for the simplified 2d-axisymmetric domain.

Boundary	Region	BC	Thermal BC
Inlet	Fluid	Velocity inlet	Constant T
Nozzle	Fluid	No-slip wall	Constant T
Outlet	Fluid	Pressure outlet	Constant T
Target	Fluid	No-slip wall + interface	CHT
Axisymmetric	Fluid	Axis	-
Target	Solid	Wall + interface	CHT
Cylinder wall	Solid	Wall	Adiabatic
Heated	Solid	Wall	Heat flux
Axisymmetric	Solid	Axis	-

4.3.2. Mesh

The domain presented in Fig. 4.2 can be split up into the fluid domain and the solid domain. The mesh for the fluid domain is needed to represent the jet on, and therefore needs more attention. Three important regions in the fluid domain can be distinguished: the jet region, the stagnation region and the wall region. Each of these regions are locally refined, to improve the representation of the flow on the mesh. The mesh size in each of these regions is a percentage of the base size. These percentages for the jet region, the stagnation region and the wall region are respectively 5%, 2.5% and 5% of the base size. The (polyhedral) mesh is shown in Fig. 4.3.

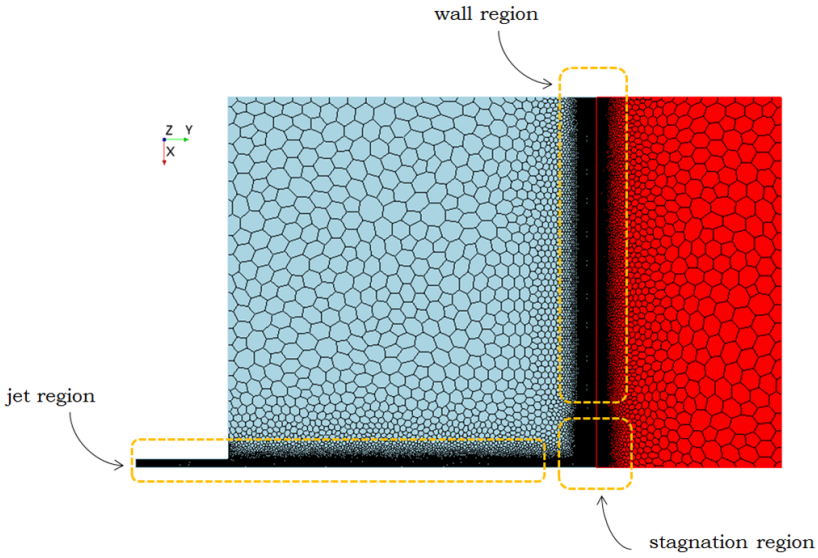

Figure 4.3: Example of the 2D mesh.

Before performing the mesh sensitivity study, there are some mesh requirements that need to be met. For heat transfer problems, the most important requirement is to keep the dimensionless wall distance y^+ below 1 such that the low y^+ wall treatment is activated, as was discussed in Chapter 2. Although the fine mesh needed for a low y^+ value increases the number of cells and thus the computation time, still its accuracy for near-wall flow is a desired feature and outweighs the increase of computation time. To make sure the dimensionless wall distance is indeed below 1, one can use prism layers. This is an easy way of designing and controlling the near-wall mesh. Besides this, it is a good way to represent boundary layers on a mesh. An example of the prism layers used can be seen in Fig. 4.4.

When designing the prism layers, one needs to make sure that the total thickness of the layers is large enough to capture the maximum boundary layer thickness. This value can be estimated by using Eq. (2.20) derived by [8] for liquid jets impinging onto a flat surface:

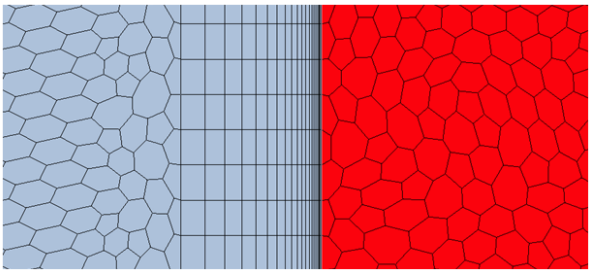

Figure 4.4: Example of prism layers (polyhedral grid).

$$\frac{\delta}{d} = \frac{5.147}{Re}\left(\frac{r}{d}\right)^2 + 0.17132\frac{d}{r}. \tag{4.1}$$

Further, it is important that the stretching of the layers is not too large [47], such that there are no large differences in mesh size for successive prism layers. This value is kept at 1.2 for all simulations. This smooth transition from layer to layer is also desired between the outer prism layer and the 'regular' mesh. The outer layer should be similar in thickness as the regular mesh size, such that also here there is a smooth transition in cell size.

The solid mesh requirements are less strict, since only conductive heat transfer takes place in part of the domain. One requirement is that the connection between the fluid and solid domain is conformal, as is shown in Fig. 4.4. The mesh size in the solid domain at the interface is thus equal to the solid mesh at the interface. In the remaining part of the solid domain the cell size increases to the base size.

4.3.3. Mesh sensitivity

To make sure that the results are not mesh dependent, a mesh sensitivity analysis is performed. This analysis is done by varying cell size, cell type and number of prism layers. The monitored output parameter is the Nusselt number distribution on the surface. The results of this study are only presented for the reproduction of test case 1.

The first test is by varying the mesh size. Since the mesh size in the refinement regions is a percentage of the base size, only the base size is varied. The prism layer settings are kept the same in this study. The tested base sizes are $1.25d$, $0.81d$, $0.52d$ and $0.32d$. The results for Nu are shown in Fig. 4.5, with the full distribution in the left figure and a close-up of the stagnation zone in the right figure.

It appears that the results are very similar and there is not much variation in Nusselt number distribution. The close-up for the stagnation region shows that the Nusselt number is clearly moving towards a certain 'limiting' distribution with decreasing mesh size. It can be seen that the largest deviations occur at $r/d = 0$, and these deviations are decreasing for larger r/d. The Nusselt number in the stagnation zone is determined by calculating the area-averaged Nusselt number for R/d between 0 and 0.787, as discussed in Chapter 2. When this is done for the results in Fig. 4.5, the differences are all below 2% for successive runs. It should be mentioned that the near-wall mesh (prism layers) is not changed in this study, which is most likely the reason for this 'insensitive' outcome. Since the monitored property is a measure of the heat transfer at the wall, these results make sense. The final mesh size is set at $0.5d$ based on these results.

The next step is to confirm this conclusion, by switching to a different mesh type (structured mesh) and again by keeping the prism layer settings the same. If the prism layer is in fact the dominant mesh region, then also the mesh type should not significantly affect the results for Nu. The same refinement strategy and base size are used for the structured mesh, which is shown in Fig. 4.6.

The results are shown in Fig. 4.7. It can be seen that there is large mismatch at $r/d = 0$ and the agreement becomes better as r/d increases. The trimmed mesh produces a slightly larger Nusselt number for $r/d < 0.1$ and a slightly lower Nusselt number for the remaining area of the stagnation zone. The area-averaged Nusselt

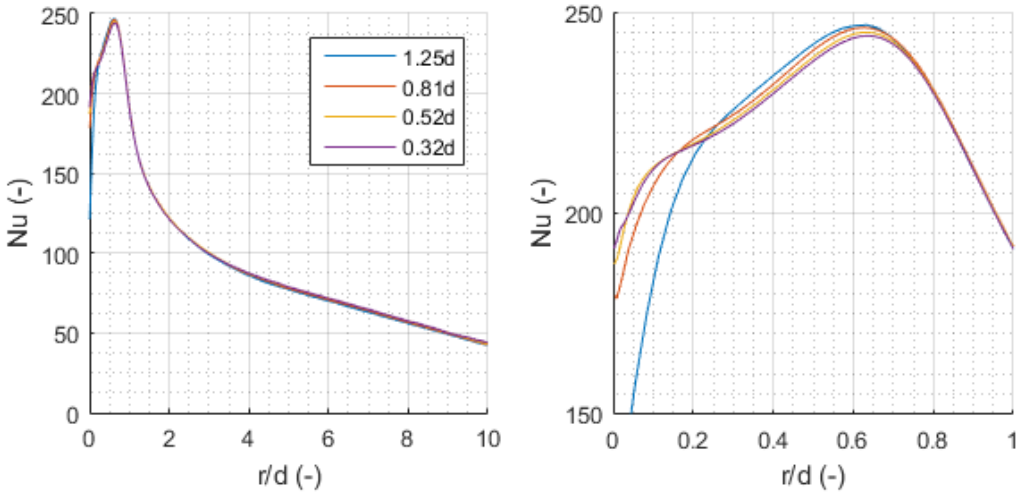

Figure 4.5: (Left) Results for Nu for different base size values. (Right) Close-up of the stagnation zone.

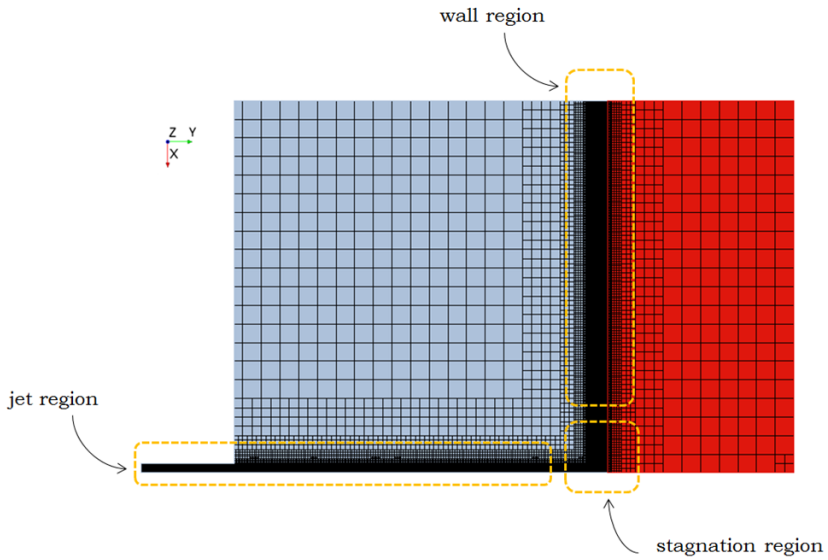

Figure 4.6: The structured mesh, with the same mesh settings as the polyhedral mesh.

numbers for the stagnation zone are 232 and 235, for respectively the trimmed mesh and the polyhedral mesh. This corresponds to a difference smaller than 2% and can be considered to be small enough to confirm the earlier conclusion: the dominant mesh region is the near-wall region, meshed with prism layers.

The final step is to investigate the effects of varying the wall y^+ value, by increasing the mesh density in the prism layers. The total prism layer thickness and the stretching factor are kept constant. The tested number of layers are 18, 20 and 25, resulting in a wall y^+ distribution on the surface as is shown in Fig. 4.8.

It can be seen that all three y^+ distributions are below 1, as this was one of the requirements for the near-wall mesh. The effect of these variations in y^+ on the Nusselt number is shown in Fig. 4.9. Small deviations can be observed in the stagnation region, however these are again small enough to neglect them ($< 2\%$). Based on these results, the final number of prism layers is chosen to be 20, and with this number of layers the results are considered to be independent of the mesh.

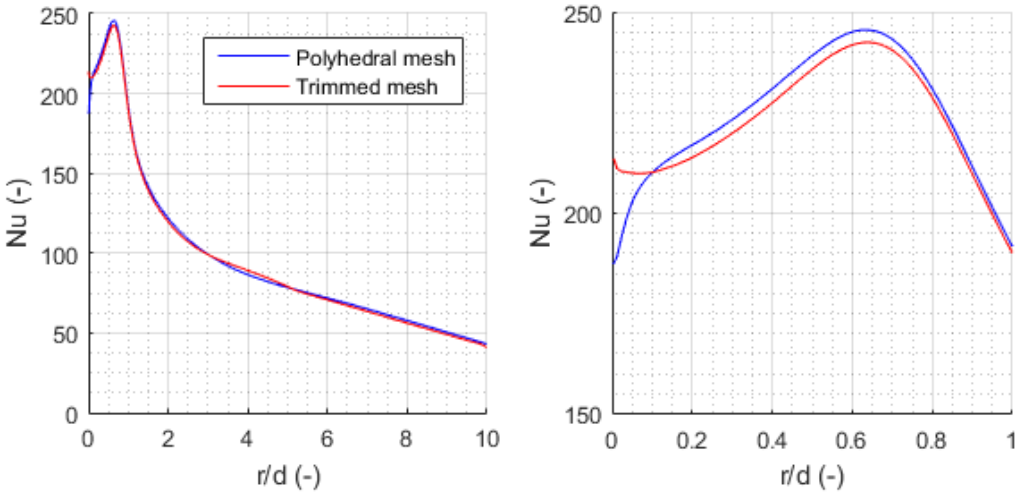

Figure 4.7: Results for Nu for a polyhedral and a trimmed mesh.

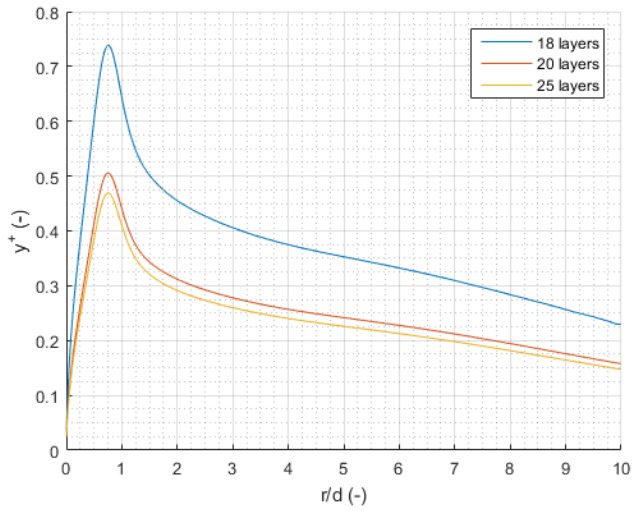

Figure 4.8: Results for y^+ for different number of prism layers.

4.3.4. VOF convection scheme

It was shown in the previous chapter that the first-order VOF convection scheme in combination with a polyhedral grid results in the introduction of serious numerical diffusion. The effects of a lower convection scheme order on the heat transfer are investigated next. The results for the Nusselt number are presented in Fig. 4.10. It can be seen that again the first-order scheme on a polyhedral grid results in a different outcome compared to the other tests. The maximum error on the target surface (outside the stagnation point) and the error in area-averaged Nu_0 is calculated and listed in Table 4.3.

The conclusion that can be drawn is the same as the conclusion drawn for the RANS simulation of the oil jet: the structured/first-order, the structured/second-order and the polyhedral/second-order combinations produce similar results (difference < 5%). The polyhedral/first-order combination results in the introduction of numerical diffusion and this is affecting the heat transfer results. This holds however for the local Nusselt number only. The area-averaged value of the Nusselt number in the stagnation zone is in good agreement with the other three runs (difference of 0.7%).

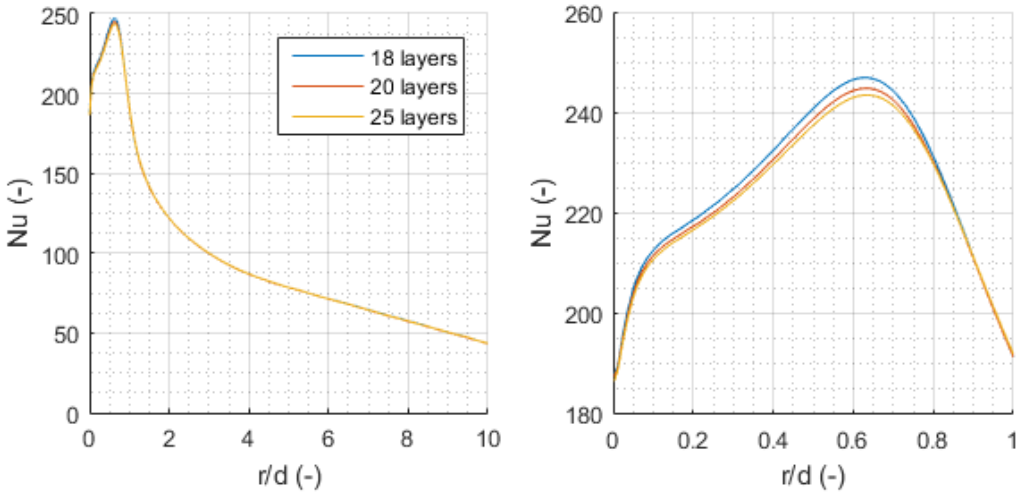

Figure 4.9: Results for Nu for different number of prism layers.

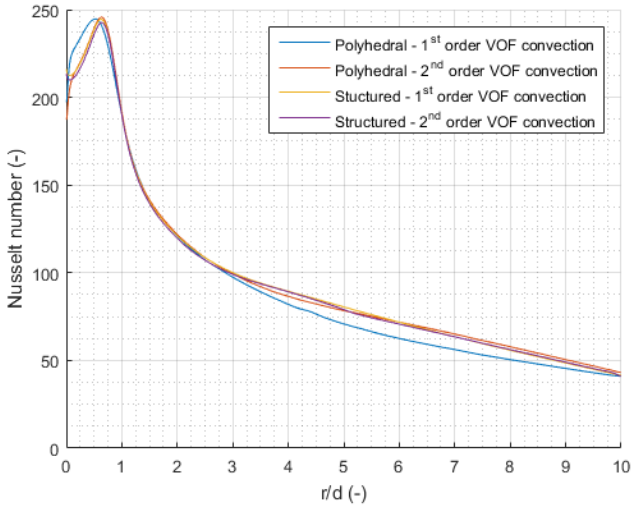

Figure 4.10: Results for different VOF convection schemes, for both the structured and polyhedral grids.

Table 4.3: Difference in Nu and area-averaged Nu_0 for different mesh types and VOF convection scheme orders, with respect to the results obtained for the polyhedral grid and the second-order VOF convection scheme.

	Polyhedral grid 1^{st} order	Structured grid 1^{st} order	Structured grid 2^{nd} order
Max error in Nu	13.7%	3.9%	4.7 %
Error in Nu_0	0.7%	0.3%	1.2%

4.3.5. 3D

The domain is simplified by using the axisymmetric property of the problem, such that there is a CFD model that is low in computational cost. The validity of this simplification is checked by comparing the results obtained in 2D-axisymmetric to results obtained for a 3D simulation. All mesh settings are kept exactly the same as described earlier for the 2D mesh. An example of the domain and the visualisation of the oil volume fraction can be seen in Fig. 4.11.

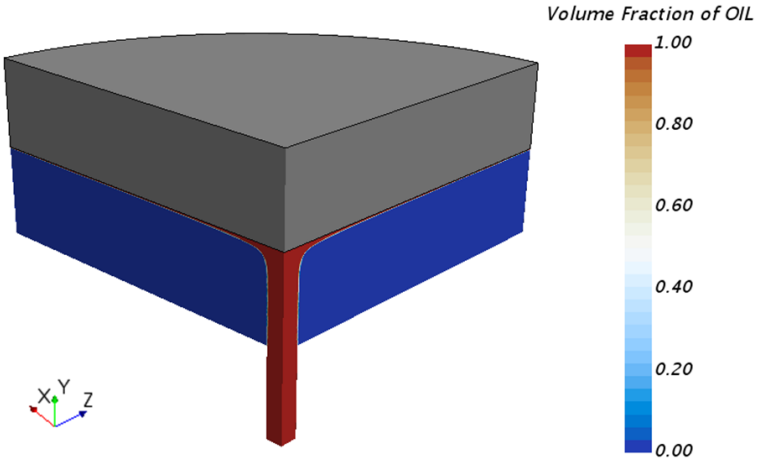

Figure 4.11: 3D domain, showing the flow field for the oil volume fraction.

For Nu_0 is was found that the difference with respect to the 2D results was smaller than 1%, and thus it can be concluded that the 2D results are in good agreement with the 3D results.

4.3.6. Physics models

Next, the physics models and CFD settings used for the investigation of the simplified 2D problem are discussed.

Spatial discretisation

The second-order scheme is used for all convection calculations. The gradients are calculated with the Hybrid Gauss-Least Squares Method. For a detailed description of these models the reader is referred to the Star-CCM+ User Guide [16].

Temporal discretisation

There is no unsteady behaviour of the flow in this simplified problem, therefore all simulations are performed as steady-state simulations.

Turbulence model

The goal is to accurately predict the heat transfer characteristics. It was mentioned in Section 2.4 that the k-ω SST model is a blending model, where the far-field qualities of the k-ϵ model and the near-wall qualities of the k-ω model are combined. This turbulence model is selected for all heat transfer calculations, and the effect of other turbulence models is not investigated.

Multiphase model

The multiphase interaction is modelled again with the VOF model. The EMP model was shown in the previous chapter to be extremely unstable for a relatively simple problem. Since in this chapter the wall modelling is included, it is expected that the EMP will become even more unstable and therefore not considered.

4.4. Results and validation

The presented CFD model is now used to reproduce the test cases. The third test case (by Ma, et al.) is not conducted for a specific operating condition and can be applied to different liquid jet impingement problems. Therefore their results will be included in the validation of the reproductions of test cases 1 and 2.

4.4.1. Stevens and Webb

This experiment is reproduced by simulating three different Reynolds numbers, such that besides the prediction of the Nusselt number, also the Reynolds number dependency of the Nusselt number can be tested. The important input parameters to the CFD model are presented in Table 4.4.

Table 4.4: Input parameters CFD model for the reproduction of test case 1.

Diameter	4.1 mm
Jet velocity	4.6 / 6.9 / 8.9 m/s
Reynolds number	21,200 / 31,800 / 40,800
Prandtl number	6
Target distance	2.5 d
Liquid	Water
Disc diameter	10 d
Disc thickness	10 mm
Heat flux	50 kW/m^2

Table 4.4 shows that the considered Reynolds numbers are clearly in the turbulent region. This is best represented by applying a fully developed turbulent profile as the inlet condition, obtained with the precursor simulation (explained in Appendix C). The results for the Nusselt number are presented in Fig. 4.12. It can be seen there is a clear Reynolds number effect, as the Nusselt number is basically shifting upwards with increasing Reynolds number.

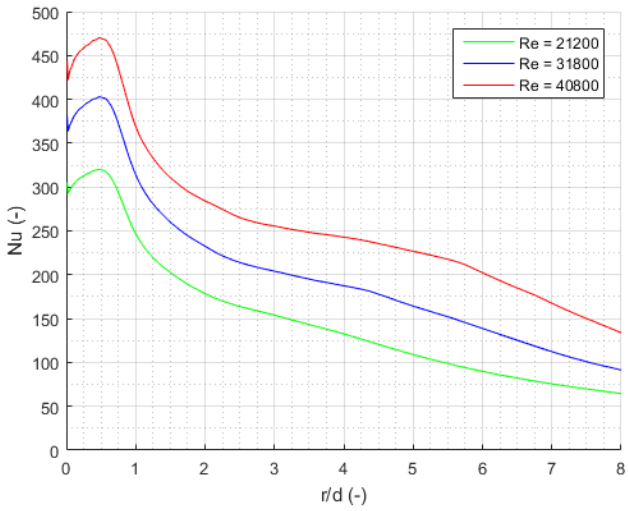

Figure 4.12: Results for Nu obtained with fully developed inlet conditions.

In order to assess the accuracy of these results, a comparison is made with the experimental results of Stevens and Webb and the analytical results of Ma, et al. To correctly compare the stagnation point Nusselt numbers, the area-averaged Nusselt numbers are again calculated first. This is shown in Fig. 4.13.

It is clear that there is an over-prediction of Nu_0 with respect to the test case results. The agreement is reasonable with Eq. (2.22) for the lowest tested Reynolds number, with a difference of 5%. However, for the larger Reynolds numbers, the over-prediction increases above 15%, which is too large to consider these results as

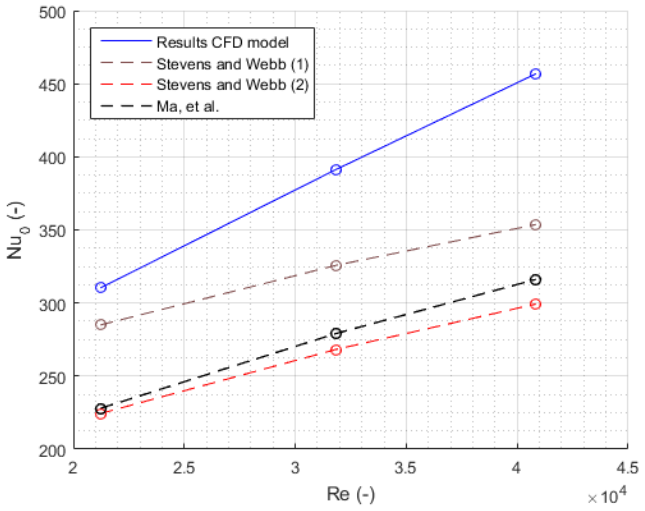

Figure 4.13: Comparison of area-averaged Nu_0 with the test case 1 and 2, for the fully developed inlet conditions.

acceptable. When the results are compared to Eq. (2.23) and the results of Ma, et al., these differences are even larger.

A possible reason for the over-prediction could be the fully developed turbulent inlet conditions. The simulation is therefore repeated with a less turbulent inlet condition. By applying a constant velocity profile at the inlet, the velocity profile at the nozzle exit can best be described as transitional flow. The turbulence specification is also decreased to the default values for the turbulence intensity and turbulent viscosity ratio at the inlet, respectively equal to 0.01 and 10. A comparison of the velocity profiles at the nozzle exit for the fully developed turbulent inlet profile and the constant inlet profile is shown in Fig. 4.14. It can be seen that the velocity profile at the nozzle exit is flatter and slightly lower than when a fully develop turbulent profile is used, and the expectation is that this will results in a lower prediction of the Nusselt number. The results for the Nusselt number and the area-averaged stagnation zone Nusselt number are presented in Fig. 4.15 and Fig. 4.16.

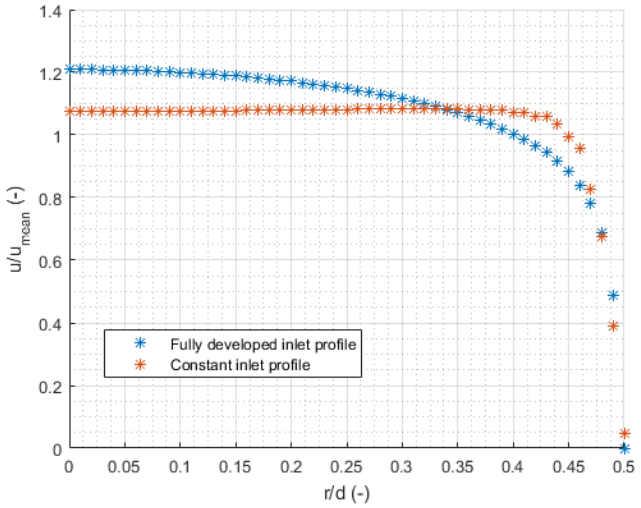

Figure 4.14: Comparison of velocity profile at nozzle exit for the fully developed turbulent inlet condition and the constant inlet condition.

It can be observed that with these less turbulent inlet conditions there is a much better agreement with the test case results. The best agreement is obtained for the second correlation of Stevens and Webb (Eq. (2.23))

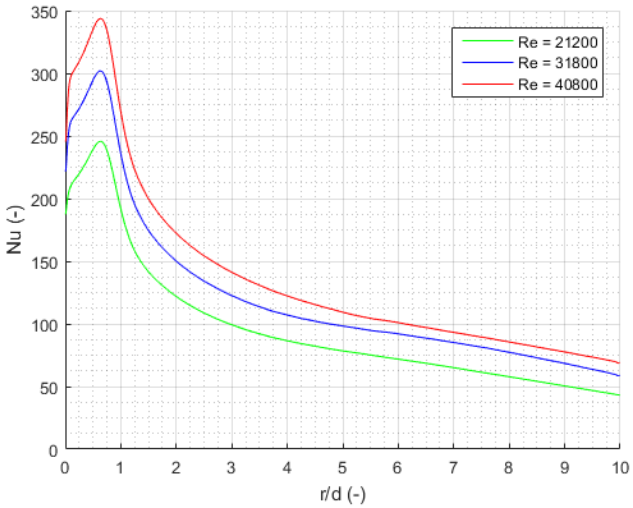

Figure 4.15: Results for Nu obtained with a constant inlet velocity profile.

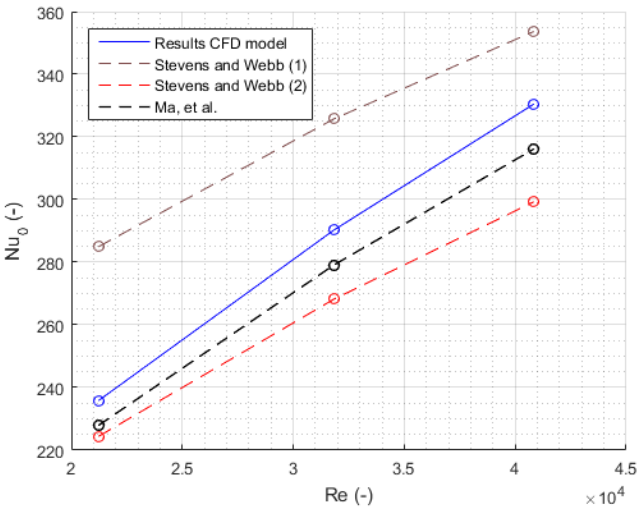

Figure 4.16: Comparison of area-averaged Nu_0 with the test case 1 and 2, for the constant inlet velocity profile.

and the analytical results of Ma, et al. The agreement with correlation one of Stevens and Webb (Eq. (2.22)) is less, as Nu_0 is under-predicted by 21.4% for the lowest tested Reynolds number. With increasing Reynolds number the agreement is improving: the difference is only 7.3% for the Re = 40,800 jet. Nevertheless, the CFD results remain nicely in between the two test case correlations.

Next, the local Nusselt number distribution is analysed. These results are shown in Fig. 4.17, Fig. 4.18 and Fig. 4.19. It can be seen that the agreement on the outer parts of the disc is not as good as was observed in the stagnation zone. For all three cases the correlations of Stevens and Webb decrease much faster than the CFD results, and are significantly lower for $r/d >$ 2-3. The reason for this outcome can be found by analysing how the researchers derived Eq. (2.24). This equation is obtained by fitting a curve through the experimental data points, as is shown in Fig. 4.20. It can be seen that this curve matches the data points in the stagnation zone only, and even for their own data it under-predicts Nu at larger radial distances. The r/d value above which the curve is under-predicting the Nusselt number is around r/d = 2-3, which is the same for the CFD results.

The local Nusselt number comparison with the results of Ma, et al. shows again the best agreement. The results are extremely good for the all tested Reynolds numbers, and this holds for the entire target surface.

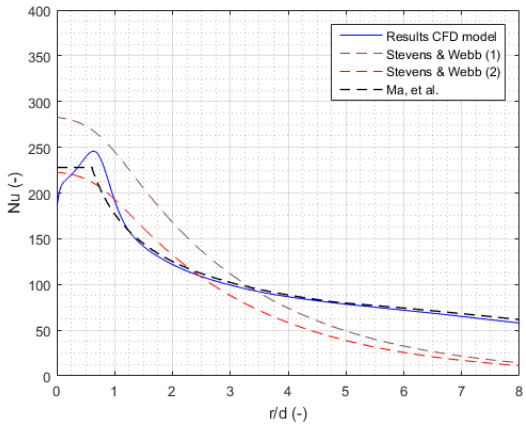

Figure 4.17: Comparison of local Nusselt number with test case results, for Re = 21,200.

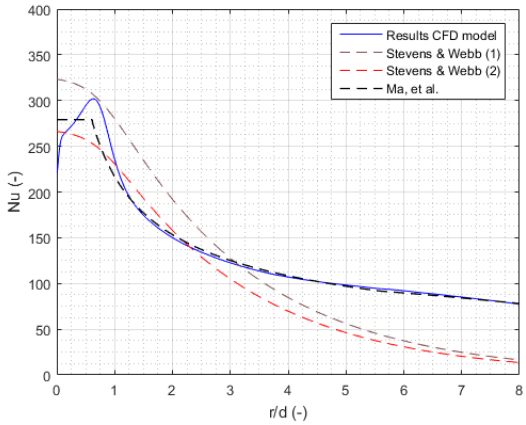

Figure 4.18: Comparison of local Nusselt number with test case results, for Re = 31,800.

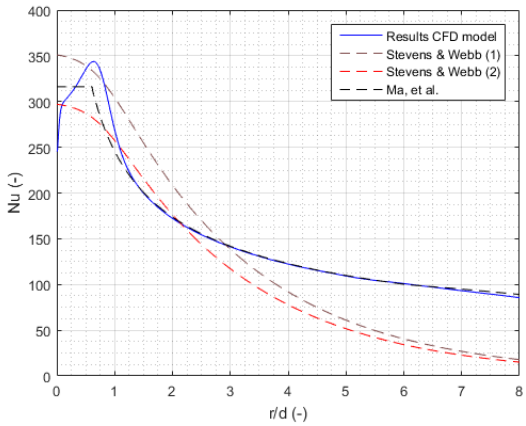

Figure 4.19: Comparison of local Nusselt number with test case results, for Re = 40,800.

The conclusion that can be drawn is that the experiment can be reproduced when constant inlet conditions are used. The most important region with jet impingement heat transfer is the stagnation zone, and it is shown that the CFD model can produce similar Nu_0 values as the experimental results. The best agreement is obtained with the analytical results of Ma, et al.

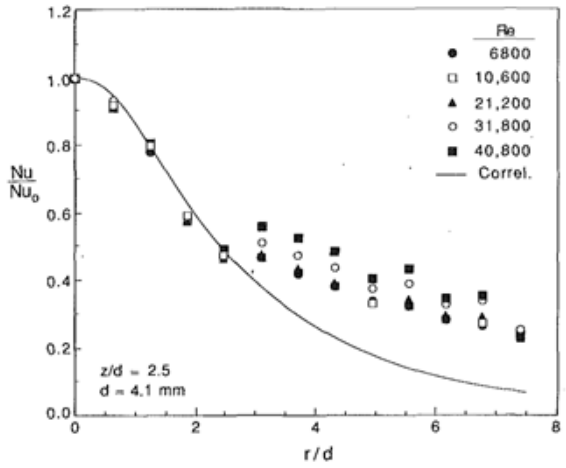

Figure 4.20: Data fitting by [9] for the determination of Eq. (2.24).

4.4.2. Nasif, Barron and Balachandar

The second test case is a numerical study, in which the aim was to determine the heat transfer between a heated the disc and an impinging oil jet. The authors presented the Nusselt number results as area-averaged values, and these are used for the comparison. Again the test case of Ma, et al. is included to the comparison of the results. The important input parameters to the CFD model are given in Table 4.5.

Table 4.5: Input parameters CFD model for the reproduction of test case 2.

Diameter	1.0 mm
Jet velocity	30 m/s
Reynolds number	3,000
Target distance	20 d
Liquid	Oil
Disc diameter	90 d
Disc thickness	10 mm
Heat flux	50 kW/m^2

Since the constant inlet conditions proved to perform better and the Reynolds number involved in this problem is lower than the critical Reynolds number (Re = 4,000), only the constant inlet conditions are used for this test case. Another important difference with respect to test case 1 is the diameter of the target disc, which is much larger for this case. Since the jet is an upward facing jet, a too large surface diameter would mean that the oil is not able to cover the entire surface and it will start to fall down because of gravity. The region covered by oil is then called the wetted area.

The velocity of the oil sheet on the surface can be estimated by Eq. (2.19) derived by Ma, et al.:

$$\frac{u_\infty}{V_0} = \frac{1}{25.735\left(\frac{r}{d}\right)^3 \frac{1}{Re} + 0.8566}.$$

The value for the Reynolds number is substituted and the resulting velocity profile is plotted in Fig. 4.21.

It can be seen that the correlation predicts that the velocity approaches zero between $r/d = 20-25$. Based on this prediction, it is expected that the oil sheet will detach from the surface in this region and fall down because of gravity. This is indeed confirmed by the CFD results. When the test case is reproduced, it is observed that the solver is clearly struggling to simulate the oil field for $r/d > 20$. The mesh is only refined near the wall, so when the flow detaches and enters the relatively coarse mesh, the numerical diffusion increases

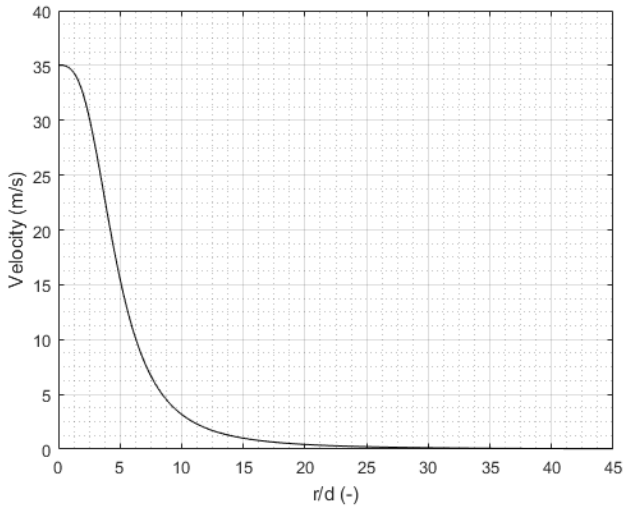

Figure 4.21: Prediction of the oil surface velocity for the test case 2, obtained with Eq. (2.19).

and this is causing convergence issues. The flow field is shown in Fig. 4.22, where the volume fraction of oil is highlighted. It can be seen that the oil detaches from the surface in the expected region, and the oil jet is not able to cover the entire disc surface.

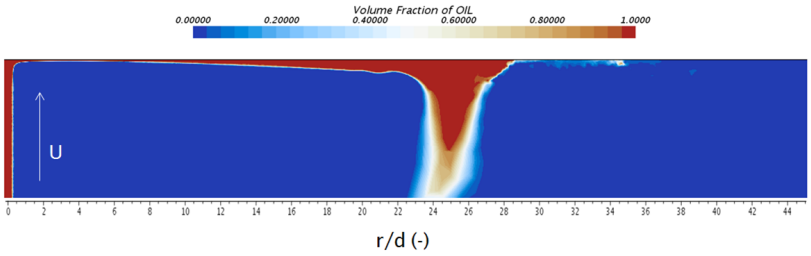

Figure 4.22: Flow field of the oil volume fraction, showing the detachment of the oil sheet.

The corresponding Nusselt number for the entire disc surface is shown in Fig. 4.23. The Nusselt number appears to be fine for $r/d < 20$. For larger radial distances the prediction is showing non-physical behaviour: it suddenly starts to increase, while it should be decreasing with increasing radial distance. This is most likely caused by the detachment of the oil from the surface. When the oil detaches from the surface, there is no more oil beyond this point and thus no more convective heat transfer. Therefore only the wetted area of the disc is considered in the following validation process.

The comparison of the CFD results to the test case results is shown in Fig. 4.24. The agreement with Ma, et al. is again very good for the entire surface. When the CFD results are compared to the results of Nasif, it can be seen that the prediction is completely off (by 70%) in the stagnation zone. Outside the stagnation zone the results show a better match. This observation can be explained by looking at the near-wall mesh used by Nasif. As was mentioned before, the low y^+ wall treatment results (theoretically) in the most accurate predictions for the convective heat transfer. The maximum y^+ distance used in the current CFD model is therefore below 1. In the test case however, the researchers mention that they keep the y^+ value below 3.5. To test if this is the cause of the serious differences in the stagnation zone, the simulation is repeated with an increased y^+ value. The result of this simulation is shown in Fig. 4.25.

It can be seen that the agreement in the stagnation zone has improved for the larger y^+ distance in the stagnation zone, however the Nusselt number distribution is not gradually decreasing along the disc surface now, which is most likely caused by the too high y^+ distance. The researchers of test case 2 performed the simulations in 3D and it can be concluded that they clearly chose a larger y^+ distance to decrease the number of

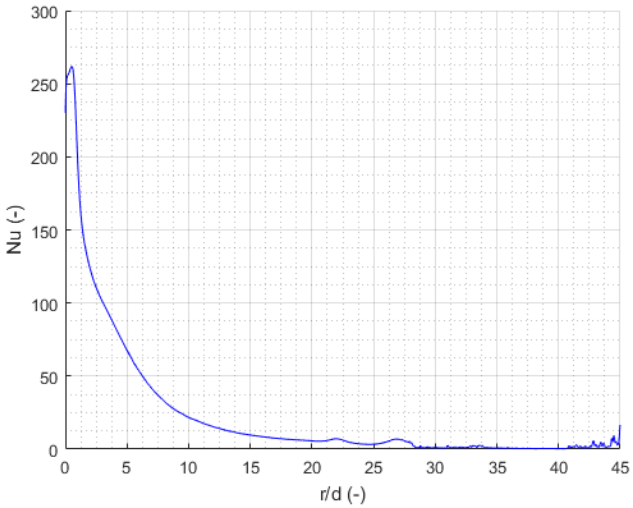

Figure 4.23: CFD results for the Nusselt number distribution (reproduction test case 2).

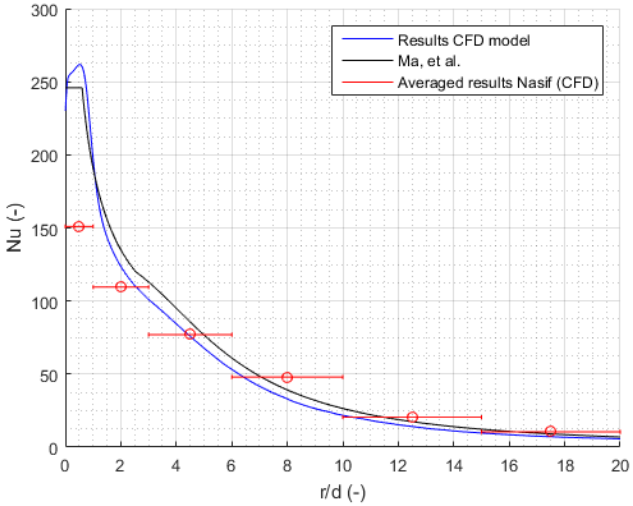

Figure 4.24: Comparison of CFD results for the Nusselt number distribution with the results of test case 2 and 3.

cells in the near-wall mesh and thus the computation time, and hereby accepted the losses in accuracy. The results obtained with the low y^+ can be considered as more reliable, and this is confirmed by the agreement with the results of Ma, et al.

4.5. Trend analysis

Now that the CFD model is validated with the selected test cases, it can be used to make predictions for the actual DAF operating conditions. By varying input parameters, the goal of this analysis is to find useful trends in the heat transfer. The analysis is similar to the trend analysis performed for the oil jet, in Chapter 3. The simplicity and low computation cost of the CFD model make it possible to extend the trend analysis by testing more parameters and more variations per parameter. The recorded output parameters will be the Nusselt number distribution on the disc surface and the resulting (steady state) temperature distributions on the heated/upper and cooled/lower surfaces of the disc. The test setup is presented in Table 4.6.

The target distance is kept constant for all performed trend analyses. It was shown in Chapter 3 that modelling

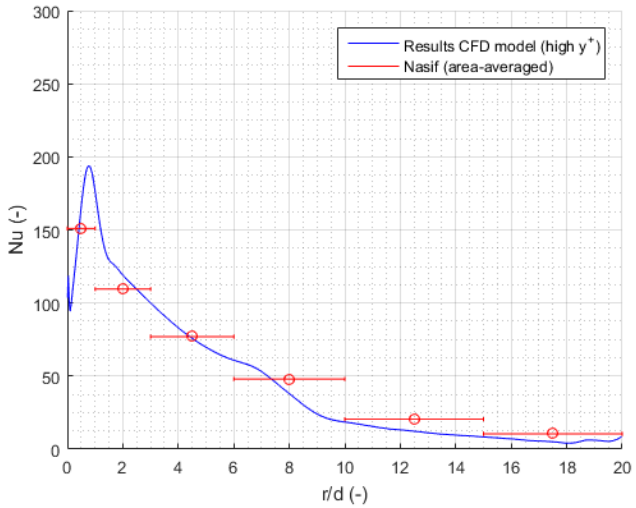

Figure 4.25: Comparison of CFD results for the Nusselt number (obtained with a high y^+) with the results of test case 2.

Table 4.6: Setup of the trend analysis of the DAF jets.

Input parameter	Tested range	Reference value
Flow rate (L/min)	[3, 5, 7, 9, 11, 13]	7
Temperature ($°C$)	[80, 90, 100, 110, 120]	100
Diameter (mm)	[2, 2.5, 3, 3.5, 4, 4.5]	3
Heat flux (kW/m^2)	[50, 150, 250, 350, 450]	250

the oil jet with RANS and VOF results in a straight beam-shaped jet, without any spreading behaviour. It is therefore expected that the target distance will not affect the outcome for the Nusselt number. This is tested by investigating the following (short) target distances: $5d$, $10d$, $15d$, $20d$ and $25d$ (for the reference nozzle diameter of 3 mm). The results for the stagnation zone Nusselt number are presented in Table 4.7. It can be seen that indeed the effect is extremely small (< 1%) for successive increments of the target distance. The final target distance is therefore set at $10d$ (for the 3 mm jet).

Table 4.7: Results for Nu_0 for different (short) target distances.

	$5d$	$10d$	$15d$	$20d$	$25d$
Nu_0	332	332	330	328	327

Finally, there is the disc thickness, which is also kept constant in this analysis. The reference value for the disc thickness is derived from the DAF piston geometry (shown in Fig. 1.3), and is set at 10 mm.

4.5.1. Flow rate effect

Again, the first tested parameter is the flow rate. The variations are again obtained by varying the velocity only, while keeping oil properties and nozzle diameter constant. The relevant problem parameters and their values are listed in Table 4.8.

First the results for the Nusselt number distribution are discussed, presented in Fig. 4.26. The results show a clear increase of the Nusselt number over the entire disc with increasing flow rate. This is in accordance with the expected Reynolds number effect, where the heat transfer increases with increasing Reynolds number. All tested flow rates result in a very similar shape/distribution, except for the 3 L/min case. For this flow rate, the shape in the stagnation zone and at the outer parts of the disc are clearly different than the other results. The stagnation zone shows a maximum in exactly the centre of the disc, whereas for the other plots this maximum is slightly downstream. The shape at the outer parts of the disc appears to be similar to what was observed in

Table 4.8: Input parameters to the CFD model for analysis of the flow rate effect.

Flow rate (L/min)	d (m)	v (m/s)	T ($°C$)	Re (−)	Pr (−)	L/d (−)
3	0.003	7.1	100	1,800	161	10d
5	0.003	11.8	100	3,000	161	10d
7	0.003	16.5	100	4,200	161	10d
9	0.003	21.2	100	5,400	161	10d
11	0.003	25.9	100	6,600	161	10d
13	0.003	30.6	100	7,800	161	10d

the reproduction of test case 2, where the oil velocity reaches zero and the flow detaches from the surface.

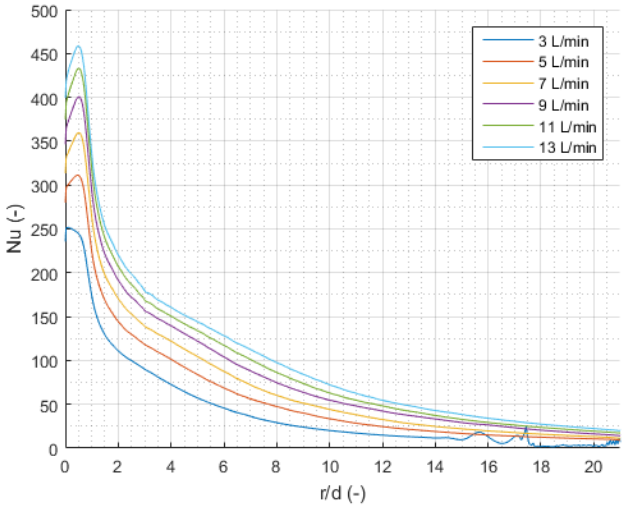

Figure 4.26: Effect of different flow rates on the Nusselt number distribution.

The difference in shape in the stagnation zone can be explained by analysing the gradient of the velocity field in the stagnation zone. This is shown for the 3 L/min and 11 L/min cases in Fig. 4.27. It can be seen that the acceleration of the oil near the wall is highest at different radial locations for the two cases. For the 3 L/min case this location is close to the centre and the maximum gradient of the velocity is relatively low. For the high flow rate case, this gradient is much larger and occurs at a radial position of $r/d = 0.5$, which is the location of the maximum Nusselt number. What is the exact reason for this difference in velocity gradient is not investigated.

For the odd behaviour at the outer part of the disc, again Eq. (2.19) can be used to estimate the radial velocity of the oil sheet. This is plotted in Fig. 4.28. It can be seen that the velocity approaches zero at around $r/d = 20$. In Fig. 4.29 the flow field for the 3 L/min case is visualised, where the detachment of the oil occurs at $r/d = 16-17$. It is clear from this figure that indeed the flow has detached from the surface and the conclusion is that the 3 L/min flow rate is not sufficient to cover the entire disc.

The accuracy of the Nusselt number predictions can be investigated by comparing the results to the correlations from the test cases. The comparison is only done for the area-averaged stagnation point Nusselt number, presented in Fig. 4.30.

The tested jets result in area-averaged Nu_0 values that are very similar to correlation 2 of Stevens and Webb. As the flow rate increases, the results start to deviate from this correlation and start to approach the correlation of Ma, et al. For the range of tested flow rates, Nu_0 remains nicely in between these two correlations. The deviations are largest when the results are compared to the first correlation of Stevens and Webb, most likely caused by the dimensional term v/d that is present in this correlation. To indicate the difference: the v/d tested in the experiment of Stevens and Webb was between $1.1{\cdot}10^3$ and $2.1{\cdot}10^3$, whereas this ratio in this analysis is between $2.4{\cdot}10^3$ and $1.0{\cdot}10^4$, for respectively the 3 L/min and 11 L/min flow rates. The v/d term

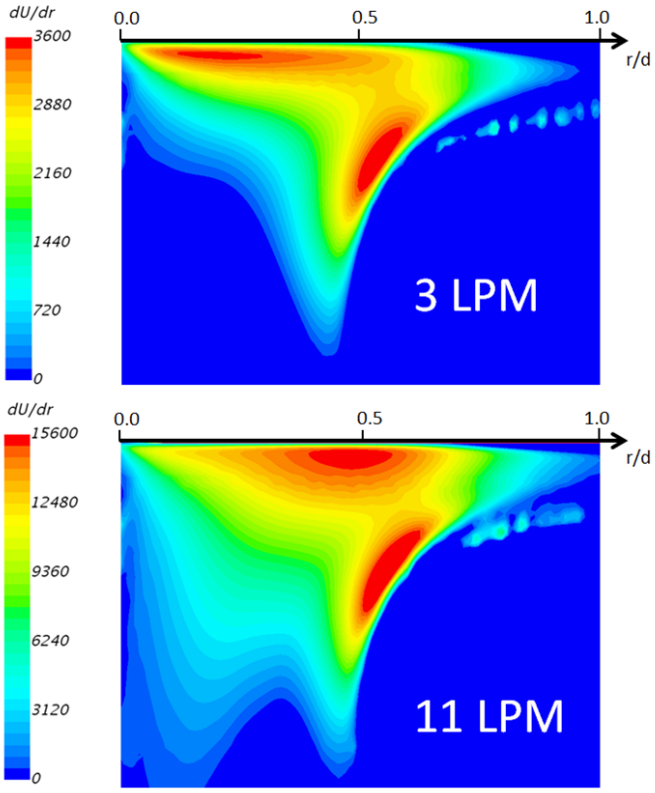

Figure 4.27: Comparison of the velocity gradient in radial direction for the 3 L/min and 11 L/min flow rates.

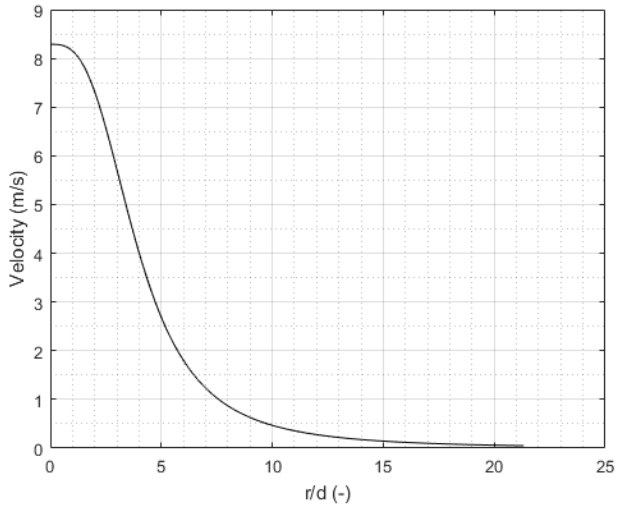

Figure 4.28: Prediction of the oil surface radial velocity for the 3 L/min jet, by using Eq. (2.19).

has a negative exponent in Eq. (2.22), and this means that for higher values, this should result in a decrease. This is exactly what is happening in Fig. 4.30 for the plot of correlation 1 of Stevens and Webb: it is decreasing faster than the other results, with increasing flow rate, thus with increasing v/d ratio.

Another interesting set of results is the results for the temperature distribution on the disc surfaces. The temperature distribution of the cooled and heated surfaces are presented in Fig. 4.31. It can be seen that the these results are a logical result of the Nusselt number results: the highest Nusselt numbers result in the lowest surface temperatures, for both the cooled and the heated disc surfaces.

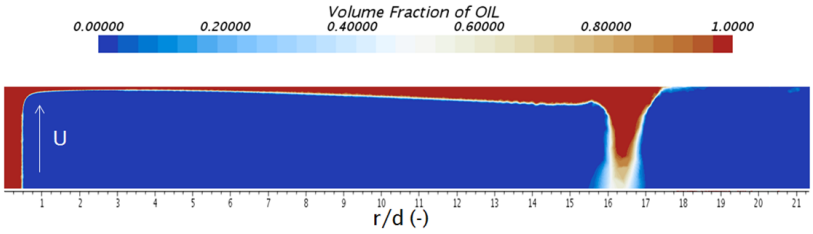

Figure 4.29: Flow field of the oil volume fraction for the 3 L/min jet, showing the detachment of the oil.

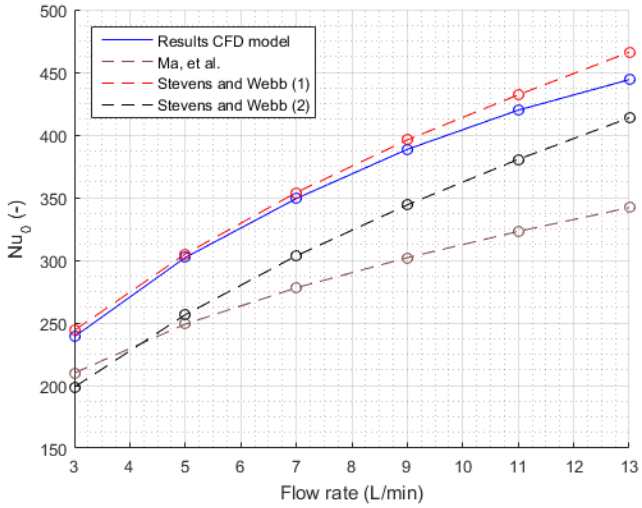

Figure 4.30: Comparison of area-averaged Nu_0 with the test case correlations for different flow rates.

Fig. 4.32 shows the area-averaged temperatures for the cooled and heated surfaces. It can be seen that the decrease of T_{avg} becomes smaller as the flow rates are increasing, indicating that T_{avg} is approaching a limit temperature when the flow rate is increased. This (theoretical) limiting case is when the flow rate is so high, that the temperature in the stagnation zone is equal to the oil temperature, because the heat transfer is highest here.

4.5.2. Temperature effect

The next analysis is done for variations in oil temperature. Changing the oil temperature result in changes in oil density, viscosity, specific heat and thermal conductivity, and these variations in turn result in changes in Reynolds number and Prandtl number, which are the determining parameters for the Nusselt number. The tested oil temperatures and resulting problem parameters are listed in Table 4.9.

Table 4.9: Input parameters to the CFD model for the analysis of the temperature effect.

Temperature (°C)	Flow rate (L/min)	d (m)	v (m/s)	Re (−)	Pr (−)	L/d (−)
80	7	0.003	16.5	2,600	258	10d
90	7	0.003	16.5	3,300	210	10d
100	7	0.003	16.5	4,200	161	10d
110	7	0.003	16.5	5,200	133	10d
120	7	0.003	16.5	6,300	110	10d

The tested range of Reynolds numbers are very similar to the tested range for the flow rate effect. The main difference now is that the Prandtl number is not constant anymore. The Reynolds number is increasing for higher temperatures, while the Prandtl number is decreasing. Since the Nusselt number has a positive de-

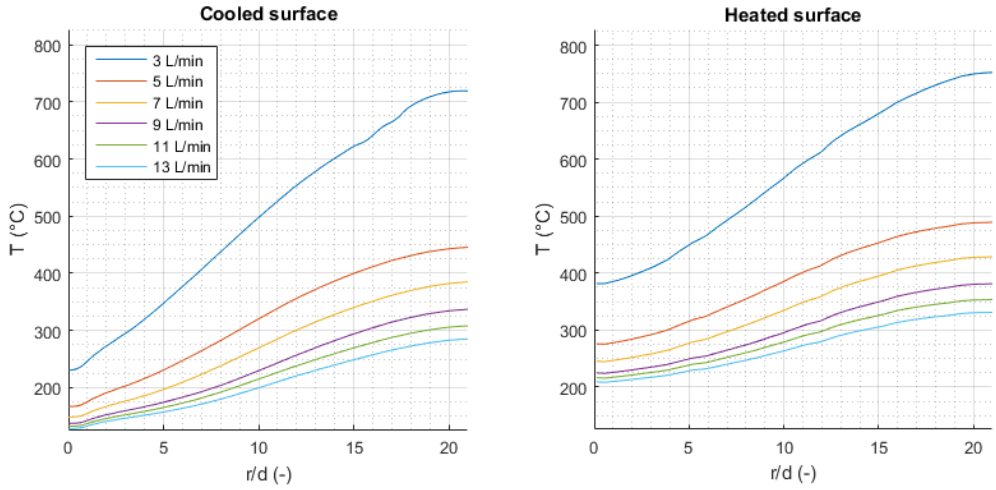

Figure 4.31: Results for the cooled and heated surface temperatures for different flow rates.

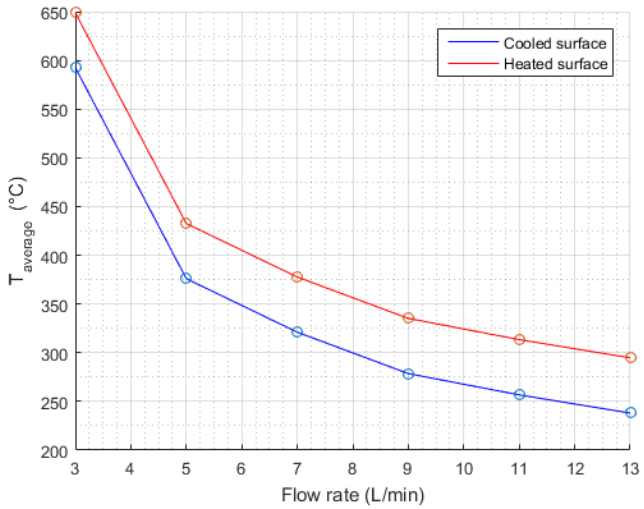

Figure 4.32: Area-averaged surface temperatures for the cooled and heated surfaces for different flow rates.

pendency on both of these numbers, it is interesting to investigate which of the two variations is dominant in the determination of the Nusselt number. The results for the Nusselt number produced for different oil temperatures are presented in Fig. 4.33.

There is a small increase (over the entire surface) with increasing oil temperature, meaning that the variations in Reynolds number are slightly more dominant than the variations in Prandtl number. The absolute increase is largest in the stagnation zone and this increase can be visualised in a better way by comparing the area-averaged Nu_0 values again. This is done in Fig. 4.34, with the predictions from literature included. It can be seen that there is a small linear increase as the oil temperature increases, as the difference between the Nu_avg for the lowest and highest temperatures is only 12%. The agreement with the test case results is again best with the second correlation of Stevens and Webb (Eq. (2.23)), whereas the slope of the line shows a better agreement with the other two correlations.

Since the Nusselt number is increasing for higher oil temperatures, this means that more heat is removed, and that the temperatures on the surface should be lower. Thus increasing the oil temperature results in

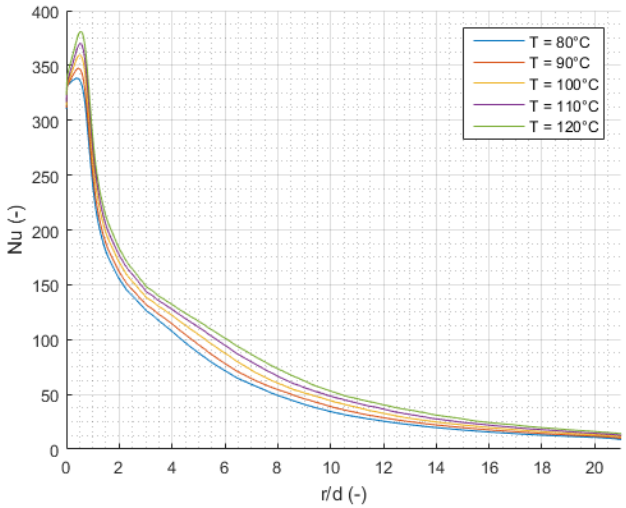

Figure 4.33: Effect of different oil temperatures on the Nusselt number distribution.

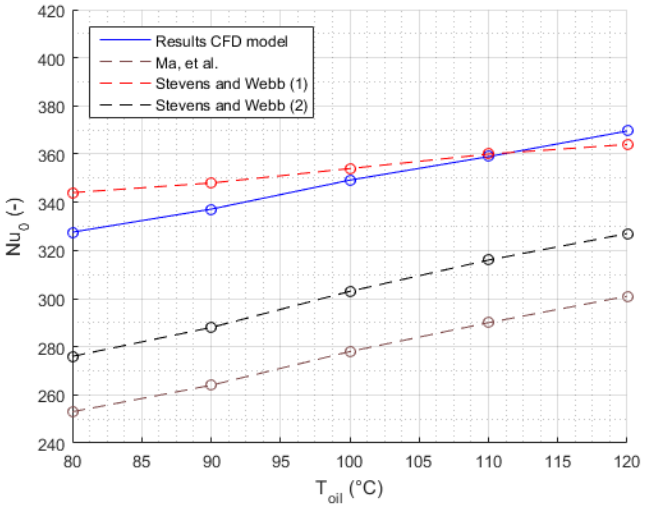

Figure 4.34: Comparison of area-averaged Nu_0 with the test case correlations for different oil temperatures.

lower disc temperatures, which is counter-intuitive outcome. If this is the case can be checked by plotting the surface temperatures again, shown in Fig. 4.35. It can be seen that indeed the expected trend is visible for the outer parts of the disc. In the centre of the disc, the opposite is observed, where the surface temperature is increasing with increasing oil temperature.

This outcome can be explained with the equations for convective heat transfer. The equations for the Nusselt number (Eq. (4.1)) and the convective heat transfer coefficient (Eq. (2.12)) can be combined to express the Nusselt number as a function of the temperature difference between the surface and the oil:

$$Nu = -\frac{d \cdot dT/dy}{T_s - T_\infty}. \tag{4.2}$$

It was mentioned that with increasing Nusselt numbers, more heat is removed and thus a lower surface temperature should be the result. This is only true when the oil temperature is kept constant. When the oil temperature is varied, this statement is false. It can be seen from Eq. (4.2) that with an increasing Nusselt number, it is not the surface temperature T_s that should decrease, but it is the term $T_s - T_\infty$ that needs to

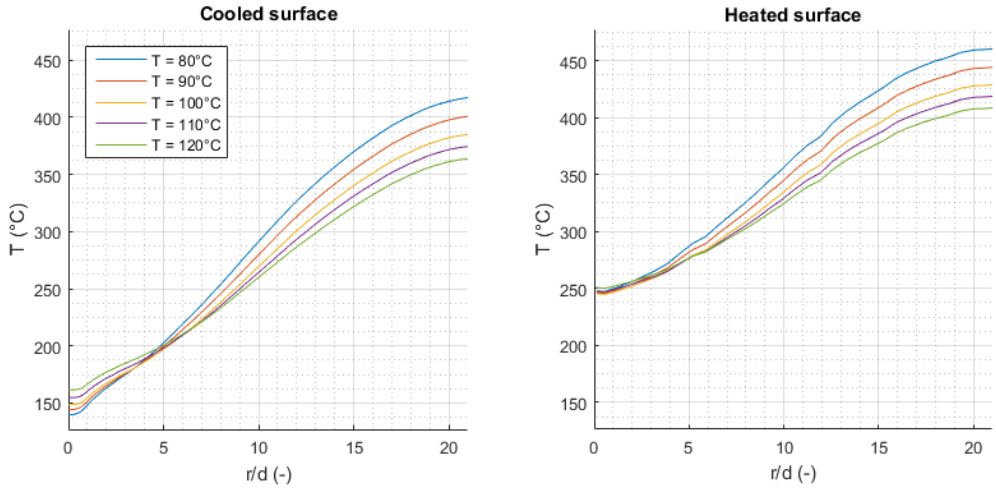

Figure 4.35: Results for the cooled and heated surface temperatures for different oil temperatures.

decrease. The results for T_s, T_∞ and $T_s - T_\infty$ in the centre of the disc are shown in Table 4.10. It can be seen that the temperature difference is indeed decreasing with increasing oil temperature. However, the variations of the oil temperature are 10 °C, whereas the decrease in the term $T_s - T_\infty$ is smaller than 10 °C, resulting in an increase of T_s in the centre of the disc.

Table 4.10: Comparison of variations for T_s, T_∞ and $T_s - T_\infty$, in the centre of the disc.

$T_{oil}(°C)$	$T_s(°C)$	$T_s - T_{oil}(°C)$
80	139	59
90	144	54
100	148	48
110	154	44
120	161	41

A simple example can help in gaining more insight into this: if the same increase in Nusselt number can be achieved (for a different - imaginary - fluid) with oil temperature variations of only 2 °C, the same table can be made, as can be seen in Table 4.11. The variations in Nusselt number are assumed to be the same as was obtained before, which means that the variations in the term $T_s - T_{oil}$ are also the same (assuming a similar boundary layer thickness). It can be seen that now the temperature difference decreases faster than the increase of oil temperature, resulting now in a decreasing surface temperature.

Table 4.11: Comparison of variations for T_s, T_∞ and $T_s - T_\infty$, for the example fluid and example Nusselt number increments.

$T_{oil}(°C)$	$T_s(°C)$	$T_s - T_{oil}(°C)$
96	155	59
98	152	54
100	148	48
102	146	44
104	145	41

Physically this outcome means that in the stagnation zone the heat transfer is so high, that the temperature difference between the oil and the surface becomes very small. When the oil temperature is then increased by 10 °C, the Nusselt number is slightly increasing and this results in a slightly smaller temperature difference between oil and surface. However, this decrease in temperature difference is not large enough to make up for the 10 °C increase of the oil temperature, and this results thus in an increasing surface temperature.

For the outer parts of the disc, it can be seen that the increase in Nusselt number is enough to make up for the 10 $°C$ increase of oil temperature. A table with the variations in temperatures and temperature differences is again shown in Table 4.12, for the radial position $r/d = 10$. It can be seen that the decrease of the temperature difference is indeed larger than the 10 $°C$ increase of oil temperature. The reason the difference being higher at the outer parts of the disc is related to the relative increase of the Nusselt number when the oil temperature is varied. The relative change of Nusselt numbers is higher at outer parts of the disc than in the centre.

Table 4.12: Comparison of variations for T_s, T_∞ and $T_s - T_\infty$, at $r/d = 10$.

$T_{oil}(°C)$	$T_s(°C)$	$T_s - T_{oil}(°C)$
80	291	211
90	279	189
100	269	169
110	264	154
120	260	140

The area-averaged temperature of both surfaces are compared in Fig. 4.36, and the effect of temperature variations is clearly visible. It can be concluded that these findings are very counter-intuitive, showing that lower surface temperatures can be obtained by increasing the temperature of the oil. The reaons are the increasing cooling capabilities of the fluid with increasing temperatures.

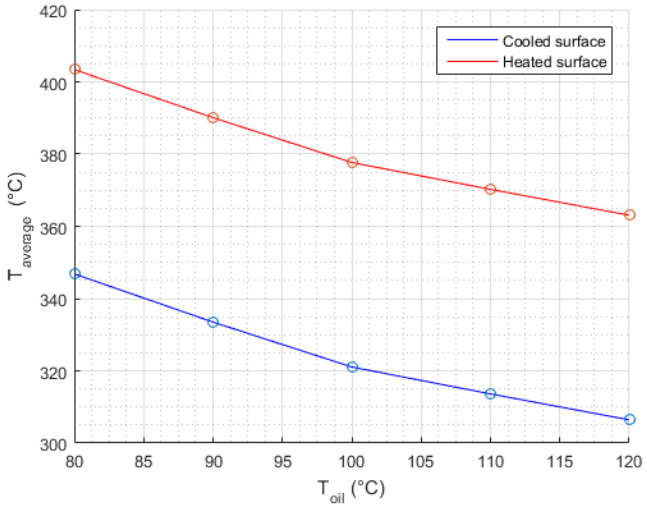

Figure 4.36: Area-averaged surface temperatures for the cooled and heated surfaces for different oil temperatures.

4.5.3. Diameter effect

The third effect is obtained for variations in nozzle diameter, as was done for the isolated oil jet as well. The diameter effect is tested by keeping the flow rate and the absolute target distance constant, meaning that L/d is not constant anymore. The velocity needs to be varied to keep the flow rate constant. The problem parameters are presented in Table 4.13.

It can be seen from the table that the Reynolds number decreases with decreasing diameter. The range of tested Reynolds numbers are similar to the range in the analysis of the flow rate effect. Further, it can be seen that L/d is decreasing as well, though the successive decreases become smaller for increasing diameters. Again, first the Nusselt number results are presented, shown in Fig. 4.37.

The first thing that can be noticed is that the shape of the Nusselt number is similar for all tested nozzle diameters, and the differences are clearly caused by the varying Reynolds number, as was the case for the flow rate effect. However, from these plots the actual effect of varying the diameter cannot be obtained. Therefore

Table 4.13: Input parameters to the CFD model for the analysis of the nozzle diameter effect.

d (m)	Flow rate (L/min)	v (m/s)	T ($°C$)	Re (−)	Pr (−)	L/d (−)
0.002	7	37.1	100	6,300	161	15
0.0025	7	23.8	100	5,100	161	12
0.003	7	16.5	100	4,200	161	10
0.0035	7	12.1	100	3,600	161	8.6
0.004	7	9.3	100	3,200	161	7.5
0.0045	7	7.3	100	2,800	161	6.67

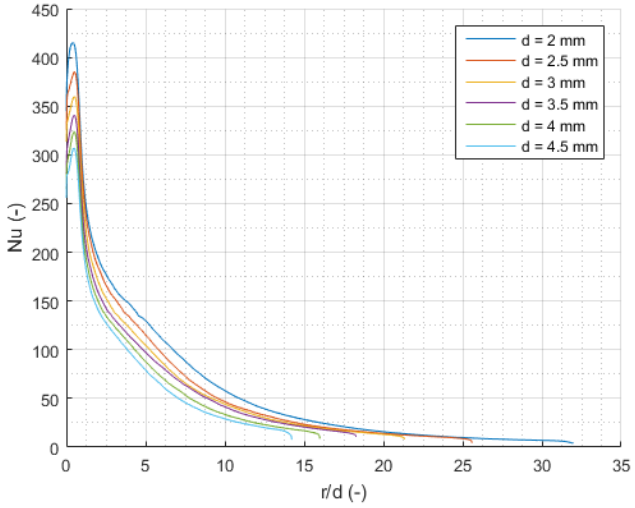

Figure 4.37: Effect of different nozzle diameters on the Nusselt number distribution, plotted versus r/d.

the results are now plotted versus the dimensional radial distance r, in Fig. 4.38. These plots can be seen as a scaled version (in radial direction) of the plots in Fig. 4.37, with the jet diameter d as the scaling factor.

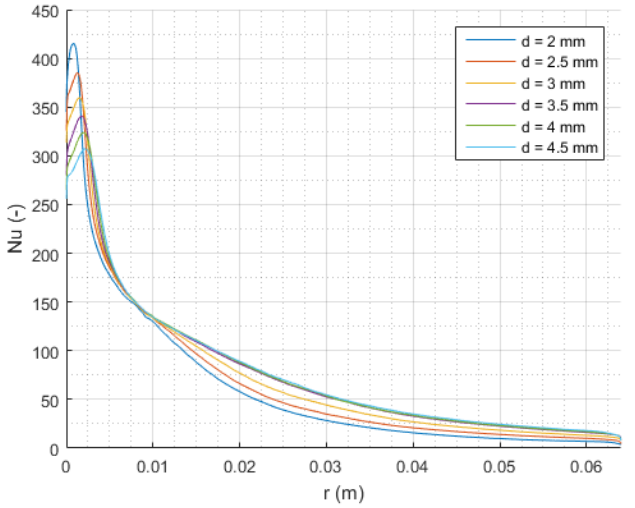

Figure 4.38: Effect of different nozzle diameters on the Nusselt number distribution, plotted versus r.

It can be seen that the earlier observed similarity in shape is now totally lost. Two different trends can be observed: the Nusselt numbers in the stagnation zone are dominated by the Reynolds number effect, as these are decreasing because of the decreasing velocities (and increasing diameters). For $r > 0.008m$ however, the dominant parameter is the jet diameter, and an increase in Nusselt number can be observed with increasing

diameter. Further, it can be seen that the differences in Nusselt number are much larger between d = 2.0, 2.5, 3.0 and 3.5 mm then the difference between d = 3.5, 4.0 and 4.5 mm.

It can be helpful in understanding these results to list the non-dimensional target diameters (D/d) for the different tested jet diameters. This is done in Table 4.14. It can be seen that again the successive decreases become smaller as the diameter increases. This means that the relative change in diameter becomes less, as the diameter is varied with a fixed value (0.5 mm per variation).

The main conclusion from these results is that the jets behave very similarly when plotted versus the non-dimensional radial distance r/d, however when they are plotted versus the absolute radial distance, the effect of the scaling results in different shapes. The values of the Nusselt number in the centre of the disc are dominated by the Reynolds number of the jet, which is highest for the lowest diameter. As the target diameter D is (relatively) much larger for this jet than it is for a larger jet diameter, the heat transfer quickly drops as the jet moves along the surface. With increasing diameter, the cooling capabilities of the jet are extended to a larger fraction of the target, resulting in higher Nusselt numbers at the outer parts of the disc. This effect is referred to as the diameter effect. Finally, it is observed that this effect becomes smaller and smaller, when the diameters are increased, as the relative variations in jet diameter become smaller (because of the fixed variation of 0.5 mm).

Table 4.14: Effect of diameter variations of the non-dimensional target diameter D/d.

d (m)	Flow rate (L/min)	v (m/s)	Re (−)	D/d (−)
0.002	7	37.1	6,300	32.0
0.0025	7	23.8	5,100	25.6
0.003	7	16.5	4,200	21.3
0.0035	7	12.1	3,600	18.3
0.004	7	9.3	3,200	16.0
0.0045	7	7.3	2,800	14.2

The accuracy of these results is again assessed by comparing the area-averaged Nu_0 values to the test case correlations. This comparison is shown in Fig. 4.39. The first thing that can observed is that one of the test case correlations is showing an increasing trend, whereas the other two correlations are showing a decreasing effect. This deviating behaviour is again observed for the first correlation of Stevens and Webb (Eq. (2.22)), which contains the dimensional term v/d. Since the only parameters that are varied in this investigation are v and d, the term v/d is dominating the outcome of Eq. (2.22) and is thus neglected in this comparison. The comparison to the other two correlations again show a very good agreement.

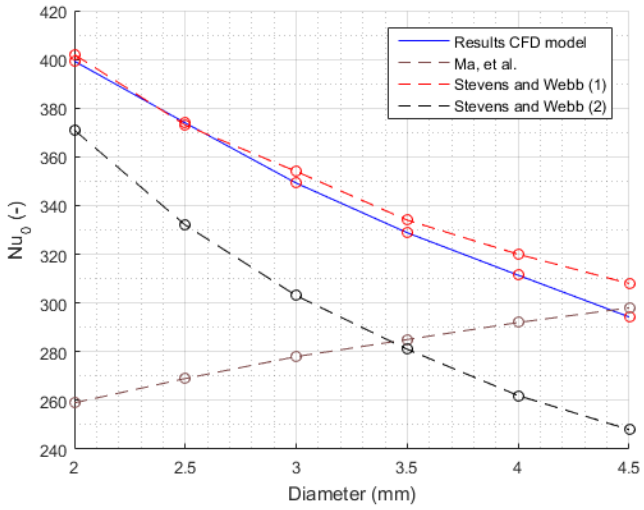

Figure 4.39: Comparison of area-averaged Nu_0 with the test case correlations for different nozzle diameters.

Next, the resulting steady-state temperature distributions are shown in Fig. 4.40. It can be seen that the re-

sulting temperature distributions look quite complicated, since there appears to be no clear/logical trend anymore. A closer look shows that there are in fact two trend present in these figures: one for the diameters between d = 2.0, 2.5, 3.0 and 3.5 mm and another trend for the diameters between d = 3.5, 4.0 and 4.5 mm. These trends can be better visualised by plotting them separately, as is done in Fig. 4.41 and Fig. 4.42.

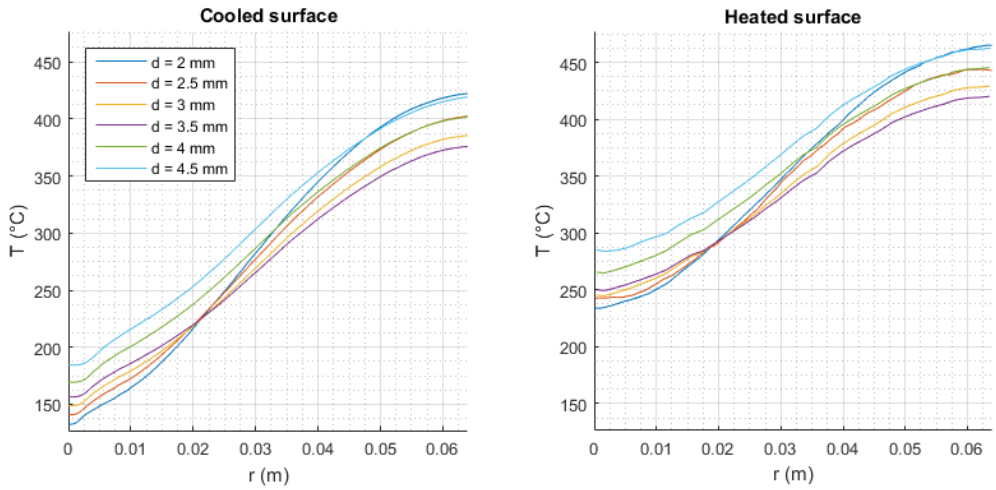

Figure 4.40: Results for the cooled and heated surface temperatures for different nozzle diameters.

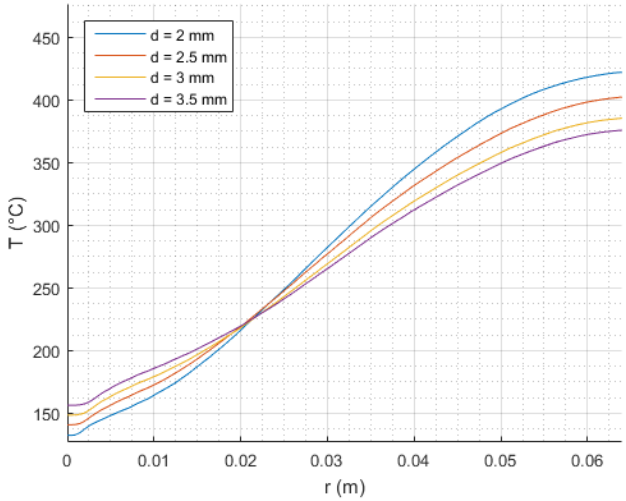

Figure 4.41: Results for the cooled surface temperatures for d = 2.0, 2.5, 3.0 and 3.5 mm

Fig. 4.41 is relatively straightforward, and can be seen as a direct consequence of the Nusselt number results. Higher Nusselt numbers in the centre result in lower temperatures, and lower Nusselt number values on the outer parts of the disc results in higher surface temperatures. This is caused by the diameter effect, as explained before.

In Fig. 4.42 something else is going on. It can be seen that there is no more intersection of the results and the temperature plots are just shifting up with increasing diameter. It appears that above d = 3.5 mm, there is no more diameter dependency and the outcome is purely a results of the changes in Reynolds number. It was already observed in the Nusselt number plots in Fig. 4.38 that the differences were extremely small at the outer parts of the disc, and this is also observed in the results for the temperature. Since there is a higher heat removal in the centre, this is causing the shift. If the heat transfer in the centre would be the same, there

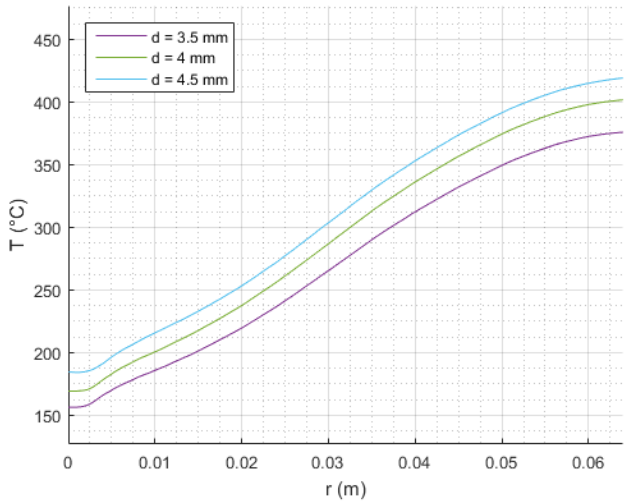

Figure 4.42: Results for the cooled surface temperatures for d = 3.5, 4.0 and 4.5 mm.

would most likely not be a shift in temperatures. It can thus be said that these jet cover the surface in a similar manner, and that there is no diameter effect for jet diameters above 3.5 mm.

Another nice way of visualising the effect of diameter variations is by plotting the area-averaged temperatures for both surfaces. This is shown in Fig. 4.43. An interesting outcome is observed, as there appears to be an optimal diameter for cooling the disc. It was shown that for diameters below d = 3.5 mm there is a diameter effect, increasing the heat removal at outer parts of the disc and thus decreasing the temperatures here. For diameters above d = 3.5 mm it was shown that this diameter effect was not (as strongly) present anymore, since these jets cover the surface in a similar manner and the largest difference in heat transfer take place in the stagnation zone, which is decreasing with increasing diameter.

It should be mentioned that this outcome depends on the diameter of the disc. For a larger disc diameter, the optimal jet diameter would increase, as the relative differences in D/d will increase, meaning that the diameter effect will be present at larger jet diameters.

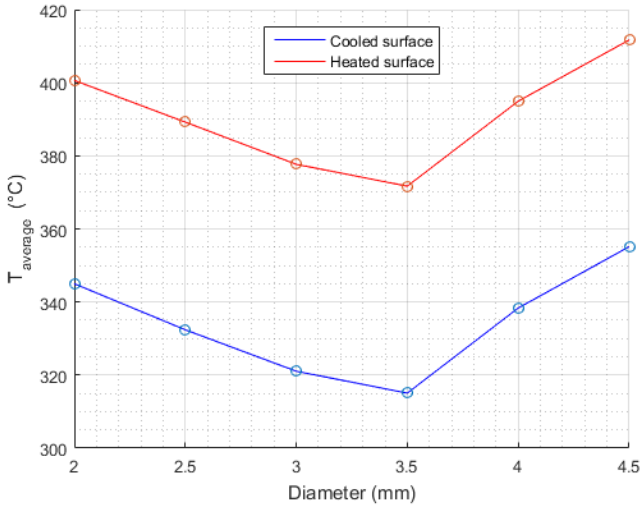

Figure 4.43: Area-averaged surface temperatures for the cooled and heated surfaces for different nozzle diameters.

4.5.4. Heat flux effect

The final trend analysis is performed for the heat flux that is applied to the top surface of the disc. It is expected that only the temperatures are affected by these variations. The determination of the reference value for the heat flux is explained in Appendix D. The tested fluxes are shown in Table 4.15

Table 4.15: Input parameters to the CFD model for the analysis of the heat flux effect.

Heat flux (kW/m^2)	Flow rate (L/min)	Re (−)	Pr (−)	L/d (−)
50	7	4,200	161	10d
150	7	4,200	161	10d
250	7	4,200	161	10d
350	7	4,200	161	10d
450	7	4,200	161	10d

The results for the Nusselt number are shown in Fig. 4.44. As was expected, there are no serious differences visible for the Nusselt number. The Nusselt number shows a small increase in the stagnation zone with increasing heat flux, however the largest difference is smaller than 2% and these differences can be neglected.

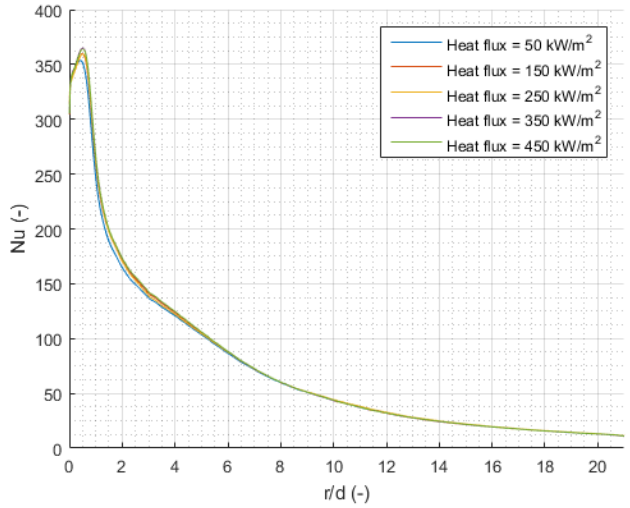

Figure 4.44: Effect of different heat fluxes on the Nusselt number distribution.

The corresponding temperature plots are shown in Fig. 4.45. It can be seen that there is clear trend visible. The temperatures on both surfaces increase with increasing heat flux. It is also interesting to see that for the lowest heat flux, the slope of the temperature plots is very small, resulting in a low temperature gradient along r/d.

The final figure is the comparison of the area-averaged temperature for both surfaces. It can be seen that there is a linear increase with increasing heat flux, which is not surprising since the Nusselt number is not changing and the heat input is varied.

4.6. Conclusions

The second sub-project was on the development of a simple, fast and reliable CFD model to analyse impingement heat transfer characteristics. This is done by making several simplifications to the spray cooling technique, such that reliable test cases can be used to develop and validate the CFD model. The main conclusions are repeated next:

- The experiment of Stevens and Webb was successfully reproduced by using a constant velocity profile

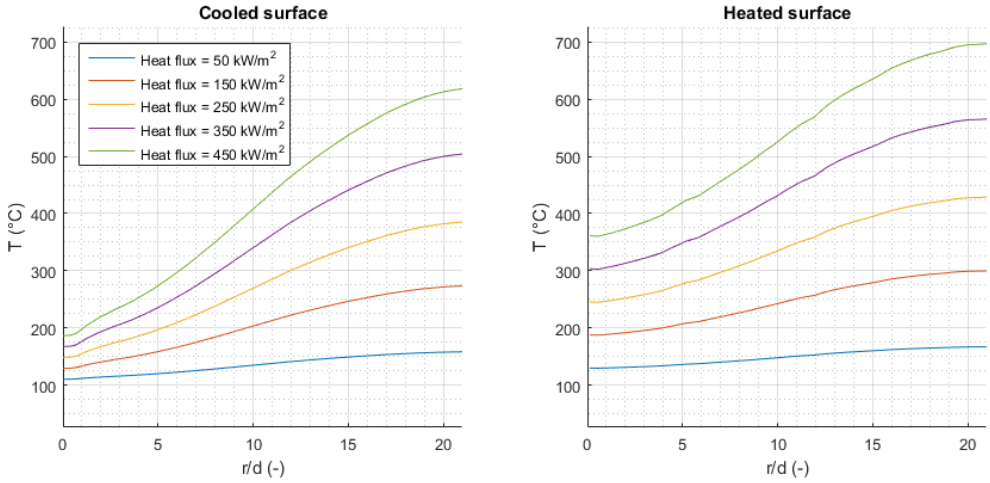

Figure 4.45: Results for the cooled and heated surface temperatures for different heat fluxes.

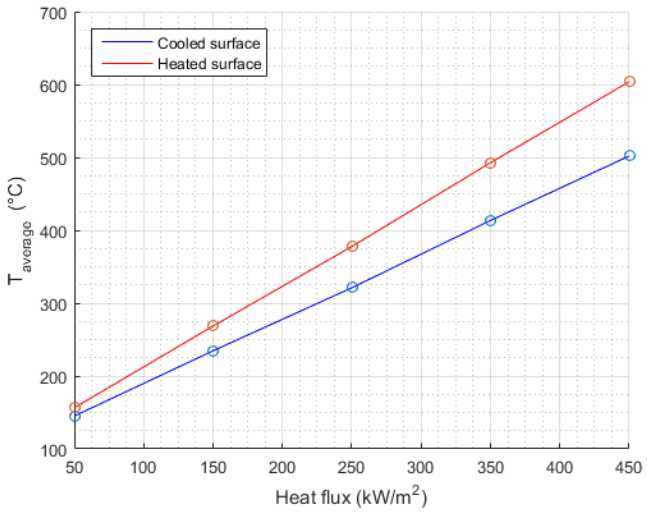

Figure 4.46: Area-averaged surface temperatures for the cooled and heated surfaces for different heat fluxes.

as the inlet conditions. The fully developed turbulent inlet conditions resulted in an over-prediction of the Nusselt number.

- The reproduction of the numerical study of Nasif, Barron and Balachandar resulted in a mismatch in the stagnation zone, and a good agreement for the remaining part of the target disc. It was shown that these differences were caused by the (less accurate) higher y^+ value used in the test case.
- Since the third test case of Ma, et al. was not derived for a specific operating condition, their results were compared to the reproduction results of the previous two test cases. It was shown that the best agreement, for the entire target surface, was obtained with this test case.
- The trend analysis for the flow rate effect resulted in an increasing heat transfer on the entire disc surface for increasing flow rates. The resulting steady-state temperatures showed a logical consequence of the Nusselt number results: decreasing temperatures with increasing flow rates.
- The analysis on the temperature effect resulted in a surprising (though logical) outcome: lower surface temperature can be obtained with higher oil temperatures. The reason for this outcome is that with

increasing temperatures, the cooling capabilities of the fluid is increased, resulting in a fluid with a higher cooling capability.

- The analysis for the diameter proved to be the most complex one. It was observed that, especially for the smaller tested diameters, there was a clear diameter effect. This can be explained as the effect of diameter variations on the outer parts of the disc. It was observed that with increasing diameters, higher Nusselt numbers can be obtained on the outer parts of the disc. For the temperature results this diameter effect was eliminated for jet diameters above 3.5 mm, as the differences in D/d for these jets become small. The optimal jet diameter resulting in the lowest T_{avg} was shown to be the 3.5 mm jet.
- The heat flux effect was shown to slightly affect the Nusselt numbers (< 2%), since flow properties are not varied in this analysis. Increasing the heat flux resulted in serious increases of temperatures on both surfaces.

5

Spray cooling

The final sub-project considered in this thesis is on the analysis of the spray cooling technique. This analysis can be seen as an extended version of the simplified disc problem, analysed in the previous chapter. It was mentioned that this model is obtained by making several simplifications to the spray cooling problem. The goal is now to undo these simplifications and analyse a more realistic situation. The following simplifications are considered:

- Effect of confinement by the cylinder
- Effect of the impingement location
- Effect of a more accurate representation of the piston cooling jet
- Effect of piston motion

The structure of the chapter is as follows: the problem description and methodology are discussed in Section 5.1. The first analysed effect is that of the impingement location. This is discussed in Section 5.2. Next, the sampled results obtained from the LES study are used to analyse the effects of a more accurate representation of the oil jet, in Section 5.3. The third analysis is on the quasi-dynamic analysis of the piston motion effect, presented in Section 5.4. The final analysis is done by combining the results of the previously mentioned investigations, and comparing the outcome to a correlation obtained from literature, in Section 5.5. The chapter ends with a summary of the main conclusions.

5.1. Problem description

The goal in this chapter is to investigate the effect of the four mentioned simplifications on the heat transfer and piston temperatures, by undoing these simplifications and returning to a more realistic situation. The effect is investigated by comparing the results to the results obtained in the previous chapter, with the simplified disc model. The effect of the confinement is not investigated separately, and is implemented for all simulations in this chapter. This is done by changing the boundary that represents the cylinder wall from an *outlet* boundary condition to a *no-slip wall* boundary condition, as is shown in Fig. 5.1.

The first investigation then is on the location of impingement. It was assumed that the impingement takes place in the centre of the disc, resulting in an axisymmetric problem. In the real configuration there is the piston pin located just below the centre of the piston, and therefore the impingement needs to take place on the side. By shifting the impingement location, the effect on the heat transfer and surface temperatures is investigated.

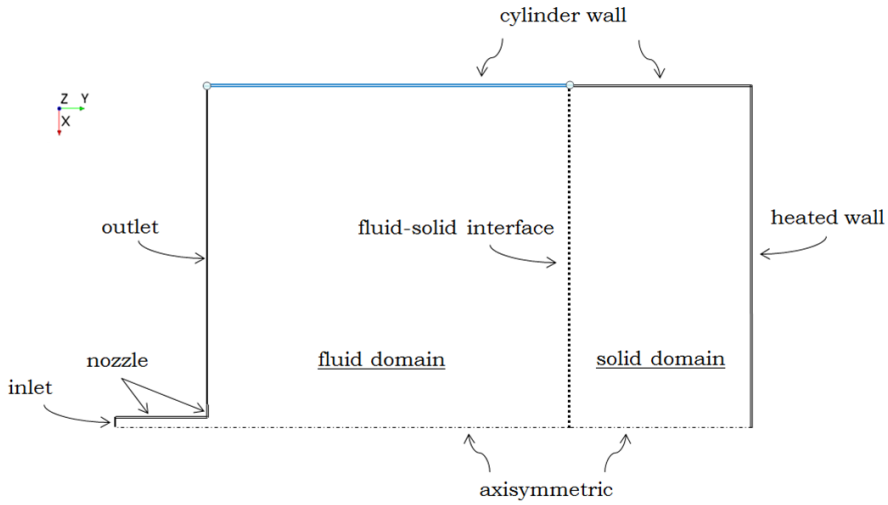

Figure 5.1: Implementation of the confinement, by representing the fluid domain boundary (in radial direction) by a *no-slip wall* boundary condition.

The second investigation then involves the implementation of the LES results for the piston cooling jet obtained in Chapter 3. As the jet modelled with RANS was unaffected and remained straight, a more accurate representation of the jet is expected to influence the heat transfer. It was already mentioned in the trend analysis of Chapter 3 that the output parameters for the spray cooling technique are the sampled volume fraction and sampled axial velocity of the jet, which are now used as inlet conditions.

The third investigation is performed by implementing the piston motion to the CFD model. Because of time constraints, this investigation is conducted as a quasi-dynamic investigation; by determining the effective velocity of the jet, and performing a static analysis with this velocity.

Finally, a combined analysis is performed, and the outcome for the area-averaged Nusselt number is compared to the correlation of Easter, et al. presented in Chapter 2.

5.2. Impingement location

In the simplified disc problem of Chapter 2 it was assumed that the impingement takes place in the centre of the disc, such that the problem is axisymmetric and the analysis can be done in 2D. This resulted in a very simple and fast way to make predictions for the heat transfer. The effect of this assumption is now investigated by testing other impingement locations, as depicted in Fig. 5.2. The location of the DAF piston cooling jet is at r = 45 mm from the centre. Since the axisymmetric property of the problem is lost when the impingement is not in the centre of the disc, a 3D computational domain needs to be used. However, the resulting problem is still symmetrical and thus a half-cylindrical domain can be used, as is shown in Fig. 5.3. All model and mesh settings are kept the same as the settings used for the 2D model, as discussed in Section 4.3. The analysis is performed for the reference piston cooling jet only (flow rate = $7L/min$, oil temperature = 100 $°C$ and nozzle diameter = 3 mm).

5.2.1. Nusselt number results

The results for the Nusselt number are presented in Fig. 5.4. The profile obtained for the centre impingement with the 2D model is also included into this figure.

Since the lower surface is still flat, the shape of the Nusselt number in the stagnation zones is the same,

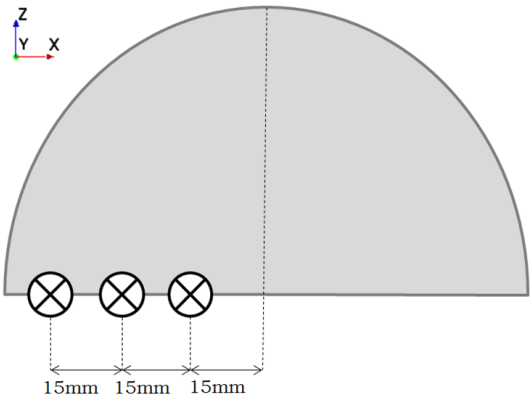

Figure 5.2: Indication of tested impingement locations.

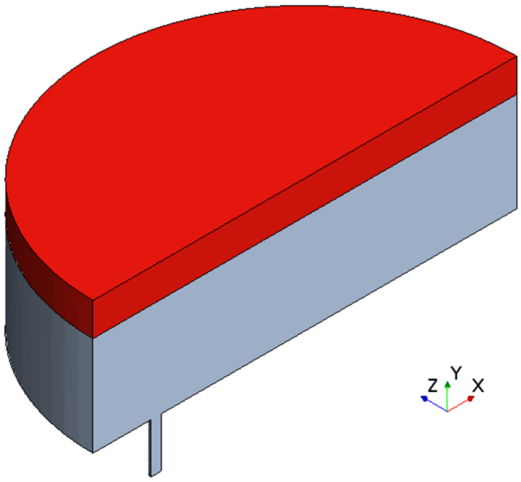

Figure 5.3: Example of the symmetrical computational domain, for the impingement at r = 45 mm.

and thus independent of the location of impingement. Further, it can be seen that there is a very similar development in the positive x-direction for all tested impingement locations. In the negative x-direction however, it can be seen that there is a clear effect of the confinement that is added to the model, where the Nusselt number distribution abruptly drops due to this confinement; the flow velocity is decelerated to zero. The results for the entire half-disc are shown in Fig. 5.5. This figure also shows that the stagnation zone is very similar for the tested impingement locations.

It can be seen that for the impingement location at r = 45 mm, the Nusselt number profile shows a non-physical behaviour at the outer parts of the disc (in positive x-direction). This behaviour in Nusselt number profile was observed before in Chapter 4, and was caused by the detachment of the oil from the surface because of the low radial velocity. By visualising the flow field, one can confirm that this is also what is happening here. The volume fraction of oil is visualised in Fig. 5.6 for the three impingement locations. It can be seen that indeed the flow is not able to cover the entire surface when the impingement location is at radial location r = 45 mm.

As was stated by Easter [18], it is common in spray cooling investigations to determine the area-averaged Nusselt number (Nu_{avg}), as these are of more engineering value. The reasons for this were given to be the complex piston geometry and the large spatial variations in heat transfer. The piston is still modelled as a disc in this analysis, nevertheless it can be seen that there are indeed large spatial variations in heat transfer.

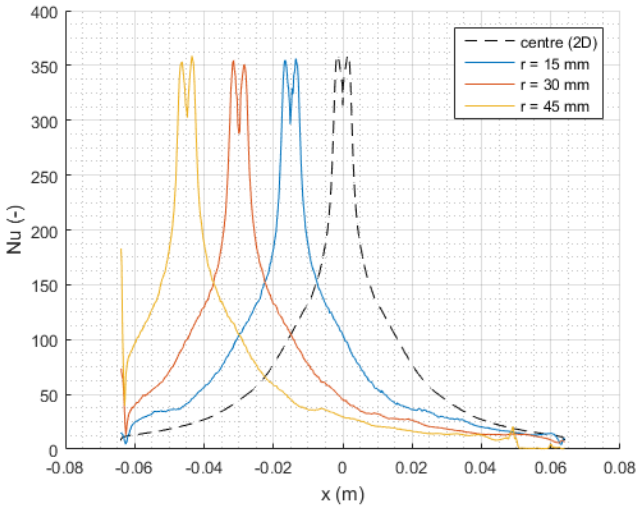

Figure 5.4: Results for Nu on the symmetry axis of the domain, for different impingement locations.

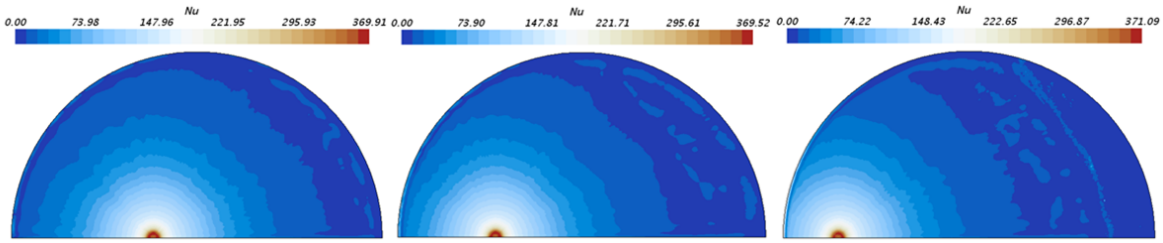

Figure 5.5: Nusselt for Nu for the complete half-disc, for different impingement locations.

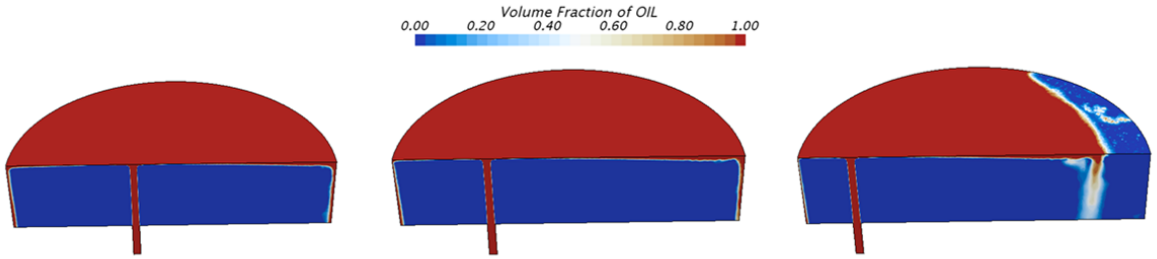

Figure 5.6: Wetted area for the tested impingement locations.

Nu_{avg} is therefore calculated and presented in Table 5.1. It can be seen that shifting the location of impingement results in a decreasing Nu_{avg}, which is not surprising as the location of maximum heat transfer is shifting.

Table 5.1: Comparison of Nu_{avg} values for different impingement locations.

Impingement location	centre (2D)	r = 15 mm	r = 30 mm	r = 45 mm
Nu_{avg}	35	32	30	27

5.2.2. Temperature results

The resulting steady-state temperatures for the cooled surface (on the symmetry axis) are plotted in Fig. 5.7. These plots are the logical result of the Nusselt number distributions, as exactly the opposite effect is observed. Temperatures on the left side of the impingement location are decreased, whereas the opposite happens on the other side. The shape of the plots in the stagnation zones are again very similar. It can be seen that when the impingement is at r = 45 mm the temperature on the symmetry axis increases to 900 °C, which is much higher than the temperature limit of the piston (480 °C). On the upper surface of the piston, these temperatures are even higher, as can be seen in Fig. 5.8.

A possible reason for this (extreme) outcome for the temperature could be the heat flux that is applied as a boundary condition. In reality this heat flux is not uniform and it could very well be that the applied flux is too high. The heat flux effect was shown in Section 4.5 to only affect the disc temperatures, and the effect on the flow field (and the Nusselt number) is negligible. Therefore the results for the temperature can be questioned. Nevertheless, the effect of the shifting impingement location is nicely visualised and will also be present when a more accurate heat flux boundary condition is used.

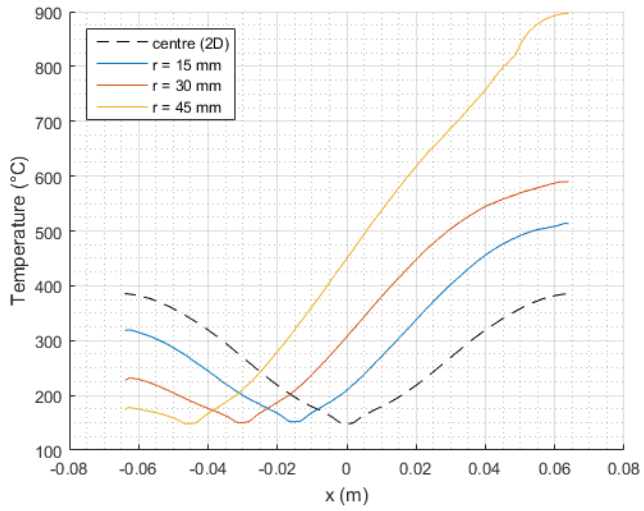

Figure 5.7: Results for T on the symmetry axis of the domain, for different impingement locations.

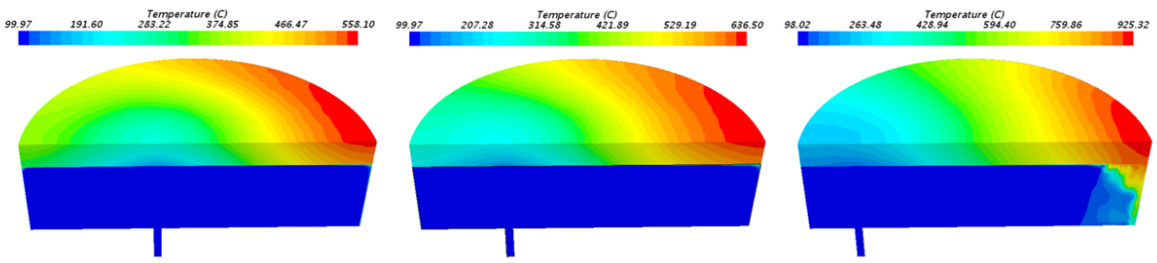

Figure 5.8: Temperature distribution in the entire disc, for different impingement locations.

5.3. Implementation of the LES results into RANS

The second investigation in this chapter is done by implementing the LES results obtained in Chapter 3 into the RANS model. The parameters that are needed are the sampled volume fraction and sampled axial velocity. The goal is to use these outputs from the LES investigation as inputs to the simplified 2D impingement model of Chapter 4, as depicted in Fig. 5.9

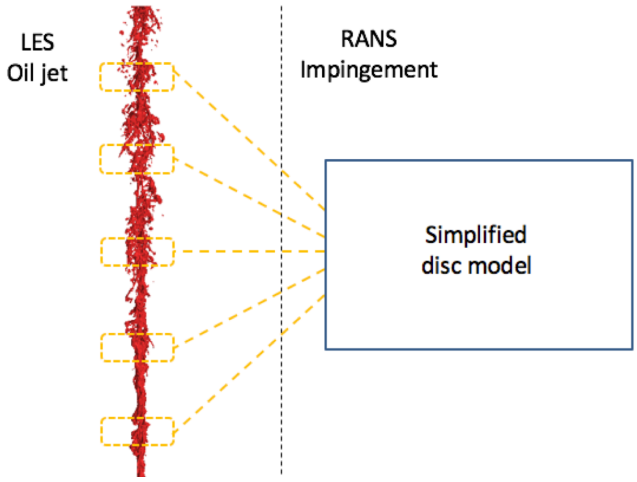

Figure 5.9: Explanation of the implementation of the LES results into the 2D RANS simplified disc model.

Since the jet properties were obtained at different piston locations (BDC, Q1, Q2, Q3, TDC), the aim at the inlet of the domain is to represent these free jet characteristics. Therefore the domain used in the previous chapter needs to be slightly modified. The first modification is to remove the nozzle from the domain, and replace it by a larger inlet that can be used to apply the sampled results for the volume fraction and velocity on, as is shown in Fig. 5.10.

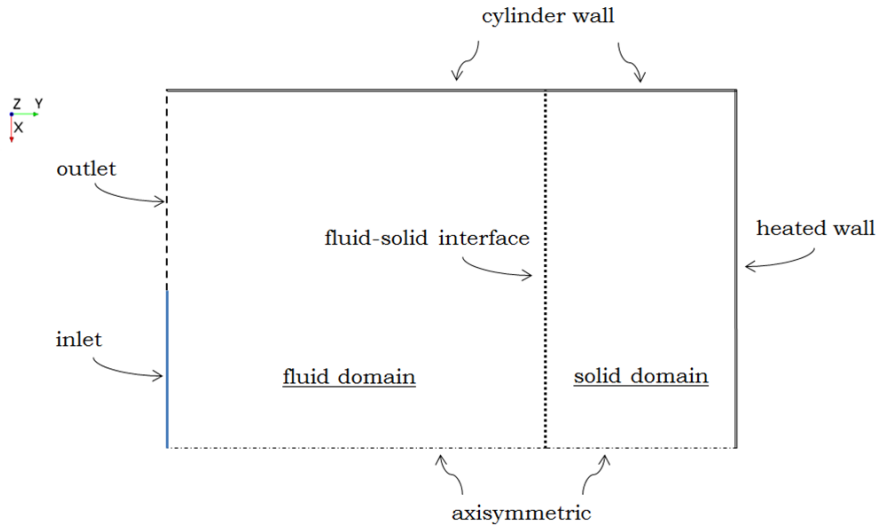

Figure 5.10: Schematic of the modified 2D-axisymmetric computational domain.

The second modification is related to the VOF model. In all previously conducted (RANS-VOF) heat transfer simulations the second-order VOF convection scheme was used, resulting in a sharp interface between the oil and air phases. This interface separated regions consisting fully of either oil or air. The goal is now to represent the oil phase entering the domain by the sampled volume fraction results, which are not consisting fully of oil; it is a mixture of oil and air, because of the time-averaging. This means that a sharp interface is not needed. The modification is therefore to switch to the first-order VOF convection scheme, which is not forcing the model to keep a sharp interface. It was shown that the effects of this order reduction are negligible for the jet modelling in Chapter 3 and for the impingement in Chapter 4. An example of the flow field is shown in Fig. 5.11. It can be seen that the profile applied to the inlet is nicely maintained up to the impingement with the disc, which is exactly what is desired.

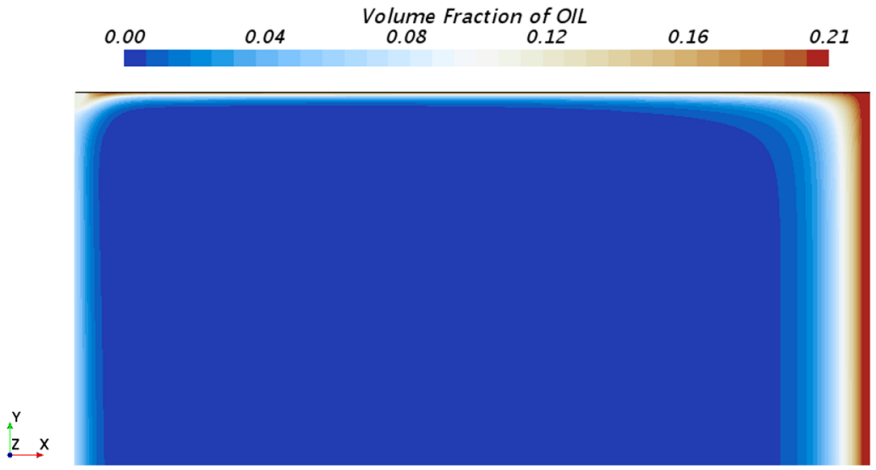

Figure 5.11: Flow field of the LES-RANS simulation, where the sampled LES results are used as inlet conditions to the RANS model.

It was also found that this order reduction is only valid on a structured grid. The first-order VOF convection scheme with a polyhedral grid was shown to result in the introduction of numerical diffusion. Therefore, the third modification with respect to the CFD model presented in Chapter 4 is to switch from a polyhedral grid to a structured grid. All other settings of the CFD model are kept the same.

The analysis is done with the sampled results for the 5 piston locations defined in Chapter 3 and for the reference piston cooling jet only (flow rate = $7 L/min$, oil temperature = 100 $°C$ and nozzle diameter = 3 mm).

5.3.1. Nusselt number results

The results for the Nusselt number on the surface are presented in Fig. 5.12. Nu obtained with the RANS jet in Chapter 4 is also included to this figure (as the dashed black line). It can be seen that there is a decrease of Nusselt number in the stagnation zone when the piston moves upwards. The opposite is observed at the outer parts of the disc, where the Nusselt number is increasing.

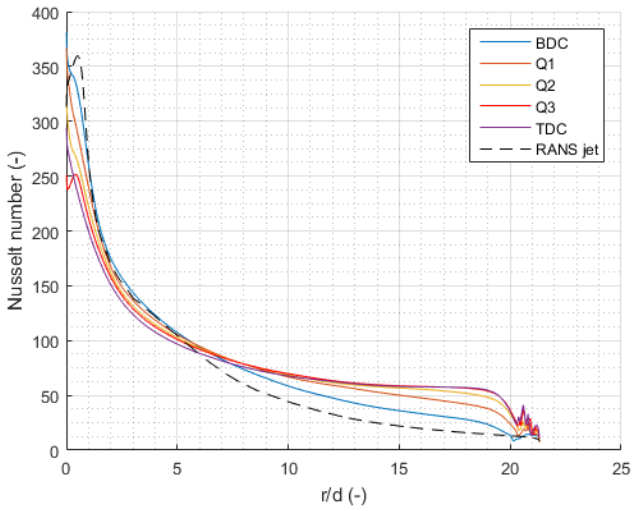

Figure 5.12: Results for the Nusselt number at different piston locations, obtained with the sampled LES results. The dashed line represents the Nusselt number obtained with RANS in Chapter 4.

The shape of the Nusselt number in the stagnation zone deviates from the earlier observed shapes. This is most likely caused by the sampled LES results, which are not physical conditions but time-averaged samples

of the volume fraction and the velocity. Therefore, the odd shapes in the stagnation zone are not further investigated. A good way to still see the effect on Nu_0 is by calculating the area-averaged values for Nu_0. These results are shown in Fig. 5.13. It can be seen that there is a clear decrease in the stagnation zone when the piston moves upwards.

It was shown that the sampled velocity remains reasonably constant for all piston locations in Fig. 3.33, and this decrease in Nu_0 needs to be caused by the decreasing volume fraction on the jet centre axis (Fig. 3.32). Since oil is a better coolant than air, a decreasing oil volume fraction means the contains less oil and more ail. As the fluid properties in VOF are determined with the volume fraction, this outcome makes sense.

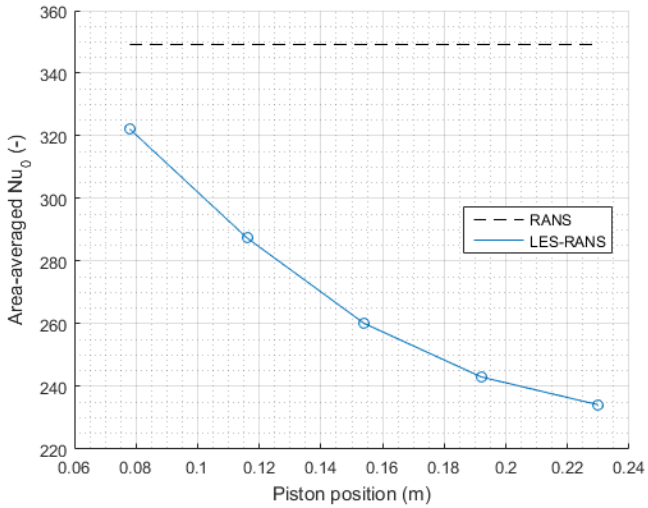

Figure 5.13: Results for Nu_0 at different piston locations, obtained with the sampled LES results. The dashed line represents Nu_0 obtained with RANS.

For the outer parts of the disc an interesting outcome is observed. Firstly, there is again a clear effect of the confinement. Secondly, the increasing Nusselt numbers here are very similar to the results obtained when the jet diameter was varied in Section 4.5. It was shown that an increase of jet diameter results in a jet that is able to cool a larger surface, resulting in higher Nusselt numbers at the outer parts of the disc. This effect was referred to as the diameter effect. The spreading behaviour of the jet can be seen as an increase of local diameter of the jet, and the diameter effect is thus nicely observed in these results as well. Even though the cooling capabilities of the working fluid are decreasing, the spreading behaviour results in higher Nusselt numbers at the outer parts of the disc.

The final step is to determine the area-averaged Nusselt numbers for the entire surface again. Since five different piston locations are considered now, this needs to be done for every piston location. The results are shown in Fig. 5.14. It can be seen that the trend observed for the outer parts of the disc is dominating the area-averaging: Nu_{avg} is increasing with increasing jet length. This outcome makes sense, as the outer parts of the disc cover a much larger area of the disc than the centre. Nu_{avg} for the RANS jet is clearly lower, as it was shown that this jet does not spread, and thus there is a relatively low heat removal on the outer parts.

Another way of presenting these results for Nu_{avg} is by plotting them versus the crank angle. This is done for two engine cycles in Fig. 5.15. These plots can now be used to determine the time-averaged value for Nu_{avg}, also called the cycle-averaged Nusselt number. This is done by averaging over a sufficiently large number of engine cycles, after which the limiting value for Nu_{avg} is reached. The calculated value is shown in Table 5.2. It can be seen that the implementation of the LES jet results in a significant increase (62%) in $Nu_{cycle-avg}$ with respect to the RANS jet. The explanation of this outcome is the same as before: the spreading behaviour of the jet is not present when RANS is used to model the piston cooling jet. It is shown that the effect of the spreading behaviour is similar to the diameter effect obtained in Section 4.5, resulting in higher Nusselt number values on the outer parts of the disc.

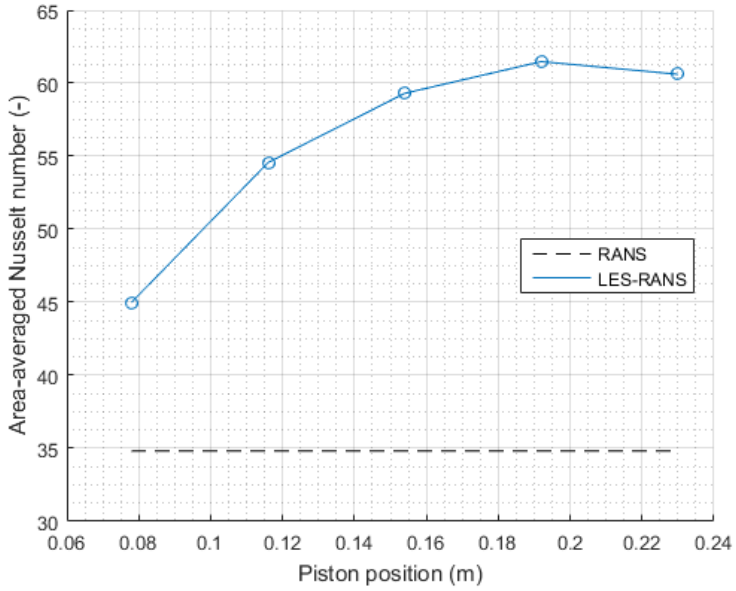

Figure 5.14: Results for Nu_{avg} at different piston locations, obtained with the sampled LES results. The dashed line represents Nu_{avg} obtained with RANS.

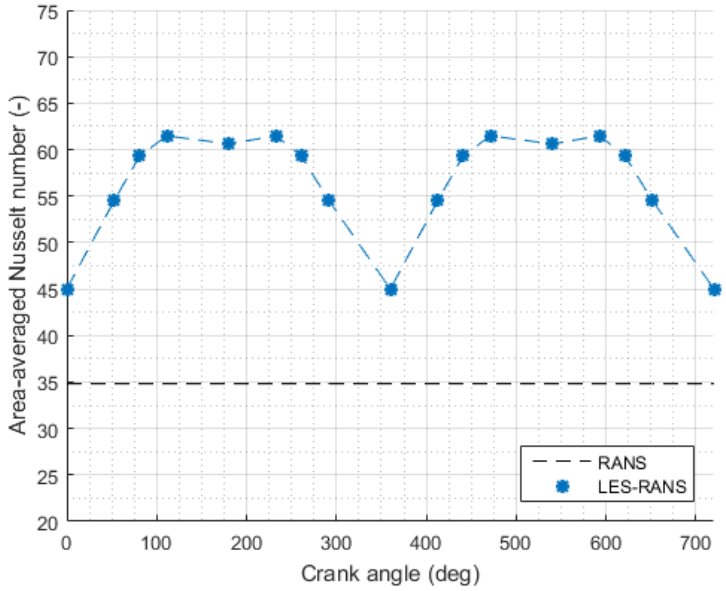

Figure 5.15: Results for Nu_{avg} obtained with the LES results, plotted versus the crank angle.

Table 5.2: The effect of the implementation of the LES results on $Nu_{cycle-avg}$.

	RANS	LES-RANS
$Nu_{cycle-avg}$	35	60

5.3.2. Temperature results

Next, the resulting steady-state temperature distributions on the cooled surface are investigated. Fig. 5.16 shows that the temperatures on the surface are increasing when the piston moves upwards. Again a look at the results obtained for the diameter effect in Section 4.5 can provide more insight into these results. It was found that the diameter effect on the temperature was not present for jet diameters larger than 3.5 mm

(with constant disc diameter D). When the sampled volume fraction plots in Fig. 3.32 are analysed, it can be seen that the local diameter of the DAF oil jet exceeds this 3.5 mm and it can thus be concluded that there is no diameter effect on the surface temperatures. Again, the relative increase of local diameter of the jets is not large enough to make a significant difference in surface temperature. The observed differences in temperature are caused by the decreasing Nusselt numbers in the stagnation zone.

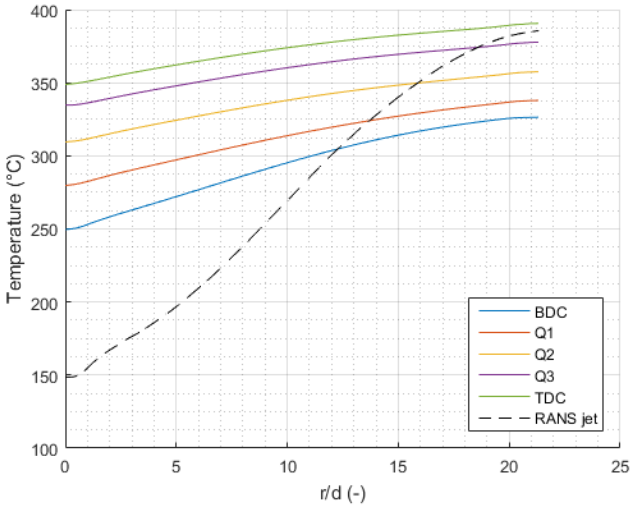

Figure 5.16: Results for the cooled surface temperature at different piston locations, obtained with the sampled LES results. The dashed line represents the lower surface temperature obtained with RANS.

5.4. Piston motion

The third investigation in this chapter is on the effects of the reciprocating motion of the piston. The position and velocity of the piston versus the crank angle are plotted in Fig. 5.17, for the MX-13 engine running at 1600 RPM. The BDC and TDC locations again coincide with respectively 0 and 180 ° crank angles. It can be seen that the velocity of the piston is zero at these locations, as these are the minimum and maximum positions of the piston.

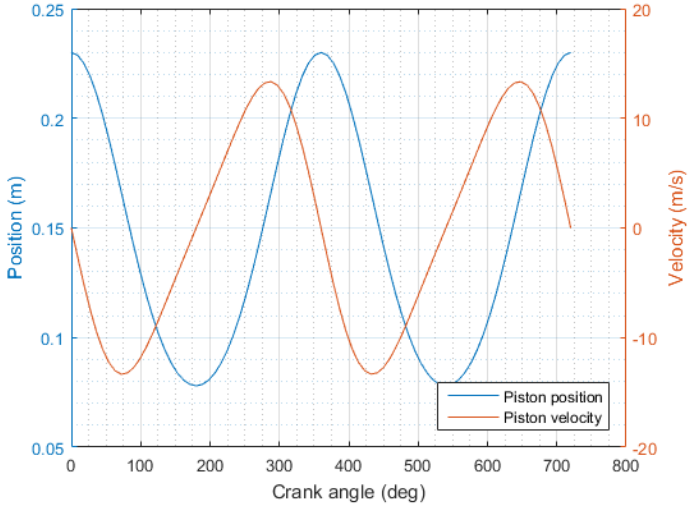

Figure 5.17: Piston position and piston velocity versus the crank angle (at 1600 RPM).

As was mentioned before, because of time constraints only a quasi-dynamic analysis is performed, instead of a full dynamic one. This is done by first determining the piston velocities at the defined 5 piston locations, for

both the stroke-up and the stroke-down. These are presented in Table 5.3. These velocities can now be used to determine the effective velocity (v_{eff}) of the oil jet, as is explained in Fig. 5.18. Since the analysis needs to be performed for different piston locations, the LES representation of the jet is used instead of the modelling the jet in RANS. This means that this analysis is very similar to the analysis performed in Section 5.3, except for the different jet velocities now.

Table 5.3: Velocity of the piston for the (five) earlier defined piston locations.

Piston location	Velocity stroke down (m/s)	Velocity stroke up (m/s)
BDC	0	0
Q3	-10.4	10.4
Q2	-13.3	13.3
Q1	-12.3	12.3
TDC	0	0

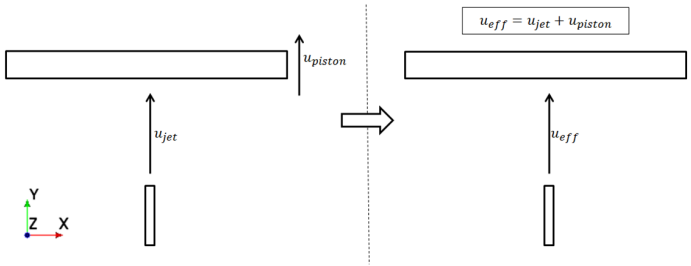

Figure 5.18: Calculation of v_{eff} by using the piston velocity.

5.4.1. Nusselt number results

The local Nusselt number results are presented in Fig. 5.19. The dotted lines represent the locations Q1, Q2 and Q3 in a stroke-down and the dashed lines represent these locations in a stroke-up. The solid lines represent the BDC and TDC locations of the piston, where the piston velocity is equal to zero. Since the motion is implemented by calculating v_{eff}, the results are similar to the results obtained for the flow rate effect in Section 4.5, where only the velocity of the jet was varied. This is essentially what is happening here as well, and it can be seen that the piston velocity dominates the outcome for the Nusselt number. It can be seen that the heat transfer decreases significantly in a stroke-up of the piston. These simulations are performed for the reference jet with a flow rate of 7 L/min jet, with a bulk velocity of 16.5 m/s. When the results for the other tested flow rates (5 L/min and 3 L/min) would be considered, with bulk velocities of respectively 11.8 and 7.1 m/s, these jets would not be able to reach the piston at the Q1, Q2 and Q3 locations in a stroke-up, as the piston velocity is larger than the velocity of the jet.

Further, the effect of the confinement is again clearly visible in the results for the stroke-down results. The Nusselt number profile abruptly drops to zero. The stroke-up results do not show the effect of the confinement. The drop to zero at large r/d is due to the low effective velocity of the jet, resulting in the detachment of the oil from the surface.

As was done before, again the Nu_{avg} values can be calculated and plotted. Nu_{avg} versus the crank angle is plotted in Fig. 5.20. It can be seen that the results over a cycle are now completely different, because of the piston velocity, which is dominating the outcome for Nu and Nu_{avg}. The cycle-averaged value for the Nusselt number is calculated and presented in Table 5.4. It turns out that the effect of piston motion on $Nu_{cycle-avg}$ is very small, as it results in a decrease of only 3% compared to the cycle-averaged results for the stationary situation. Since the piston velocity is dominating the outcome for the Nusselt number, it can thus be concluded that the velocity effects in a stroke-up cancel out the effects in a stroke-down, resulting in a similar cycle-averaged value for the Nusselt number.

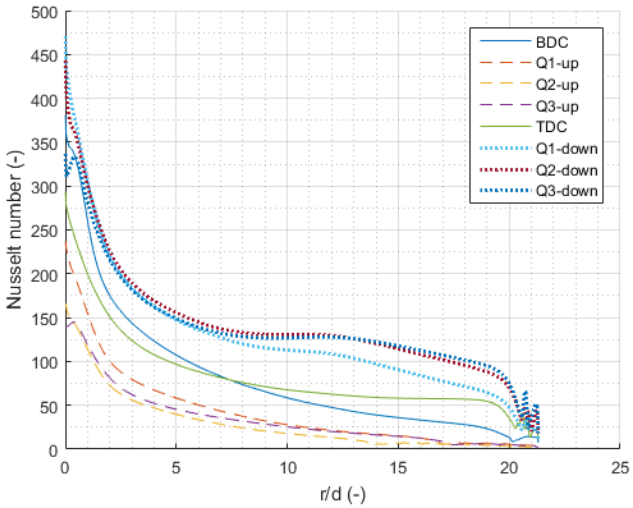

Figure 5.19: Nusselt number results for a full engine cycle, when the piston motion is included (quasi-dynamic).

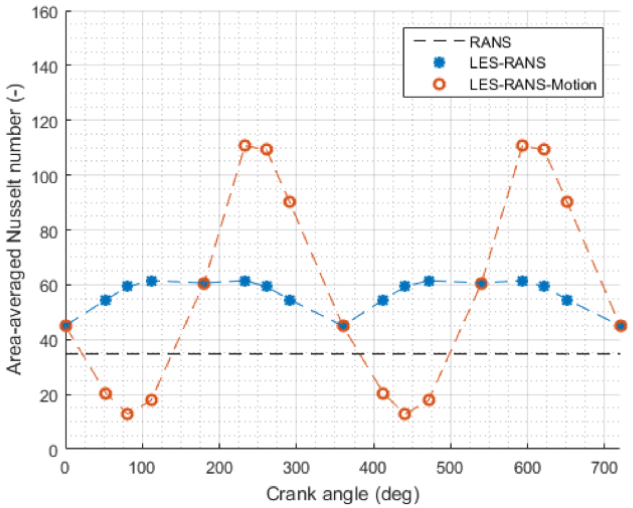

Figure 5.20: Nu_{avg} plotted versus the crank angle for two engine cycles and the comparison to the results obtained without the piston motion effect.

Table 5.4: The effect of the implementation of the LES results on $Nu_{cycle-avg}$.

	RANS	LES-RANS	LES-RANS-MOTION
$Nu_{cycle-avg}$	35	60	58

5.4.2. Temperature results

The resulting steady-state temperature distributions are plotted in Fig. 5.21. The effect of the velocity is again clearly present in the results, as the temperatures reach extremely high values at the Q1, Q2 and Q3 location in a stroke-up motion of the piston. The opposite is observed for the stoke-down results, were there is a very strong cooling and thus very low temperatures.

A possible reason for the extremely high temperatures could again be the value of the applied constant heat flux on the combustion side of the disc, as was mentioned before. A lower heat flux will result in lower temperatures, without affecting the Nusselt number profiles. Another reason could be the fact that these are steady-state temperatures. In a real running engine, these temperature can never be reached, simply be-

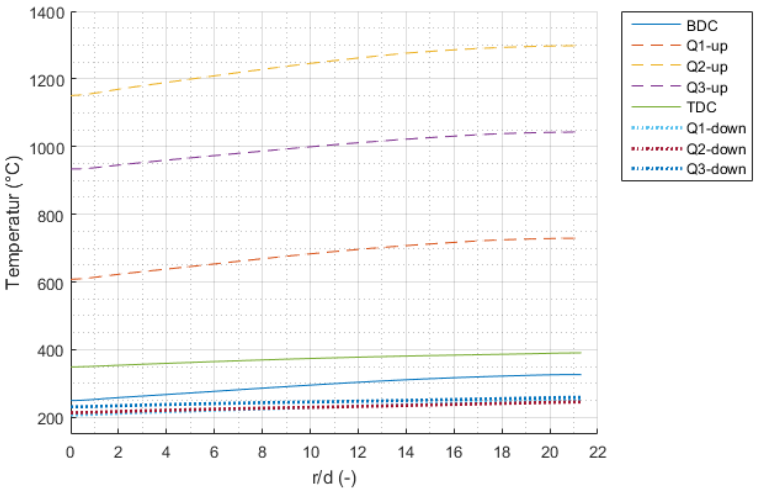

Figure 5.21: Steady-state temperature results for a full engine cycle, when the piston motion is included (quasi-dynamic).

cause there is no time for the piston temperature to reach this steady-state temperature in a stroke-up. This can be shown with a simple energy balance example:

$$Q_{in} - Q_{out} = \Delta E.$$

The heat into the disc (Q_{in}) is equal to the heat flux times the area of the disc, whereas the heat out (Q_{out}) is equal to the convective heat transfer coefficient times the area and the temperature difference between the surface temperature and the oil temperature (at the nozzle). It is assumed that the temperature is uniform in the disc. The energy increase is then equal to the temperature increase times the mass times the specific heat of the disc material:

$$q'' A - hA(T_s - T_\infty) = mC_p \frac{dT}{dt}.$$

Since the change of T is the same as the change of $\frac{T-T_\infty}{T_0-T_\infty}$, this term is non-dimensionalised and the equation is rearranged, resulting in the following differential equation:

$$\frac{d}{dt}\left(\frac{T-T_\infty}{T_0-T_\infty}\right) + \frac{hA}{mC_p}\left(\frac{T-T_\infty}{T_0-T_\infty}\right) - \frac{qA}{mC_p} = 0.$$

The solution of this ordinary differential equation is in the form:

$$\frac{T-T_\infty}{T_0-T_\infty} = C_1 e^{-At} + \frac{B}{A},$$

with A = $\frac{hA}{mC_p}$ and B = $\frac{qA}{mC_p}$. The constant C_1 can be determined with the initial condition at t = 0, where $\frac{T-T_\infty}{T_0-T_\infty}$ needs to be equal to 1, resulting in $C_1 = (1 - B/A)$.

By substituting the material properties of the piston material, the time needed to go from the initial temperature to an extremely high temperature, such as 1000 °C, can now be calculated. The convective heat transfer coefficient can be calculated with Eq. (4.1), and the heat flux q'' is again 250,000 kW/m^2. This results in a time of t = 0.41 seconds, with a specific heat equal to 500 $J/(kg-K)$, a disc mass of 1.01 kg and an initial temperature of 350 °C (obtained from Section 4.5 for the 7 L/min flow rate jet). To compare: at 1600 RPM

one engine cycle takes around 0.038 seconds, which is thus much lower than the time needed to reach these extremely high temperatures.

It can thus be concluded that the quasi-static investigation is not an accurate way of predicting the temperatures on the disc, and a real dynamic analysis is needed. Since the heat transfer profiles for the Nusselt number are determined for different locations (in both the stroke-up and stroke-down), a CFD model can be developed where only the disc is simulated, where these Nusselt number results can be applied as a varying boundary condition on the cooled surface of the disc. This is not included in this thesis, and is mentioned as a recommendation for future studies.

5.5. Combined

The final analysis in this chapter is on the determination of the combined effect of the earlier performed investigations. The motion of the piston is not included to this analysis, as the results for Nu were dominated by the piston velocity (and not the jet properties), and the value for $Nu_{cycle-avg}$ is hardly affected when the cycle-averaging is done. This analysis thus contains the confinement, the implementation of the LES results and the impingement locations.

The location of the DAF piston cooling jets are at a radial distance of 45 mm from the piston centre, as is indicated in Fig. 5.22. Since the axisymmetric property of the problem is again lost by changing the impingement location, a 3D computational domain needs to be used, similar to the domain used in Section 5.2. Also the modifications done for the analysis in Section 5.3 (because of the time-averaged inlet conditions for the volume fraction) are applied to this domain. The computational domain is shown in Fig. 5.23, with the large inlet plane to represent the free jet characteristics at impingement location r = 45 mm.

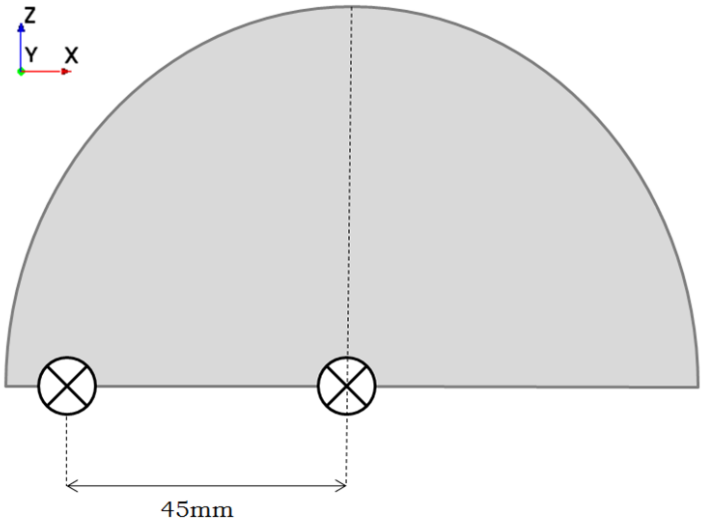

Figure 5.22: Indication of tested impingement locations.

5.5.1. Nusselt number results

Again the analysis is performed for the BDC, Q1, Q2, Q3 and TDC locations of the piston. The results for Nu_{avg} of this combined analysis are shown in Fig. 5.24 (yellow dots), plotted for two engine cycles. Also included to this figure are the results obtained for the RANS jet impinging in the centre, the RANS jet impinging at r = 45 mm and the LES-RANS jet impinging in the centre.

The effect of each simplification is nicely visualised in this figure. It was shown before that Nu_{avg} decreases

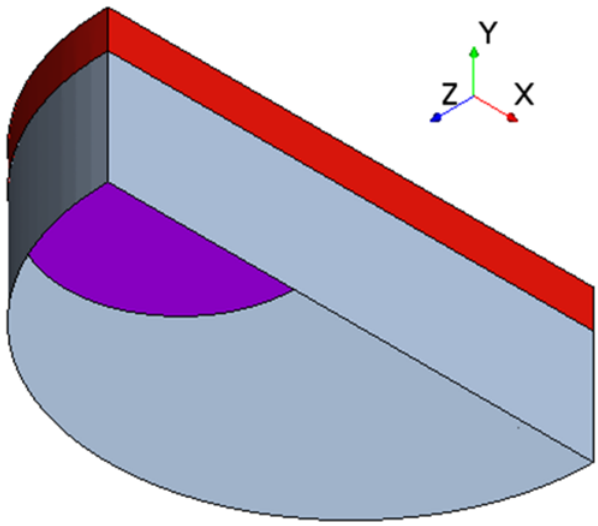

Figure 5.23: Symmetrical 3D domain used for the combined analysis of the impingement locations and LES representation of the oil jet.

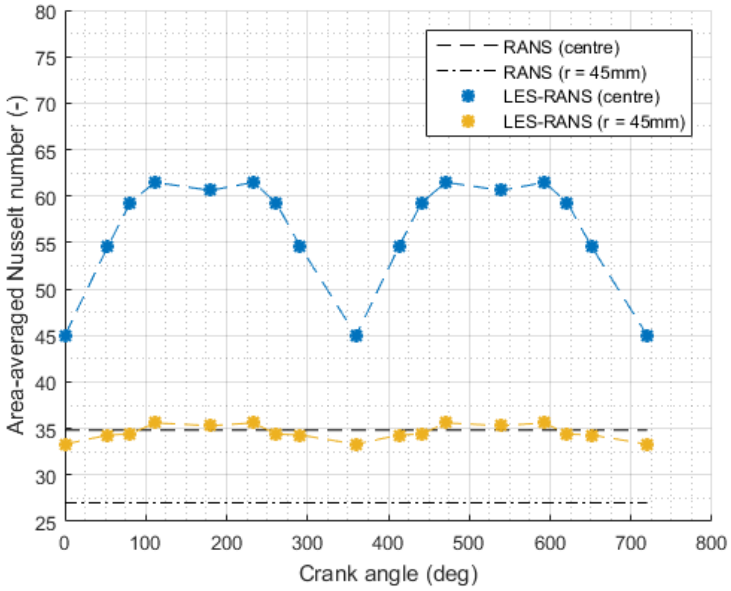

Figure 5.24: Results for Nu_{avg} for the RANS and LES-RANS simulations, at impingement locations in the centre and at r = 45 mm.

when the impingement location is shifted outwards. The confinement on the impingement side of the piston resulted in an abrupt cut-off of the Nusselt number profile and the other side of the piston was not entirely covered with oil, resulting in a drop in the Nusselt number profile. It was also shown that Nu_{avg} increases when the LES results are used to represent the oil jet, because of the increasing local jet diameter, resulting in the diameter effect for the outer parts of the disc. The combined effect appears to cancel out the individual effects, as Nu_{avg} varies around the same value as obtained with the RANS impingement in the centre.

This is confirmed by the cycle-averaged results, listed in Table 5.5. It can be seen that the value for the LES-RANS jet impinging on the side of the disc is the same as the RANS jet impingement in the centre. It is believed that this exact match is coincidental, as the results for the LES-RANS impingement on the side are derived

by performing two totally unrelated implementations: the shift of location and the implementation of LES results. Therefore the conclusions drawn from these results need to be carefully formulated, and possible errors or deviations need to be addressed. Nevertheless, it can be said that the combined effect is very small compared to the RANS impingement in the centre case.

Table 5.5: The effect of the implementation of the LES results and the impingement location on $Nu_{cycle-avg}$.

	RANS centre	RANS 45 mm	LES-RANS centre	LES-RANS 45 mm
$Nu_{cycle-avg}$	35	27	60	35

The effect of the two implementations can now be compared when they are implemented separately and when they are implemented in a combined way. When only the impingement location was shifted (for the RANS jet), $Nu_{cycele-avg}$ decreased from 35 to 27, which is a decrease of 23%. The decrease due to the impingement when the LES results are used for the jet is from 60 to 35, which corresponds to 42%. This shows that the effect of the impingement location is stronger when the oil jet is represented with the LES results. The reason for this difference can be found by analysing the local Nusselt numbers at the outer parts of the disc. The Nusselt numbers of the four considered cases are plotted in Fig. 5.25. The plots for the LES results are cycle-averaged to make the comparison easier. Otherwise 5 plots would be needed per case, and this would make the comparison very difficult.

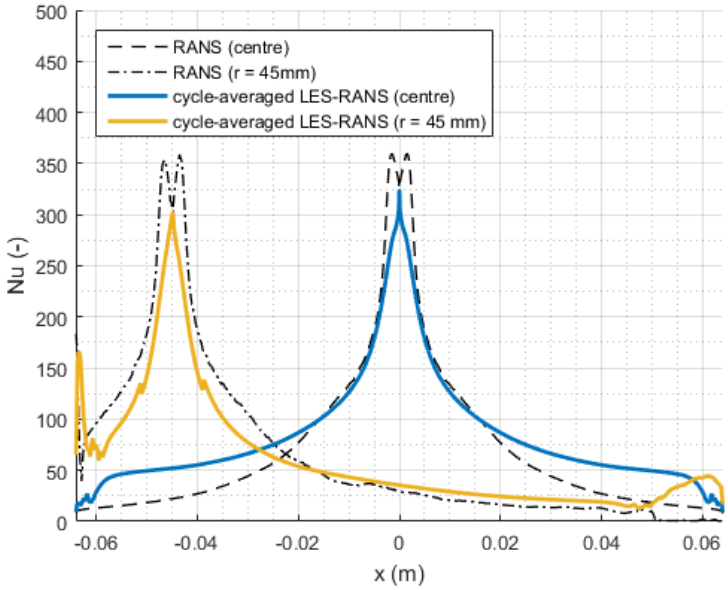

Figure 5.25: Results for the Nusselt number distribution on the symmetry axis for the RANS and LES-RANS simulations, at impingement locations in the centre and at r = 45 mm. The LES-RANS results are cycle-averaged for a more comparison reasons.

It can be seen that the effect of shifting the impingement location results in a larger decrease for the solid lines, than for the dashed and dot-dashed lines, for $x > 0.02$. However, if the solid lines are carefully compared to each other, it can be seen that the Nusselt number profiles are not similar. They are similar in the stagnation zone, but outside this region, the profile obtained for the side impingement appears to decrease much faster than when the impingement takes place in the centre. The only difference between these two simulations is ofcourse the impingement location and the computational domain, since for side impingement a 3D domain is needed. It could very well be that the first-order VOF convection scheme that is used for the LES-RANS simulation is producing a larger discretisation error when a 3D domain is used. This different behaviour on the surface results in a larger impingement location effect, which is the reason for the higher decrease compared to the impingement location effect when the jet is modelled with RANS.

The same comparison can now be made for the effect of the implementation of the LES results. When this is done for impingement in the centre, $Nu_{cycle-avg}$ increases from 35 to 60, which is equal to an increase

of 71%. When this effect is analysed for impingement at r = 45 mm, $Nu_{cycle-avg}$ increases from 27 to 35, corresponding to an increase of 29%. It can thus be said that the effect of the LES-RANS implementation is stonger when the impingement takes place in the centre of the disc, which is the same conclusion as was drawn before.

The accuracy of the final results for $Nu_{cycle-avg}$ can now be assessed by comparing it to the results obtained for $Nu_{cycle-avg}$ with the correlation of Easter, et al., presented in Chapter 2. This is done inTable 5.6. It can be seen that there is an under-prediction for the test case of 19%. A possible reason for this outcome could be related to the test case itself. It is observed that the correlation does not contain a disc/piston diameter (D) dependency. Easter, et al. performed their experiment on a passenger car piston, which is smaller in diameter than the DAF pistons. Since the results at the outer parts of the disc are dominating the outcome of the area-averaging, it can be said that if the CFD simulation would be repeated with a smaller disc diameter, the outcome would result in smaller mismatch.

Another reason could be the impingement location, which is not clearly mentioned in the test case. As Nu_{avg} is decreasing with an impingement location moving to the side, one can imagine that impingement closer to the centre will result in a smaller difference.

A third possible reason for the under-prediction could be the representation of the piston as a disc. As the lower surface of a spray cooling piston is curved, and it was discussed in Chapter 2 that concave surfaces can increase the heat transfer, the implementation of a curved lower piston surface could decrease the mismatch.

Table 5.6: Comparison of final value for $Nu_{cycle-avg}$ with the results of Easter, et al [18].

	LES-RANS	Easter, et al.
	45 mm	
$Nu_{cycle-avg}$	35	43

5.6. Conclusions

In this chapter, the simplified disc problem discussed in Chapter 4 is extended by undoing several simplifications, and returning to a more realistic situation. All simulations are performed for the reference jet only. The main findings and conclusions are listed next:

- It was shown when the location of impingement is shifted to the side of the piston, the Nusselt number distribution is not affected, except for the actual shift. Due to the confinement that is caused by the cylinder wall, this results in an abrupt blockage of the oil, resulting in a cut-off of the Nusselt number. For the other side of the disc (with respect to the impingement side), it was observed that the oil jet is not able to reach the end of the disc, due to the radial velocity decreasing to zero, resulting in detachment of the oil.
- The sampled results for the oil jet obtained in Chapter 3 are used to analyse the effect of a more accurate representation of the oil jet. This is done by using the results for the volume fraction and velocity directly as inlet conditions and evaluating the effect on the heat transfer, for the five defined piston locations. The observed effect was that due to the volume fraction decrease on the jet centre axis, there was a decreasing Nu_0 for increasing piston position. On the outer parts of the jet, a similar outcome was observed as for the diameter analyses is Chapter 4: the increasing local diameter (spreading) of the jet results in higher Nusselt numbers at the outer parts of the disc.
- The piston motion is analysed in a quasi-dynamic way, by determining the effective velocity of the jet. It was observed that the velocity of the jet is dominant in the outcome for the Nusselt number, for both the stroke-up and the stroke-down. The total effect was observed to be very small, resulting in a decrease of only 3% for $Nu_{cycle-avg}$ with respect to the static analysis, indicating that the effects of the velocity in a stroke-up and stroke-down cancel each other out.
- The final investigation was one the combined effect of the aforementioned implementations. $Nu_{cycle-avg}$ for impingement on the side and the LES representation of the jet resulted in the same value as was ob-

tained for the RANS jet impinging in the centre of the disc. It is believed that this exact match is purely coincidental, as the results for LES-RANS impinging on the side are derived by two totally unrelated implementations. Nevertheless, it can be concluded that these effects are counteracting, and the simplified 2D model can be very valuable in making area-averaged Nusselt number predictions for the spray cooling technique. To confirm this conclusion, these tests need to be repeated for other operating conditions as well. The comparison with the test case of Eq. (2.27) showed an under-prediction of 19% for $Nu_{cycle-avg}$, which is most likely related to the geometry (dimension and surface curvature) of the piston or the location of impingement used in the experiment.

- It was observed for the RANS jet that the location of impingement does not affect the shape of the Nusselt number profile. This was not the case when the LES results were used to represent the oil jet. The reason for this outcome is most likely the combination of using a first-order VOF convection scheme on a 3D computational domain, which could increase the discretisation error and thus affecting the solution.

6

Conclusions

The present thesis aimed at making the first steps towards a piston cooling CFD model, that can be used by DAF to better understand, analyse and improve their piston cooling process. The project was split up into five sub-projects:

- The liquid jet
- Impingement
- Spray cooling
- Gallery cooling
- Lubrication of the piston pin

In this thesis, the first three sub-projects are covered. The other two are left for future studies, as will be discussed in Chapter 7. The main conclusions for each sub-project are repeated next.

The liquid jet

It was found in literature that the DAF oil jets disintegrate and breakup according to the second wind-induced and/or atomization regimes, based on the Reynolds number and Ohnesorge number. For these relatively unknown breakup mechanisms the aerodynamic drag encountered by the oil is one of the dominant contributors to the breakup. Further, it was observed from literature that the level of interaction and chaotic behaviour of the jets increase for increasing flow rates. This results in a larger droplet and ligament formation, and a spreading behaviour of the jet.

The CFD model to model these jets was obtained by reproducing the test cases first. It was shown that the RANS-VOF combination falls short in modelling the jet behaviour, due to the tendency of the VOF method to maintain a sharp interface between the phases, whereas the aim with RANS is to model the mean flow properties, which is not separated by a sharp interface. The LES-VOF combination proved to be more successful, as the flow rate efficiency experiment of DAF was reproduced within acceptable accuracy. The CFD model was then used to analyse the DAF jets, by performing a trend analysis.

This is done by varying the flow rate, the oil temperature and the nozzle diameter, and investigating the effect of these variations on the jet behaviour. The output parameters were selected such that these can be used in later stages of this thesis (or in future studies) to be: the flow rate efficiency, the sampled volume fraction and the sampled velocity at different piston locations.

The trend analysis results for the flow rate effect showed that also at other piston locations (except for the BDC) there is a clear flow rate effect: a decreasing flow rate efficiency as the flow rate is increased. The volume fraction plots confirmed this, as there was a larger spreading with increasing flow rate. Also the effect of the increasing piston locations showed the increasing spreading distance.

The effect of the temperature was found to be not as strong as variations in flow rate, nevertheless it was found that the spreading behaviour increases with increasing temperatures.Possible reason for the weak dependency on the oil temperature were given to be either a strong dependency on dimensional numbers (instead of the Reynolds number), the approach of a limiting behaviour for Reynolds numbers above the critical Reynolds number and/or the assumption of constant surface tension for the tested jets.

The diameter effect was shown to be more difficult than the first two tests. There are two counteracting effects present when the diameter is varied (at constant flow rate): the diameter and the velocity. At lower piston locations, the diameter itself was shown to be dominant, whereas for higher locations the velocity of the jet was more dominant in the outcome for the flow rate efficiency.

Impingement

The second sub-project was on the analysis of the impingement heat transfer. The literature review for impingement onto a flat surface showed that the highest Nusselt numbers occur in the stagnation zone, followed by a gradual decrease over the target surface. It was obtained from two benchmark studies that the Nusselt number can be estimated with the Reynolds number and the Prandtl number.

The modelling of the impingement was done by simplifying the spray cooling problem. The first simplification was to represent the piston as a heated disc, with constant target distance, heat flux and disc thickness. The impingement location was shifted to the centre of the disc, such that the axisymmetric property of the problem can be used to reduce computation cost. The methodology was again to reproduce test cases, and use the validated CFD model to analyse the DAF jets in the form of a trend analysis.

Since the CFD model was much less computationally expensive, more variations per input parameter were tested. Before starting the analysis, a suitable target distance needed to be determined. It was shown that the effect of the target distance for $L/d < 25$ was negligible.

The first tested parameter was the flow rate. This resulted in an increasing Nusselt number on the entire disc surface, with increasing flow rates. The resulting steady-state temperatures were the logical consequence of the Nusselt number results: decreasing temperatures with increasing flow rates.

The analysis on the temperature effect resulted in a surprising (though logical) outcome: lower surface temperature can be obtained with higher oil temperatures. The reason is that with increasing temperatures, the cooling capabilities of the fluid is increased, resulting in more heat transfer. This was confirmed by comparing the results for Nu_{avg} to the test case results, which were also predicting an increasing cooling capability with increasing oil temperature.

The analysis for the diameter proved to be the most complex one. It was observed that, especially for the smaller tested diameters, there was a clear diameter effect. This was defined as the effect of diameter variations on the outer parts of the disc. It was observed that with increasing jet diameters, higher Nusselt numbers can be obtained on the outer parts of the disc. This effect was shown to be eliminated for jet diameters above 3.5 mm, as the differences in D/d for larger diameters are relatively smaller. The results showed that the optimal jet diameter is 3.5 mm jet, resulting in the lowest T_{avg}.

An extra trend that was tested is the effect of the heat flux. The heat flux effect was shown to slightly affect the Nusselt numbers (< 2%), since flow properties are not varied in this analysis. Increasing the heat flux resulted in serious increases of temperatures on both surfaces.

Spray cooling

The third sub-project of this thesis is on the analysis of the spray cooling technique. The simplified disc model in Chapter 4 was obtained by simplifying the spray cooling problem. The goal in this study was therefore to undo these simplifications and to return to a more realistic simulation. The simplifications that are considered are: the confinement effect, the impingement location effect, the implementation of the LES results and finally the effect of piston motion.

It was shown when the location of impingement is shifted to the side of the piston, the Nusselt number distribution is not affected, except for the actual shift. Due to the confinement that is caused by the cylinder wall, this results in an abrupt blockage of the oil, resulting in a cut-off of the Nusselt number. For the other side of the disc (with respect to the impingement side), it was observed that the oil jet is not able to reach the end of the disc, due to the radial velocity decreasing to zero, resulting in detachment of the oil.

The sampled results for the oil jet obtained in Chapter 3 are used to analyse the effect of a more accurate representation of the oil jet. This is done by feeding the results for the volume fraction and velocity directly as inlet conditions and evaluating the effect on the heat transfer, for the five defined piston locations. The observed effect was that due to the volume fraction decrease on the jet centre axis, there was a decreasing Nu for increasing piston position. On the outer parts of the jet, a similar outcome was observed as for the diameter analyses is Chapter 4. The increasing local diameter (spreading) of the jet results in higher Nusselt numbers at the outer parts of the disc.

The piston motion is analysed in a quasi-dynamic way, by determining the effective velocity of the jet. It was observed that the velocity of the jet is dominant in the outcome for the Nusselt number, for both the stroke-up and the stroke-down. The net effect was observed to be very small, resulting in a decrease of only 3% for $Nu_{cycle-avg}$ with respect to the static analysis.

The final investigation was one the combined effect of the aforementioned implementations. $Nu_{cycle-avg}$ for impingement on the side and the LES representation of the jet resulted in the same value as was obtained for the RANS jet impinging in the centre of the disc. It is believed that this exact match is purely coincidental, as the results for LES-RANS impinging on the side are derived by two totally unrelated implementations. Nevertheless, it can be concluded that these effects are counteracting, and the simplified 2D model can be very valuable in making area-averaged Nusselt number predictions for the spray cooling technique. To confirm this conclusion, these tests need to be repeated for other operating conditions as well. The comparison with the test case of Eq. (2.27) showed an under-prediction of 19% for $Nu_{cycle-avg}$, which is most likely related to the geometry (dimension and surface curvature) of the piston or the location of impingement used in the experiment.

It was observed for the RANS jet that the location of impingement does not affect the shape of the Nusselt number profile. This was not the case when the LES results were used to represent the oil jet. The reason for this outcome is most likely the combination of using a first-order VOF convection scheme on a 3D computational domain, which could increase the discretisation error and thus affecting the solution.

7

Recommendations

The recommendations are divided into two parts. Firstly, the issues encountered during this thesis project are discussed and recommendations on the conducted work are presented, in Section 7.1. The second part of this chapter deals with the recommendations for the two future studies that need to be conducted and is discussed in Section 7.2.

7.1. Thesis work

The liquid jet

The major drawback of the CFD model used for the study of the liquid jet was the extremely high computation time related to LES, which is an undesired feature in industry. The first recommendation is therefore to further investigate ways to decrease the computation time. Especially for the initialisation stage it is believed that it can be decreased when better initial conditions are used.

Nevertheless, LES will always remain computationally expensive, and therefore also further investigations on the RANS method are needed, to find useful relations with the LES results. An example of this is the solution for the turbulent kinetic energy, which showed a similar outcome as the sampled turbulent kinetic energy with LES. If these relations can be found, the jet properties can be predicted with RANS, instead of performing a full LES study.

Impingement

The simplified 2D-axisymmetric model proved to be a very simple, fast and accurate predictor of heat transfer characteristics. This model is extensively analysed and optimised in this thesis, and therefore no recommendations are given for this part of the thesis.

Spray cooling

The first recommendation for this chapter would be related to the implementation of the piston motion. Because of time constraints, this is done as a quasi-dynamics analysis only. Further investigation on motion modelling is needed to determine the effects of motion in a more accurate way. A possible recommendation is to use the results for the Nusselt number at the different piston positions and apply these as boundary conditions to a thermal analysis of the disc only. This way no fluid domain is needed, and a better prediction of surface temperatures can be obtained in a relatively simple and fast way.

The second recommendation is related to the implementation of the LES results. In this implementation the individual effect of the produced droplets and ligaments is neglected, and it is assumed that these are represented by the sampled volume fraction of oil. The effects or uncertainties caused by this assumption are unknown, making the results questionable, even though the results for the Nusselt number make sense. Further investigation is needed on the effects of individual ligaments and droplets on impingement heat transfer.

The third recommendation is related to the implementation of the LES results. In this implementation, the VOF convection scheme order is decreased to the first-order. In 2D the results appeared to be good, however in 3D it was observed that the solution was different. It is advised to investigate the effect of this modification more extensively or find other ways to implement the sampled results for the volume fraction and velocity into a simple 2D impingement model.

7.2. Future work

Gallery cooling

The gallery cooling technique is the cooling technique used in the DAF engines. Since sloshing motion of the oil inside the gallery is the main contributor to the cooling, this simulation needs to by a fully dynamic one, which will increase the computation time of the simulation. However, the LES results can be used to extract the flow rate efficiency versus piston location, which can be used to determine the flow rate entering the cooling gallery. The analysis can then be limited to modelling the cooling gallery only, and this will results in a decrease of computation time.

Lubrication of the piston pin

The lubrication of the piston pin is the last sub-project of the DAF piston cooling research project. Another function of the cooling jets are to continuously lubricate the oscillating piston pin. This can easily be implemented into the CFD model used for the analysis of the gallery cooling technique, by adding an extra outlet hole in the cooling gallery domain. The mass flow through this outlet hole should already give a good impression of the amount of oil that is fed to the piston pin.

Bibliography

[1] M. GmbH, *Piston and Engine Testing* (Heidelberg: Springer Vieweg, 2016).

[2] *The Demands of Diesel Pistons and Sleeves,* Available at: `http://www.enginebuildermag.com/2014/08/demands-diesel-pistons-sleeves/`.

[3] G. Moreno, S. Narumanchi, T. Venson, and K. Bennion, *Microstructured Surfaces for Single-Phase Jet Impingement Heat Transfer Enhancement,* Journal of Thermal Science and Engineering Applications (2013).

[4] H. Liu, *Science and Engineering of Droplets – Fundamentals and Applications,* William Andrew Publishing/Noyes, New York (2000).

[5] D. Skilone, *Characterization of pre- and post-breakup liquid jets,* MSc. Thesis (2009).

[6] S. Moghe and S. Janowiak, *Large Eddy Simulation of Cylindrical Jet Breakup and Correlation of Simulation Results With Experimental Data,* Journal of Engineering for Gas Turbines and Power (2017).

[7] F. Incropera, D. Dewitt, T. Bergman, and A. Lavine, *Fundamentals of Heat and Mass Transfer* (John Wilet & Sons, 2007).

[8] C. Ma, Y. Zhao, T. Masuoka, and T. Gomi, *Analytical Study on Impingement Heat Transfer with Single-Phase Free-Surface Circular Liquid Jets,* Journal of Thermal Science (1996).

[9] J. Stevens and B. Webb, *Local Heat Transfer Coefficients Under an Axisymmetric, Single-Phase Liquid Jet,* Journal of Heat Transfer (1991).

[10] C. Ma, Q. Zheng, H. Sun, and K. Wu, *Local characteristics of impingement heat transfer with oblique round free-surface jets of large Prandtl number liquid,* International Journal of Heat and Mass Transfer (1997).

[11] L. Gabour, *The effects of surface roughness on stagnation-point heat transfer during impingement of turbulent liquid jets,* MSc. Thesis, MIT (1993).

[12] *Thermopedia,* Available at: `http://www.thermopedia.com/content/5239/GorTayF2.gif`.

[13] N. Thiel, H. Weimar, and H. Kamp, *Advanced Piston Cooling Efficiency: A Comparison of Different New Gallery Cooling Concepts,* SAE International (2007).

[14] J. Pan, R. Nigro, and E. Matsuo, *3-D Modeling of Heat Transfer in Diesel Engine Piston Cooling Galleries,* SAE International (2005).

[15] P. Penumadu, *LES and Unsteady RANS Simulations of Multiple Jet Impingement System,* MSc. Thesis (2015).

[16] *User Guide Star-CCM+ Version 12.02.*

[17] G. Nasif, R. Barron, and R. Balachandar, *Simulation of jet impingement heat transfer onto a moving disc,* International Journal of Heat and Mass Transfer (2015).

[18] J. Easter, C. Jarrett, C. Pespisa, Y. Liu, A. Alkidas, L. Guessous, and B. Sangeorzan, *An area-average correlation for oil-jet cooling of automotive pistons,* (2014).

[19] A. Agarwal and M. Varghese, *Numerical investigations of piston cooling using oil jet in heavy duty diesel engines,* International Journal of Engine Research (2006).

[20] H. Kajiwara, Y. Fujioka, and H. Negishi, *Prediction of Temperatures on Pistons with Cooling Gallery in Diesel Engines using CFD Tool,* SAE Technical Papers (2003).

[21] T. Siang, *A study of upward oil jet impingement on flat and concave heated surfaces and the application to IC engine piston cooling,* PHD Thesis, Loughborough (2007).

[22] N. Ladommatos, H. Zhao, and Z. Xiao, *The effect of piston bowl temperature on diesel exhaust emissions,* Proceedings of the Institution of Mechanical Engineers (2005).

[23] J. Lienhard, *Heat Transfer by Impingement of Circular Free-Surface Liquid Jets,* Heat and Mass Transfer Conference (2006).

[24] J. Delteil, S. Vincent, A. Erriguible, and P. Subra-Paternault, *Numerical investigations in Rayleigh breakup of round liquid jets with VOF methods,* Computers & Fluids 2011 (2011).

[25] G. Stiesch, *Modeling Engine Spray and Combustion Processes* (Springer, New York, 2003).

[26] N. Moallemi, *Numerical and experimental investigations in the instability and breakup of capillary waterjets,* MSc. Thesis (2014).

[27] R. Grant and S. Middleman, *Newtonian Jet Stability,* American Institute of Chemical Engineers Journal (1966).

[28] R. Phinney, *Breakup of a Turbulent Liquid Jet in a Low-Pressure Atmosphere,* American Institute of Chemical Engineers Journal (1975).

[29] K. Sallam, Z. Dai, and G. Faeth, *Liquid breakup at the surface of turbulent round liquid jets in still gases,* International Journal of Multiphase Flow (2002).

[30] A. Veen, *ML15-469 (Flow efficiency measurement),* DAF Library (2015).

[31] X. Liu, J. Lienhard, and J. Lombara, *Convective Heat Transfer by Impingement of Circular Liquid Jets,* Journal of Heat Transfer (1991).

[32] N. Mostafa, *Computational Fluid Dynamics Modelling of Three-Dimensional Jet Impingement Cooling On Concave Surfaces,* PHD Thesis, MACE (2007).

[33] H. Thomann, *Effect of streamwise wall curvature on heat transfer in a turbulent boundary layer,* Journal of Fluid Mechanics (1968).

[34] D. Lee, Y. Chung, and S. Won, *The effect of concave surface curvature on heat transfer from a fully developed round impinging jet,* International Journal of Heat and Mass Transfer (1998).

[35] *Introduction to Compressible Flows,* Available at: `https://ocw.mit.edu/courses/aeronautics-and-astronautics/16-01-unified-engineering-i-ii-iii-iv-fall-2005-spring-2006/fluid-mechanics/f11_sp.pdf`.

[36] H. Versteeg and W. Malalasekera, *An introduction to Computational Fluid Dynamics, The Finite Volume Method* (Longman Scientific & Technical, 1995).

[37] B. Oudheusden, *Viscous Flows - AE4120,* Lecture notes, Technical University of Delft (2016).

[38] L. Berselli, T. Iliescu, and J. Layton, *Mathematics of Large Eddy Simulation of Turbulent Flows* (Springer, 2006).

[39] S. Pope, *Turbulent Flows* (Cambridge University Press, UK, 2000).

[40] A. Guha, R. Baron, and R. Balachandar, *Numerical simulation of high-speed turbulent water jets in air,* Journal of Hydraulic Research (2010).

[41] R. Lebas, T. Menard, P. Beau, A. Berlemont, and F. Demoulin, *Numerical simulation of primary break-up and atomization: DNS and modelling study,* International Journal of Multiphase Flow (2009).

[42] E. Olsson, L. Ahrne, and A. Tragardh, *Heat transfer from a slot air jet impinging on a circular cylinder,* Journal of Food Engineering (2004).

[43] G. Nasif, *CFD Simulation of Oil Jets with Application to Piston Cooling,* PHD Thesis (2014).

[44] J. Persson, *Synthetic Inlet Boundary Conditions for LES,* MSc. thesis, Chalmers University of Technology (2015).

[45] U. Gaitonde, *Quality criteria for Large Eddy Simulations,* First year transfer report, University of Manchester (2008).

[46] S. Hickel and S. Hulshoff, *CFD3 - Large Eddy Simulation,* Lecture notes, Technical University of Delft (2016).

[47] *The Steve Portal - Siemens,* Available at: `https://thesteveportal.plm.automation.siemens.com/articles/en_US/FAQ/How-to-create-an-accurate-prism-layer-mesh-in-5-Steps-temp`.

A

10-W30 engine oil property table

The following figure can be used to obtain the relations between temperature, viscosity and density for the oil used in the current DAF piston cooling jets (10-W30).

Temperature	Density	Dynamic Viscosity	Specific Heat		Thermal Conductivity	Thermal Diffusivity
			per unit mass	per unit volume		
°C	kg/m³	mPa.s = cP	kJ/kg.K	kJ/m³.K	W/m.K	mm²/s
0	877.1	692.7	1.81	1584.8	0.1355	0.085
5	873.7	478.0	1.83	1594.9	0.1351	0.085
10	870.4	338.6	1.84	1604.4	0.1348	0.084
15	867.0	245.6	1.86	1614.2	0.1344	0.083
20	863.7	182.0	1.88	1623.5	0.1340	0.083
25	860.3	137.6	1.90	1633.1	0.1337	0.082
30	857.0	105.9	1.92	1642.1	0.1333	0.081
35	853.6	82.88	1.93	1651.4	0.1329	0.080
40	850.3	65.85	1.95	1660.3	0.1326	0.080
45	846.9	53.06	1.97	1669.3	0.1322	0.079
50	843.6	43.30	1.99	1677.9	0.1318	0.079
55	840.2	35.76	2.01	1686.7	0.1315	0.078
60	836.9	29.85	2.03	1695.0	0.1311	0.077
65	833.5	25.17	2.04	1703.6	0.1307	0.077
70	830.2	21.43	2.06	1711.7	0.1304	0.076
75	826.8	18.39	2.08	1720.0	0.1300	0.076
80	823.5	15.91	2.10	1727.9	0.1296	0.075
85	820.1	13.87	2.12	1736.0	0.1293	0.074
90	816.8	12.17	2.13	1743.6	0.1289	0.074
95	813.4	10.74	2.15	1751.4	0.1285	0.073
100	**810.1**	**9.542**	**2.17**	**1758.8**	**0.1282**	**0.073**
105	806.7	8.522	2.19	1766.3	0.1278	0.072
110	803.4	7.649	2.21	1773.5	0.1274	0.072
115	800.0	6.898	2.23	1780.8	0.1271	0.071
120	796.7	6.248	2.24	1787.7	0.1267	0.071
125	793.3	5.683	2.26	1794.8	0.1263	0.070
130	790.0	5.189	2.28	1801.4	0.1260	0.070
135	786.6	4.755	2.30	1808.3	0.1256	0.069
140	783.3	4.373	2.32	1814.7	0.1252	0.069
145	779.9	4.034	2.34	1821.3	0.1249	0.069
150	776.6	3.732	2.35	1827.4	0.1245	0.068

Figure A.1: Oil properties (10-W30).

B

Sampled velocity results from LES study on the oil jet

The results of the trend analysis performed in Chapter 3 consist of the flow rate efficiency, the sampled oil volume fraction and the sampled oil velocity in axial direction. For the spray cooling analysis in Chapter 5, the volume fraction and the velocity are used to determine the effect of on the heat transfer. In Chapter 3 only the results for the sampled oil volume fraction are shown, since these give an indication of the spreading behaviour of the jet. The sampled velocity plots do not show the distinction between the oil phase and the air phase, and therefore are not very useful for the analysis of jet behaviour. However, they are needed in Chapter 5 to analyse the effect of the jet behaviour on the impingement heat transfer, therefore these results are presented next for the interested reader.

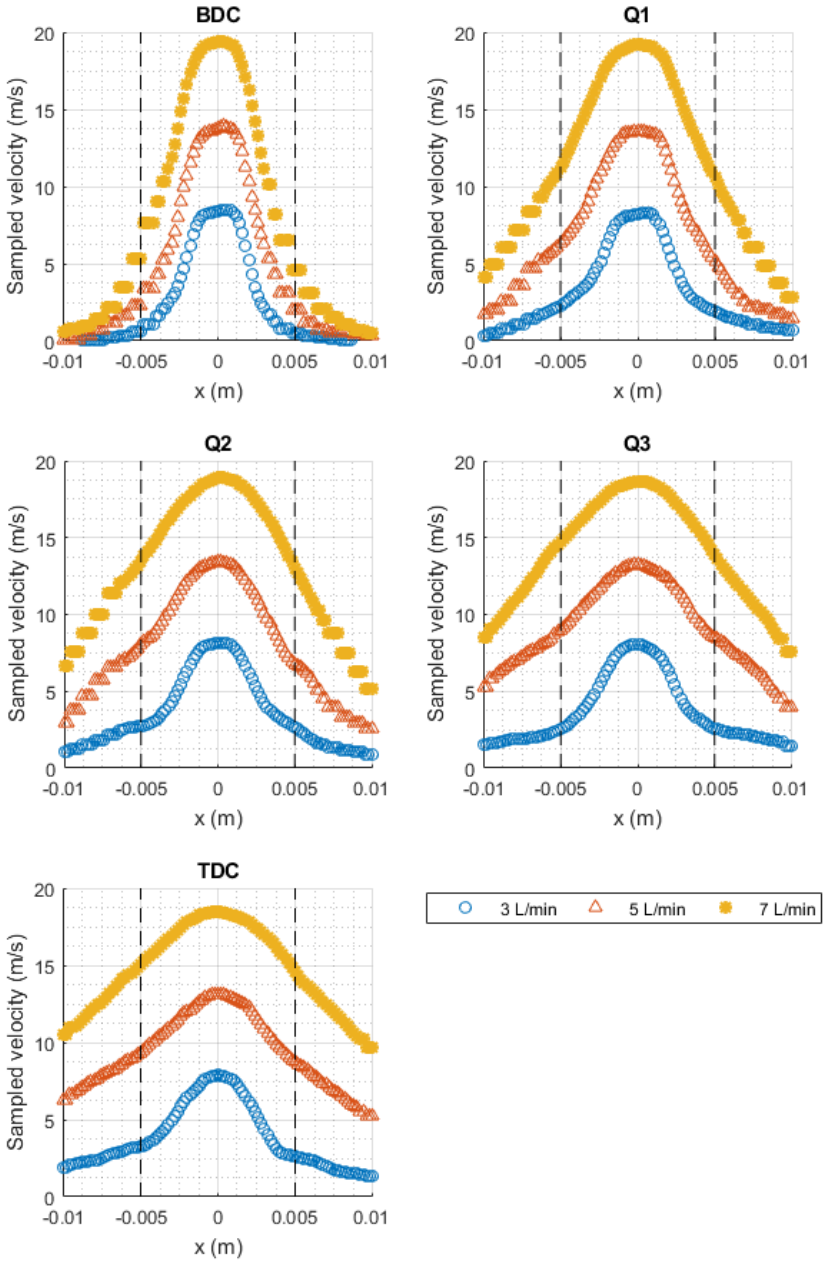

Figure B.1: Sampled oil velocity results for flow rates at different piston locations.

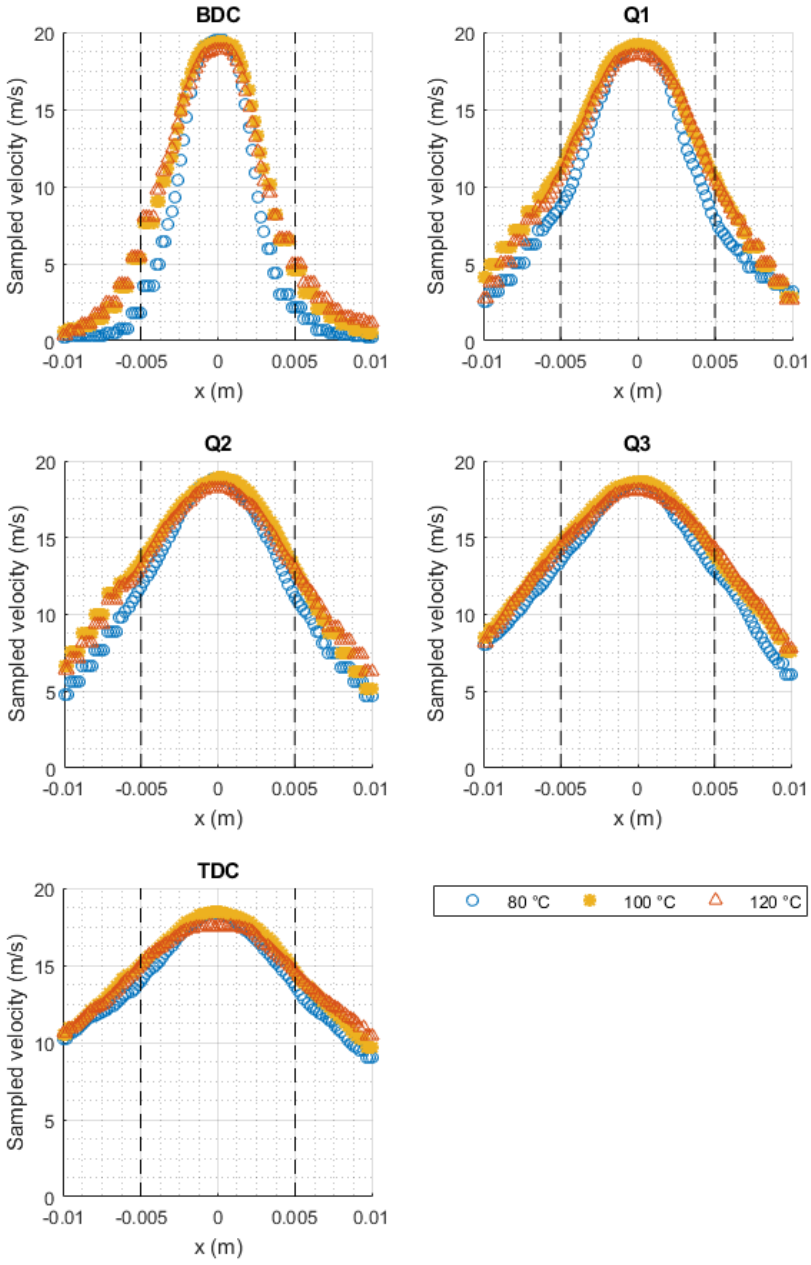

Figure B.2: Sampled oil velocity results for temperatures at different piston locations.

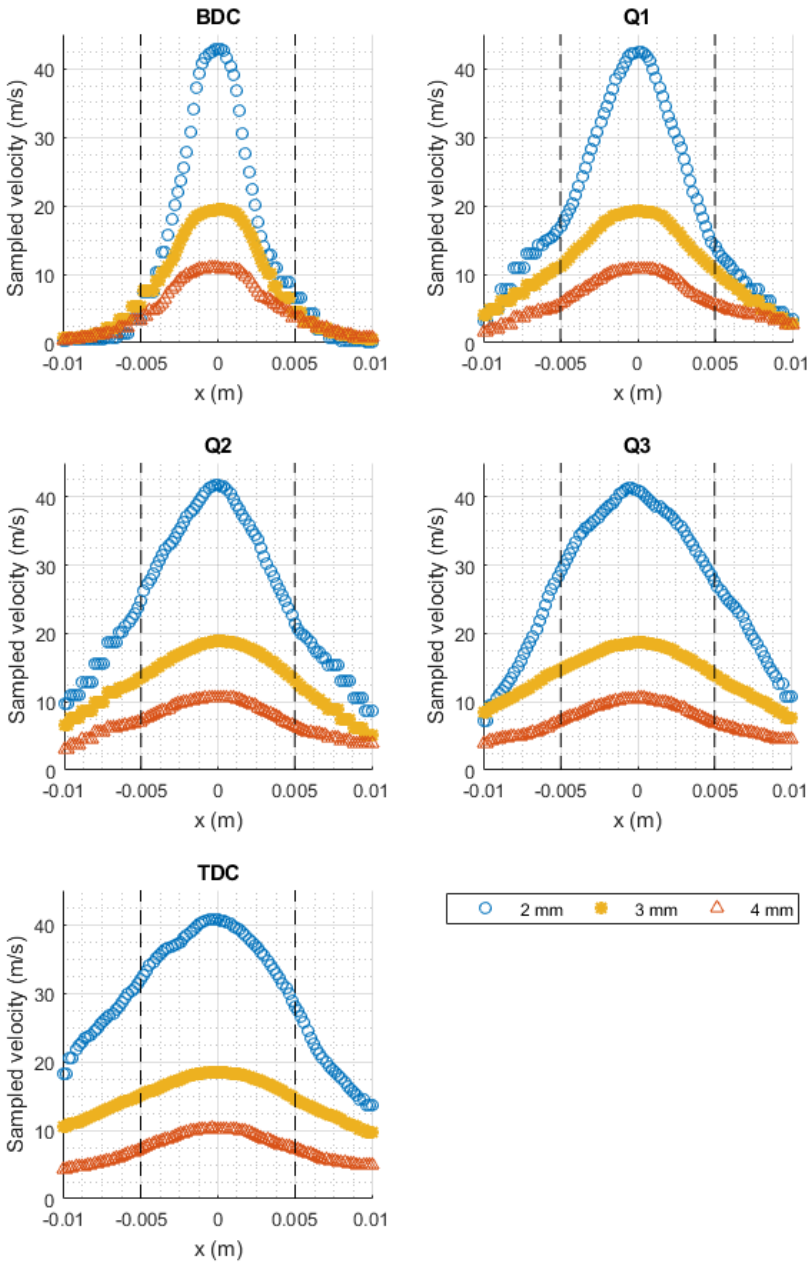

Figure B.3: Sampled oil velocity results for diameters at different piston locations.

C

Pipe flow precursor simulation

The precursor simulation is used to produce fully developed turbulent inlet conditions for the simulations used in Chapter 3 and Chapter 4. The definition of a fully developed profile is that flow properties do not change in the direction of the flow. This is accomplished by recycling the flow properties at the outlet, and feeding these back to the inlet. This is similar to the simulation of a pipe with infinite length. Therefore the output velocity profile can be obtained from any cross section of the nozzle, once there are no variations in flow direction anymore.

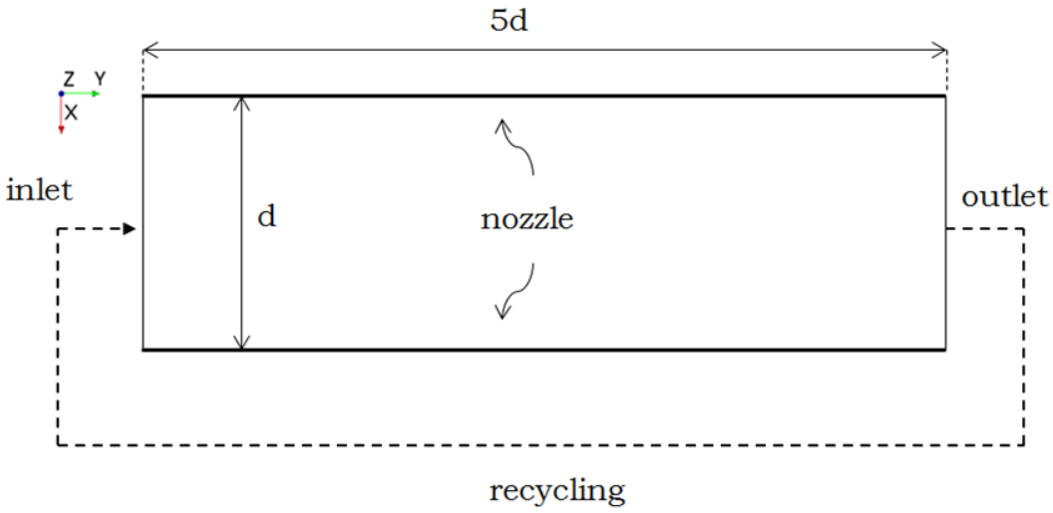

Figure C.1: Schematic of the computational domain and dimensions for the precursor pipe flow simulations.

D

1D heat balance analysis

The heat flux determination in Chapter 4 (and Chapter 5) is explained next. This calculation was performed in an early stage of the research project, to estimate the area-averaged Nusselt number and heat transfer coefficient needed to remove the heat flux by combustion. In this calculation, it is assumed that the heat flux is only removed by piston cooling, and thus there is no heat removal through the liner, resulting in a one-dimensional heat transfer problem. The problem schematic is presented in Fig. D.1

It is found in [19] that 2% of the heat created by combustion leaved through the pistons (with piston cooling). The total heat created by combustion is determined by using the fuel consumption at 1600 RPM. The percentage of mechanical power of the MX-13 engine is around 40%, resulting in a heat per piston of 3125 W. Using the surface area of the disc, the resulting heat flux is 250 kW/m^2.

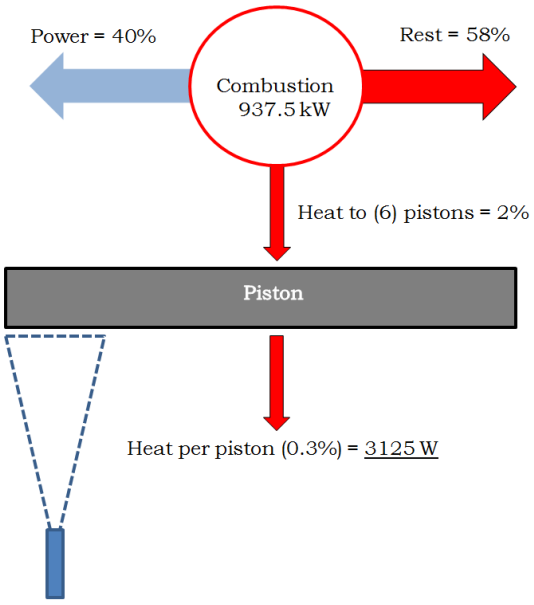

Figure D.1: Schematic of the one-dimensional heat transfer problem, to estimate the heat flux per piston, for the MX-13 engine running at 1600 RPM.